



ADVERTIMENT. L'accés als continguts d'aquesta tesi queda condicionat a l'acceptació de les condicions d'ús establertes per la següent llicència Creative Commons:  <https://creativecommons.org/licenses/?lang=ca>

ADVERTENCIA. El acceso a los contenidos de esta tesis queda condicionado a la aceptación de las condiciones de uso establecidas por la siguiente licencia Creative Commons:  <https://creativecommons.org/licenses/?lang=es>

WARNING. The access to the contents of this doctoral thesis it is limited to the acceptance of the use conditions set by the following Creative Commons license:  <https://creativecommons.org/licenses/?lang=en>



**Universitat Autònoma
de Barcelona**

DOCTORAL THESIS

Magnetoelectric Heterostructures with Reduced Substrate Clamping Effect

Filippos Giannis Perdikos

Directors:

Prof. Josep Nogués
Dr. Borja Sepúlveda

Tutor:

Prof. Josep Nogués

Universitat Autònoma de Barcelona
Departament de Física
Programa de Doctorat en Ciència de Materials

Bellaterra (Barcelona), June 2023

This work has received funding from the European Union's Horizon 2020 research and innovation programme under the Marie Skłodowska-Curie grant agreement No 861145.



The present work entitled 'Magnetolectric Heterostructures with Reduced Substrate Clamping Effect' presented by Filippos Giannis Perdikos to obtain the degree of Doctor in Materials Science by **Universitat Autònoma de Barcelona**, was performed at the **Magnetic Nanostructures Group** at the **Catalan Institute of Nanotechnology and Nanoscience (ICN2)**, under the supervision of Prof. Josep Nogués and Dr. Borja Sepúlveda.

The present thesis was also performed under the doctoral studies 'PhD in Materials Science' at the Physics Department, Sciences Faculty, Universitat Autònoma de Barcelona, under the tutorship of Prof. Josep Nogués.

A handwritten signature in black ink, appearing to be 'Filippos Giannis Perdikos', written in a cursive style.

Filippos Giannis Perdikos
(Author)

A handwritten signature in blue ink, appearing to be 'Josep Nogués', written in a cursive style.

Prof Josep Nogués
(Director/Tutor)

A handwritten signature in blue ink, appearing to be 'Borja Sepúlveda', written in a cursive style.

Dr Borja Sepúlveda
(Director)

Στο άπειρο πορεύομαι
απ' το άπειρο ξεκίνησα
κέντρο του σύμπαντος κι αθάνατος
νόμιζα ο άμυαλος πως ήμουνα...
- Θανάσης Παπακωνσταντίνου

To those who are, those who were, and those who will be

PREFACE

I. Acknowledgments

First and foremost, I would like to express my deepest appreciation to my supervisors, Josep Nogués and Borja Sepúlveda, for their guidance, virtually unlimited patience, and willingness to hire an engineer to do physics! Their vast knowledge and expertise have been crucial in shaping my research and helping me overcome the numerous challenges I encountered along the way. I am truly grateful for their unwavering support and encouragement throughout my thesis.

I would also like to extend my sincere gratitude to my colleagues in the magnetic nanostructures group. Firstly, from the group: MJ, Alex, Patxi, Pau, Guba, Nour, Aritz, Jessica and Arnau. I will always cherish the times we shared in the office laughing and stressing over small things! And in the words of the doctora, ningun hello, ningun afternoon! From the project, I want to thank for their unconditional friendship: Muireann for her rational advice and for always keeping a positive and contagious attitude towards everything, Quim for his brotherly qualities and for his patience whenever I needed use the PFM at ETH, Maksim for the amazing discussions on life and science, and Gaja, Berto, Zhibo, Song and Tan for their constant willingness to join me for a cold one. I am proud to call you all my friends.

I am thankful for the support provided by Roque, Marcos, Francisco and Raul who have provided me with the necessary resources to conduct my research. Additionally, I would like to express my appreciation to Jordi Sort, Aliona Nicolenco and Pau Solsona who have generously shared their expertise and resources, enabling me to complete my research successfully. I cannot thank them enough for their commitment and I am truly honoured to have had the opportunity to work with such talented individuals.

I am grateful to my parents Isabelle and Andreas, as well as my sister Olivia whose unconditional love and support pushed me all this way. Of course, I could not skip my friends for their constant love and encouragement throughout this journey. Their support and understanding have kept me motivated and focused, and I cannot thank them enough for being a source of great inspiration.

VERY special thanks go to my incredible girlfriend Avgi and my closest and most amazing friends Adrian, Chris and Christina as well as the latest transfers Maria and Manto who saw me both at my best and my worst and were willing to emotionally support me, each one in their own, unique way.

Finally, I would like to thank all the individuals who have supported me throughout my academic journey but whose names I may have inadvertently left out. I appreciate your support and contributions, and I am grateful for having had your influence.

Filippos Giannis Perdikos

II. Resumen

Debido a su capacidad para producir campos eléctricos mediante la aplicación de campos magnéticos externos, los materiales magnetoeléctricos (ME) han despertado un gran interés para muchas aplicaciones. En particular, tienen una contribución importante en la biomedicina al permitir el control inalámbrico de la entrega de medicamentos, la detección o la electroestimulación celular/neuronal inalámbrica a través de la aplicación de un campo magnético externo. El aumento del interés en los compuestos magnetoeléctricos ha puesto de relieve problemas como el efecto de sujeción del sustrato (“clamping effect”) que puede reducir la eficacia de los sistemas compuestos. En particular, la incorporación de sustratos flexibles o capas nanoestructuradas puede minimizar este efecto. Sobre esta base, el trabajo presentado en esta tesis doctoral se centra en el desarrollo de nuevos sistemas compuestos magnetoeléctricos que incorporarán dos métodos diferentes para abordar el problema de la sujeción del sustrato, para aplicaciones biomédicas.

En primer lugar, se desarrolló una película compuesta altamente flexible con una heteroestructura magnetoeléctrica Au/Ti/FeGa/ZnO integrada en una capa de elastómero de polidimetilsiloxano (PDMS). La fabricación combinó técnicas de deposición física en vacío y síntesis hidrotermal. La capa de ZnO piezoeléctrico crecida hidrotermalmente presentó un coeficiente piezoeléctrico de $d_{33} = 11.2 \pm 0.3$ pm V⁻¹. La película compuesta también mostró magnetización en-plano con coercitividad $H_c = 200$ Oe. La respuesta magnetoeléctrica con campo magnético alterno se evaluó mediante la degradación de azul de metileno, obteniendo los mayores campos eléctricos bajo un campo magnético de 200 Oe y frecuencia de 100 Hz. Se demostró la biocompatibilidad de la heteroestructura, y los estudios de proliferación celular mostraron un aumento del 42% en la proliferación después de 7 días de estimulación magnetoeléctrica de 1 hora diaria. La película compuesta altamente flexible podría ser adecuada para aplicaciones en biomedicina.

Además, se fabricaron microdiscos suspendidos de Au/FeGa/BaTiO₃ mediante deposición física en fase vapor, litografía coloidal y grabado por iones reactivos. Comparados con los microdiscos no suspendidos y las películas continuas de la misma composición, los microdiscos suspendidos mostraron una mejora significativa en el rendimiento magnetoeléctrico debido a la reducción del efecto de sujeción del sustrato. Los bordes de los microdiscos suspendidos mostraron una respuesta mecánica más fuerte que los centros sujetos y la película continua. Los coeficientes piezoeléctricos para la película continua, los microdiscos no suspendidos y los microdiscos suspendidos fueron 3.7 ± 0.3 pm·V⁻¹, 7.7 ± 0.4 pm·V⁻¹ y 13.2 ± 0.4 pm·V⁻¹, respectivamente. El coeficiente de acoplamiento magnetoeléctrico fue más alto para los microdiscos suspendidos, alcanzando 730 ± 70 V·cm⁻¹·Oe⁻¹ en el centro y 1040 ± 70 V·cm⁻¹·Oe⁻¹ en el borde, en comparación con

$260 \pm 70 \text{ V}\cdot\text{cm}^{-1}\cdot\text{Oe}^{-1}$ para la película continua. Los microdiscos suspendidos también demostraron una mayor eficacia en la degradación del azul de metileno bajo un campo magnético de 200 Oe y 100 Hz. La biocompatibilidad de las tres configuraciones fue confirmada por ensayos celulares durante 3 días. En conclusión, la película compuesta altamente flexible y los microdiscos suspendidos muestran un gran potencial en diversas aplicaciones, incluyendo biomedicina.

En resumen, el trabajo de esta tesis ha demostrado que el rendimiento de los sistemas magnetoeléctricos puede mejorarse mediante la implementación de enfoques para reducir el efecto de sujeción mediante: (i) un sustrato de elastómero o (ii) a través de la microestructuración y liberación de las capas formando estructuras independientes suspendidas. La respuesta magnetoeléctrica mejorada de ambos enfoques hace que este tipo de sistemas sea atractivo para aplicaciones en biomedicina.

III. Abstract

Due to their ability to produce electric fields by applying external magnetic fields, magnetoelectric (ME) materials have attracted considerable interest for many applications. In particular, they have an instrumental role in biomedicine by enabling wireless precision drug delivery, sensing or wireless cellular/neural electrostimulation via the application of an externally-applied magnetic field. The increased interest in magnetoelectric composites has brought forward issues which were not previously effectively dealt with; namely the substrate clamping effect which can reduce the effectiveness of composite systems. Particularly, the incorporation of flexible substrates or nanopatterned structures, can potentially minimize this effect. On this basis, the work presented in this PhD thesis is focused on the development of novel magnetoelectric composite systems which will incorporate two different methods to tackle the problem of substrate clamping, for biomedical applications.

Firstly, a highly flexible magnetoelectric composite film was developed by embedding a magnetoelectric Au/Ti/FeGa/ZnO heterostructure within a polydimethylsiloxane (PDMS) elastomer layer. The film was fabricated using a combination of physical vapor deposition and hydrothermal synthesis techniques. The hydrothermally-grown hexagonal ZnO nanosheet layer in the composite film exhibited a piezoelectric character, with a piezoelectric coefficient of $d_{33} = 11.2 \pm 0.3 \text{ pm} \cdot \text{V}^{-1}$. The composite film also showed in-plane magnetization with a moderate coercivity of $H_c = 200 \text{ Oe}$. To evaluate the magnetoelectric response, the film's electric field-induced methylene blue degradation under a magnetic field was studied. The most significant degradation was observed under a 200 Oe magnetic field at a frequency of 100 Hz, indicating the generation of the largest electric fields. Biocompatibility testing demonstrated that the heterostructure was compatible with living cells. Cell proliferation studies revealed a 42% enhancement in cell growth after 7 days of 1-hour daily magnetoelectric stimulation, suggesting the potential for biomedical applications.

Secondly, magnetoelectric Au/FeGa/BaTiO₃ suspended microdisc heterostructures were fabricated using physical vapor deposition, colloidal lithography, and reactive-ion etching. The properties of these structures were compared to non-suspended microdiscs and continuous films with the same composition. The suspended microdiscs exhibited a ferroelectric character and in-plane magnetization, with similar coercivity to the other morphologies. However, the saturation field differed among the three structures. The suspended microdiscs demonstrated significantly improved magnetoelectric performance due to reduced substrate clamping. Mechanical response measurements showed that the edges of the microdiscs exhibited stronger responses compared to the clamped centers and

the continuous film. The piezoelectric coefficients of the continuous film, non-suspended microdiscs, and suspended microdiscs were calculated as $3.7 \pm 0.3 \text{ pm} \cdot \text{V}^{-1}$, $7.7 \pm 0.4 \text{ pm} \cdot \text{V}^{-1}$, and $13.2 \pm 0.4 \text{ pm} \cdot \text{V}^{-1}$, respectively. The magnetoelectric coupling coefficient was highest for the suspended microdiscs, measuring $730 \pm 70 \text{ V} \cdot \text{cm}^{-1} \cdot \text{Oe}^{-1}$ at the center and $1040 \pm 70 \text{ V} \cdot \text{cm}^{-1} \cdot \text{Oe}^{-1}$ at the edge of the microdiscs, compared to $260 \pm 70 \text{ V} \cdot \text{cm}^{-1} \cdot \text{Oe}^{-1}$ for the continuous film. The superior performance of the suspended microdiscs was further demonstrated in catalytic experiments, where the magnetoelectric-induced electric field exhibited a significant effect on methylene blue degradation under a magnetic field of 200 Oe at 100 Hz. Biocompatibility testing confirmed that all three configurations were compatible with living cells. Preliminary results also indicated the ability to stimulate bone cells cultured on the suspended magnetoelectric microdiscs using a 200 Oe alternating magnetic field, as observed through confocal fluorescence microscopy. Overall, the highly flexible magnetoelectric composite film and suspended microdisc heterostructures hold great potential for diverse applications, particularly in biomedicine.

In summary, the work of this thesis has shown that the performance of magnetoelectric systems can be enhanced by the implementation of two different approaches to reduce the substrate clamping effect: (i) an elastomer substrate or (ii) by nanopatterning the composite into free-standing structures. The improved magnetoelectric response of both approaches makes this type of systems appealing for applications in biomedicine.

IV. Table of Contents

I.	Acknowledgments	11
II.	Resumen	13
III.	Abstract	15
IV.	Table of Contents.....	17
V.	Motivation	21
VI.	Aim & Objectives	23
VII.	Thesis outline	24
VIII.	References	25
1.	Introduction to Magnetoelectric Materials	27
1.1.	Magnetoelectric Materials.....	29
1.1.1.	Magnetoelectric Effect.....	29
1.1.2.	Single-Phase Magnetoelectric Materials.....	30
1.1.3.	Composite Magnetoelectric Materials (Heterostructures)	32
1.1.4.	Piezoelectric Effect.....	35
1.1.5.	Magnetism and Magnetostriction	39
1.1.6.	Applications of Magnetoelectric Materials	43
1.2.	References.....	49
2.	Introduction to Human Electrophysiology.....	55
2.1.	Physiology of Excitable Tissues.....	57
2.2.	Mechanisms of Excitable Cells.....	59
2.2.1.	Cell Membrane.....	60
2.2.2.	Ion Channels and Resting Membrane Potential.....	60
2.2.3.	Action Potentials.....	62
2.2.4.	Synaptic Transmission	64
2.2.5.	Diseases Associated with Defects of Tissue Excitability.....	64
2.3.	Electrostimulation of Excitable Cells for Clinical Treatments.....	65
2.3.1.	Mechanism of Artificial Excitable Cell Stimulation.....	66
2.4.	Established Clinical Treatments Using Wired Electrostimulation	67
2.4.1.	Limitations of Clinical Treatments Using Wired Electrostimulation..	69
2.5.	Wireless Tissue Electrostimulation	69
2.5.1.	Wireless Optical Stimulation	69
2.5.2.	Wireless Magnetic Stimulation.....	72
2.5.3.	Wireless Ultrasound Stimulation	73
2.5.4.	Limitations of Current Wireless Electrostimulation Techniques	73
2.6.	References.....	74

3.	Experimental Techniques	79
3.1.	Fabrication.....	81
3.1.1.	Substrate preparation.....	81
3.1.2.	Thin Film Deposition	81
3.1.3.	Polymer Substrate Fabrication	82
3.1.4.	Micropatterning.....	83
3.2.	Characterisation	84
3.2.1.	Morphological and Structural	84
3.2.2.	Magnetometry.....	85
3.2.3.	Scanning Probe Microscopy (SPM).....	85
3.2.4.	Magneto-Mechanical Flexibility Assessment.....	87
3.2.5.	Magnetic Stimulation System.....	88
3.2.6.	Indirect Evaluation of the Global ME-induced Electric Fields by Catalytic Degradation of Methylene blue	91
3.2.7.	Biological Characterisation	92
3.4.	References	94
4.	Highly Flexible FeGa/ZnO Magnetoelectric Thin Films.....	95
4.1.	Introduction	97
4.2.	Results and discussion.....	98
4.2.2.	Morphological Characterization	99
4.2.3.	Magnetic Characterization.....	102
4.2.4.	Piezoelectric Characterization	102
4.2.5.	Assessment of Mechanical Flexibility of Au/Ti/ZnO/FeGa/PDMS Film 103	
4.2.6.	Indirect Evaluation of the ME-induced Electric Fields by the Catalytic Degradation of Methylene Blue	104
4.2.7.	Biocompatibility and Proliferation Assays	106
4.3.	Conclusions.....	108
4.4.	References	109
5.	Suspended Au/FeGa/BaTiO₃ Magnetoelectric Microdiscs.....	111
5.1.	Introduction	113
5.2.	Results and Discussion.....	114
5.2.2.	Morphological and Structural Characterization.....	115
5.2.3.	Piezoelectric and Ferroelectric Characterization	117
5.2.4.	Magnetic and Magnetoelectric Characterization.....	119
5.2.5.	Indirect Evaluation of the ME-induced Electric Fields by Catalytic Degradation of Methylene Blue	122
5.2.6.	Biocompatibility Assay and Calcium Peak Detection.....	124
5.3.	Conclusions.....	127
5.4.	References	128

6.	Conclusions and Future Perspectives	131
6.1.	Conclusions	133
6.2.	Future Perspectives	134

V. Motivation

Magnetolectric (ME) materials have been the subject of significant attention due to their great potential in a variety of applications, including in biomedicine. These materials are able couple magnetism and electricity by combining piezoelectric (or ferroelectric) and magnetostrictive materials at the nanoscale level, creating artificial composites which exhibit both piezoelectric (or ferroelectric) and magnetostrictive behaviours. Consequently, they are able to convert magnetic energy into electrical energy and vice versa¹⁻⁵. However, the performance and applicability of these composites designed for the aforementioned applications is often hindered by the substrate clamping effect.

The substrate clamping effect refers to the influence of a rigid substrate on the performance of the ME composite, which limits its overall output efficiency by limiting the transfer of mechanical forces between the ferromagnetic and ferroelectric components, which in turn decreases the output electric field. Considering the principles of elasticity, when an external force is applied on a material, it elastically deforms until the force is removed. The degree of freedom of movement of the material depends on its elasticity. When a material is clamped onto a stiff substrate, the substrate restricts the deformation of the material, reducing its elasticity. In the case of ME composites, the issue arises from the mechanical coupling between the composite and the substrate, when the two are essentially bonded^{6,7}. The substrate can potentially act as a mechanical load on the composite, forming mechanical stress and strain, limiting its freedom of movement, and therefore reducing its piezoelectric response and inherently its ME response⁸. Moreover, rigid substrates can also inhibit their integration with biological tissues, leading to limited functionality and potential tissue damage. In contrast, soft implantable or injectable structures offer improved biocompatibility and conformability, allowing for better interaction with biological systems. Their flexibility and adaptability make them a more favourable choice for achieving safe and effective biomedical applications.

A method used to alleviate this effect is by using flexible thin film ME structures. These composites can be fabricated by growing a magnetostrictive layer directly on a flexible ferroelectric film, thus eliminating the need for a rigid substrate, reducing its mechanical constraint, allowing it to be flexible and conformable, and improving its ME performance. Thin films can also be fabricated by embedding the ME system in a flexible polymer which essentially acts as a substrate, reducing the substrate clamping effect⁹⁻¹¹. Additionally, patterned nanostructured materials have shown improved mechanical properties. Nanoparticles, nanowires, or patterned thin films have the ability to limit the mechanical constraint of the substrate by containing it into a smaller area, allowing the ME device being more flexible and increasing its ME efficiency¹²⁻¹⁴.

In summary, the substrate clamping effect is a significant challenge for achieving highly efficient ME composites. Different approaches have been proposed to reduce this effect, including the use of flexible thin film substrates, optimized geometries, and non-planar structures. By reducing the substrate clamping effect, the performance of ME composites can be improved, enabling their use in a wider range of applications. Therefore, the main goal of this thesis is the development of ME composite heterostructures, leading to an enhanced ME response, and improved integration in tissues for potential applications in biomedicine.

VI. Aim & Objectives

Magnetolectric (ME) materials are a very unique and promising class of materials that offer significant potential in various applications. Due to the fact that they are a relatively young and still developing field of research, there are still a lot of challenges that need to be addressed in order to unlock their full potential. The aim of this thesis is to develop novel, soft implantable or injectable ME heterostructures for biomedical applications. These ME structures are based on the coupling between piezoelectric/ferroelectric and magnetostrictive materials, which exhibit a reduced substrate clamping effect by either integrating them in flexible substrates or by freeing them from the substrate by nanopatterning. More specifically, two ME systems have been developed in this thesis for wirelessly generating ME-induced electric fields:

1. A highly flexible magnetolectric (piezoelectric/magnetostrictive) nanostructured film composed of ZnO and FeGa, as wireless actuated implants for cell electrostimulation.
2. Nanostructured suspended BaTiO₃/FeGa magnetolectric (ferroelectric/magnetostrictive) microdiscs with enhanced magnetolectric coupling coefficient as potentially injectable structures.

VII. Thesis outline

This thesis is divided into six chapters which are summarized below:

- The first chapter presents an overview of the magnetoelectric effect, magnetoelectric materials, and their division into single-phase and composites. It also includes basic concepts of piezoelectricity, magnetism and magnetostriction, and a detailed literature review of current research in applications of magnetoelectric materials, crucial for the understanding of the work in this thesis.
- The second chapter discusses the basic concepts of human electrophysiology and how excitable cells regulate the electrical activity and bodily functions of the human body. One of the most promising applications of ME structures is in cell stimulation. Since the structures developed in this thesis will be used for ME cell stimulation, here in this chapter, basic concepts of human electrophysiology are described such as the mechanisms of excitable cells, diseases affecting the central nervous system, and how they can be treated using electrostimulation. The third chapter describes in detail the experimental techniques used in this work. The purpose is to provide details on the fabrication and characterisation used for the development of the ME systems in the thesis.
- The fourth chapter presents the highly flexible, conformable, PDMS-embedded Au/Ti/FeGa/ZnO thin film. The heterostructure exploits the flexible properties of PDMS to reduce the substrate clamping effect. It combines magnetostrictive FeGa with piezoelectric ZnO to achieve a magnetoelectric heterostructure. The magnetoelectric character of the film is indirectly evaluated by observing the catalytic effect of the magnetoelectrically-induced electric field on pollutant degradation. The magnetically induced mechanical flexibility is also assessed and quantified. Finally, the heterostructures are used to enhance the proliferation of human osteoblast cells by the electric field induced by the remote application of a magnetic field.
- The fifth chapter describes the suspended Au/FeGa/BaTiO₃ magnetoelectric microdiscs on Si substrates. The substrate clamping effect in this case is reduced by directly removing the Si substrate from the underside of the microdiscs. The piezoelectric, ferroelectric and magnetoelectric properties of the discs are studied by piezo force microscopy and compared with continuous film and non-suspended microdisc configurations of the same materials. As in the fourth chapter, the magnetoelectric response is indirectly assessed by observing the catalytic effect of the ME-induced electric field on pollutant degradation. Finally, the biocompatibility of the heterostructures

was evaluated using human osteoblast cell assays, and the stimulation of Saos-2 human osteosarcoma cells via voltage-gated calcium channels caused by the magnetoelectric effect was detected by confocal microscopy.

- The sixth chapter provides a summary of the conclusions drawn from this thesis, as well as the future perspectives.

VIII. References

1. Martin, L. W. *et al.* Multiferroics and magnetoelectrics: thin films and nanostructures. *J Phys: Condens Matter* **20**, 434220 (2008).
2. Annapureddy, V. *et al.* Magnetic energy harvesting with magnetoelectrics: an emerging technology for self-powered autonomous systems. *Sustain Energy Fuels* **1**, 2039–2052 (2017).
3. Srinivasan, G. Magnetoelectric Composites. *Annu Rev Mater Res* **40**, 153–178 (2010).
4. Eerenstein, W., Mathur, N. D. & Scott, J. F. Multiferroic and magnetoelectric materials. *Nature* **442**, 759–765 (2006).
5. Spaldin, N. A. & Ramesh, R. Advances in magnetoelectric multiferroics. *Nat Mater* **18**, 203–212 (2019).
6. Li, T., Wang, H., Ma, D., Li, K. & Hu, Z. Influence of clamping effect in BaTiO₃ film on the magnetoelectric behavior of layered multiferroic heterostructures. *Mater Res Bull* **115**, 116–120 (2019).
7. Almusallam, A. *et al.* Clamping effect on the piezoelectric responses of screen-printed low temperature PZT/Polymer films on flexible substrates. *Smart Mater Struct* **24**, 115030 (2015).
8. Kim, D. *et al.* Magnetoelectric coupling in micropatterned BaTiO₃/CoFe₂O₄ epitaxial thin film structures: Augmentation and site-dependency. *Appl Phys Lett* **119**, 012901 (2021).
9. Martin, L. W. & Rappe, A. M. Thin-film ferroelectric materials and their applications. *Nat Rev Mater* **2**, 16087 (2017).
10. Sharma, T., Aroom, K., Naik, S., Gill, B. & Zhang, J. X. J. Flexible Thin-Film PVDF-TrFE Based Pressure Sensor for Smart Catheter Applications. *Ann Biomed Eng* **41**, 744–751 (2013).
11. Benelmekki, M. & Erbe, A. Nanostructured thin films—background, preparation and relation to the technological revolution of the 21st century. *Front Nanosci* **14**, 1–34 (2019).
12. Wang, S., Shan, Z. & Huang, H. The Mechanical Properties of Nanowires. *Adv Sci* **4**, 1600332 (2017).
13. Chen, X.-Z. *et al.* Hybrid Magnetoelectric Nanowires for Nanorobotic Applications: Fabrication, Magnetoelectric Coupling, and Magnetically Assisted In Vitro Targeted Drug Delivery. *Adv Mater* **29**, 1605458 (2017).

14. Gao, W. *et al.* Flexible organic ferroelectric films with a large piezoelectric response. *NPG Asia Mater* **7**, e189–e189 (2015).

1. Introduction to Magnetoelectric Materials

1.1. MAGNETOELECTRIC MATERIALS

Magnetoelectric (ME) materials are a subcategory of multiferroic materials that denote the coupling of the magnetic and electrical properties of a material. As a result, there is induction of electric polarization \mathbf{P} (vector which expresses the electric dipole moments of a dielectric material) with the application of a magnetic field \mathbf{H} , or magnetization \mathbf{M} with the application of an electric field \mathbf{E} ^{1,2}.

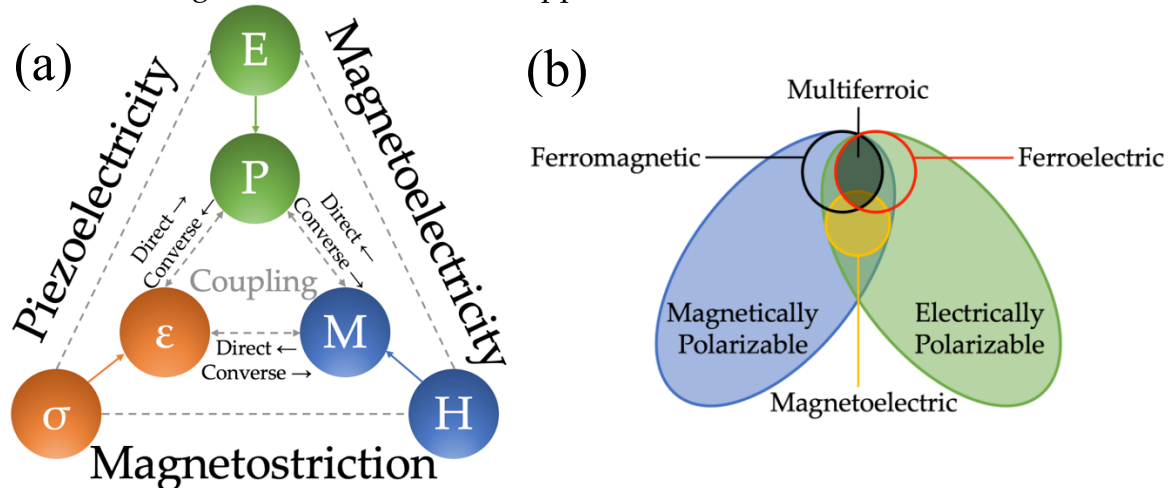


Figure 1.1. (a) Multiferroics interactions under external stimuli. E - electric field; σ – stress; H - magnetic field; P - electric polarization; ϵ – strain; M - magnetization³⁻⁵ (b) Relationship between multiferroic and magnetoelectric materials^{6,7}

As illustrated in **Figure 1.1a**, the magnetoelectric properties of multiferroic materials are just one aspect of multiferroics and, in fact, different properties (magnetization - \mathbf{M} , polarization - \mathbf{P} and strain - ϵ) can be tuned by manipulating the appropriate applied external stimuli (magnetic field - \mathbf{H} , electric field - \mathbf{E} and stress - σ). Additionally, the relationship between multiferroic and magnetoelectric materials is shown in **Figure 1.1b**.

1.1.1. Magnetoelectric Effect

The first documented work on the ME effect was carried out by Wilhelm Röntgen, who in 1888 discovered that a moving dielectric became magnetized with the application of an electric field^{8,9}. In 1894, Pierre Curie developed the theory of existence of such effects in non-moving objects in an inherent, natural manner¹⁰. The term “magnetoelectric” was first documented by Peter Debye, who was unsuccessfully trying to prove the concept¹¹. Harold Wilson was able to prove the polarization of a moving dielectric under magnetic field a few years later, in 1905¹². It was only in 1960, when Dzyaloshinskii and Astrov were able to experimentally confirm polarization under a magnetic field, as well as production of magnetization under an electric field in the antiferromagnetic Cr_2O_3 ¹³⁻¹⁷.

In order to express ME coupling, Landau's equation of free energy, F , can be used¹⁸:

$$F(E, H) = F_0 - P_i^S E_i - M_i^S H_i - \frac{1}{2} \epsilon_0 \epsilon_{ij} E_i E_j - \frac{1}{2} \mu_0 \mu_{ij} H_i H_j - \alpha_{ij} E_i H_j - \beta_{ijk} E_i H_j H_k \dots \quad (1.1)$$

, where i and j denote cartesian coordinates, F_0 is the free energy of a disordered system, P_i^S and M_i^S are spontaneous polarization and magnetization, ϵ_0 and μ_0 are permittivity and permeability of free space, ϵ_{ij} and μ_{ij} are the relative electrical permittivity and magnetic permeability of the material. The vector α_{ij} determines the magnitude of the linear direct ME coupling coefficient in the material¹⁹.

When equation (1.1) is differentiated with respect to E_i or H_i , and ϵ_{ij} or μ_{ij} is each set to zero in order to eliminate the influence of electrical conductivity, the appropriate ME responses can be obtained. For given magnetic and electric fields, polarization \mathbf{P} and magnetization \mathbf{M} are related to the electric field \mathbf{E} and magnetic field \mathbf{H} and their models are expressed with the equations²⁰:

$$P_i(H) = \frac{\partial F(E)}{\partial E_i} = P_i^S + \epsilon_0 \epsilon_{ij} E_j + \alpha_{ij} H_j + \dots \quad (1.2)$$

$$M_i(E) = \frac{\partial F(E)}{\partial H_i} = M_i^S + \mu_0 \mu_{ij} H_j + \alpha_{ji} E_j + \dots \quad (1.3)$$

, quantifying the dependence of polarization on magnetic field and of magnetization on electric field. Therefore, the ME coupling coefficients can be expressed in the form:

$$\alpha_E = \alpha_{ij}^H = \frac{\partial P_i}{\partial H_j} \text{ in } V / (Oe \cdot cm) \text{ for the direct ME effect} \quad (1.4)$$

$$\alpha_B = \alpha_{ij}^E = \frac{\partial M_i}{\partial E_j} \text{ in } (Oe \cdot cm) / V \text{ for the converse ME effect} \quad (1.5)$$

Note that the generation of electric polarization by an applied magnetic field is usually denoted as direct ME effect, whereas inducing magnetization using electric fields is called converse ME effect. The ME coefficient denotes the efficiency of a given material in terms of polarization or magnetization production with applied magnetic or electric fields, for the direct or converse ME effect, respectively (**Figure 1.1a**).

1.1.2. Single-Phase Magnetoelectric Materials

Single-phase ME materials exhibit an intrinsic coupling between the magnetic and electrical properties in the same phase (**Figure 1.1a**). We can divide single-phase magnetoelectrics into two main categories. The first group, type-I magnetoelectrics, are materials in which the properties of ferromagnetism (Section 1.1.5) and ferroelectricity (Section 1.1.4.1) are separated from each other, although there is weak coupling between the two properties. In these materials, usually electric polarization is stronger and typically appears at higher temperatures than their magnetic properties. For the type-II magnetoelectric, ferroelectricity is actually

caused by magnetism. This automatically means the existence of a much stronger coupling than of those in type-I, but they tend to have smaller polarization ($\approx 10^{-2} \mu\text{C}/\text{cm}^2$). For comparison, in type-I BiFeO_3 , ferroelectricity occurs at around $T_C \approx 1100 \text{ K}$, while magnetic ordering occurs at $T_N = 643 \text{ K}$, the spontaneous polarization is around $P \approx 90 \mu\text{C}/\text{cm}^2$. In type-II TbMnO_3 , there is ferroelectricity at $T_C \approx 27 \text{ K}$ and magnetic ordering at $T_N \approx 41 \text{ K}$. In this case, spontaneous polarization is around $P \approx 0.07 \mu\text{C}/\text{cm}^2$, however, as explained earlier, the ME coupling in these materials is stronger^{21–26}.

Each type of single phase magnetoelectrics is divided into subgroups, which separates materials according to their mechanism of production of ferroelectricity.

1.1.2.1. Type-I Single-Phase Magnetoelectrics

Ferroelectricity due to lone pairs

In this case, one of the positively-charged ions has two 6s unbonded valence electrons which orbit around the core ion but are not part of the chemical bond (“lone pairs”). These electrons create an electrical dipole, which makes the material polarizable and gives it its ferroelectric behaviour. The magnetic ions are responsible for the magnetic order. For example, in the case of BiFeO_3 , Bi^{3+} makes the material ferroelectric, while Fe^{3+} give the material its magnetic character^{27–31}.

Geometric ferroelectricity

In these materials, structural instabilities and geometric constraints lead to ionic shifts, inducing polarization and thus ferroelectricity. For example, in BaNiF_4 ferroelectricity originates from the asymmetry between Ba^{2+} and F^{28,32–34}. Another example is that of hexagonal manganites (h-) RMnO_3 (R = rare earth) where a tilt and deformation of MnO_5 bipyramids displace the rare-earth (RE) ions, leading to spontaneous polarization.

Ferroelectricity due to charge ordering

In materials containing transition metal ions with valence electrons in different states, ferroelectricity can appear after charge ordering of the different states, when sites and bonds are inequivalent. An example of this subcategory is LuFe_2O_3 , where spontaneous polarization is observed after charge ordering, in which alternating layers of Fe^{2+} and Fe^{3+} of ratios of 2:1 and 1:2, is created^{28,33,35,36}.

1.1.2.2. Type-II Single-Phase Magnetoelectrics

Spin-driven ferroelectricity

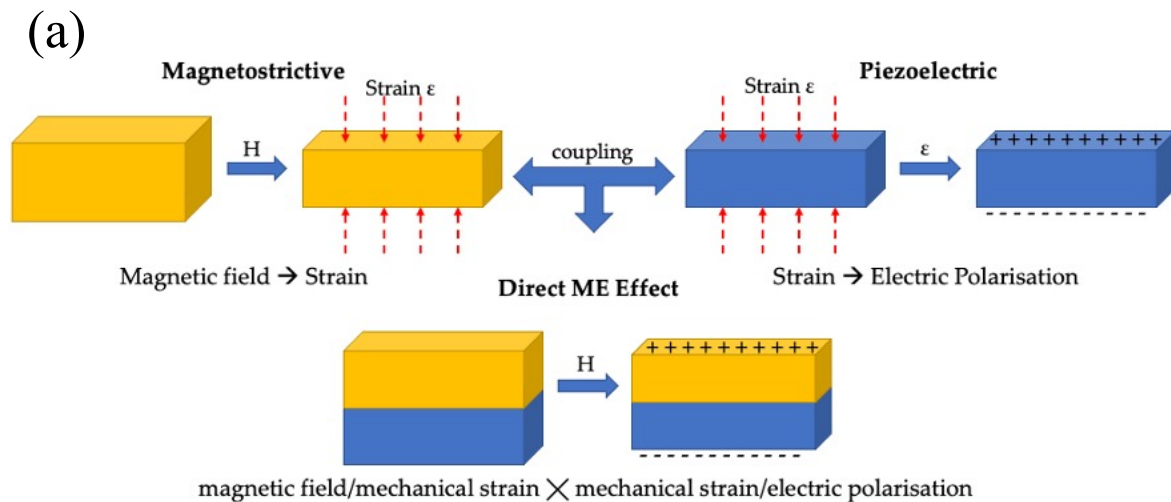
In the case of spin-driven ferroelectricity, these materials are the exception to the rule, where instead of having the FE and magnetic orders operating separately, the magnetic order activates ferroelectricity by breaking the inversion symmetry. This is achieved by transferring the central asymmetry from the magnetic to the electric lattice due to the influence between spins and charges which can create polarization^{37–39}.

1.1.3. Composite Magnetoelectric Materials (Heterostructures)

Even though ME properties can be found intrinsically in single-phase ME materials, their limited number and often low magnetic transition temperatures, led to the development of composite ME materials which artificially couple the electric and magnetic properties (**Figure 1.1b**). This coupling is commonly obtained by combining piezoelectric and magnetostrictive phases into a single heterostructure, whose efficiency can be adjusted to the requirements of their application. Thus, most composite ME heterostructures are composed of (i) a piezoelectric material (see Section 1.1.4), which induces a polarization (P) when subject to a stress (σ) or generates a strain (ϵ) when an electric field (E) is applied, and (ii) a magnetostrictive magnetic material (see Section 1.1.5), which generates a strain (ϵ) when subject to a magnetic field (H) or a change in magnetization (M) when a stress (σ) is applied. By combining the properties of these two materials and through the exchange of stress - strain between both materials, the electric polarization or magnetic moment can be manipulated, using magnetic or electric fields, depending on the type of required effect. The two types of ME coupling that exist are (a) Direct ME Coupling and (b) Converse ME Coupling (**Figure 1.2**)⁴⁰. Direct ME coupling denotes the generation of electrical polarization with the application of magnetic field, whereas the latter denotes the induction of magnetization with the application of an electric field.

$$(a) \text{ Direct ME Coupling} = \frac{\text{Magnetic}}{\text{Mechanical}} \times \frac{\text{Mechanical}}{\text{Electrical}} \quad (1.6)$$

$$(b) \text{ Converse ME Coupling} = \frac{\text{Electrical}}{\text{Mechanical}} \times \frac{\text{Mechanical}}{\text{Magnetic}} \quad (1.7)$$



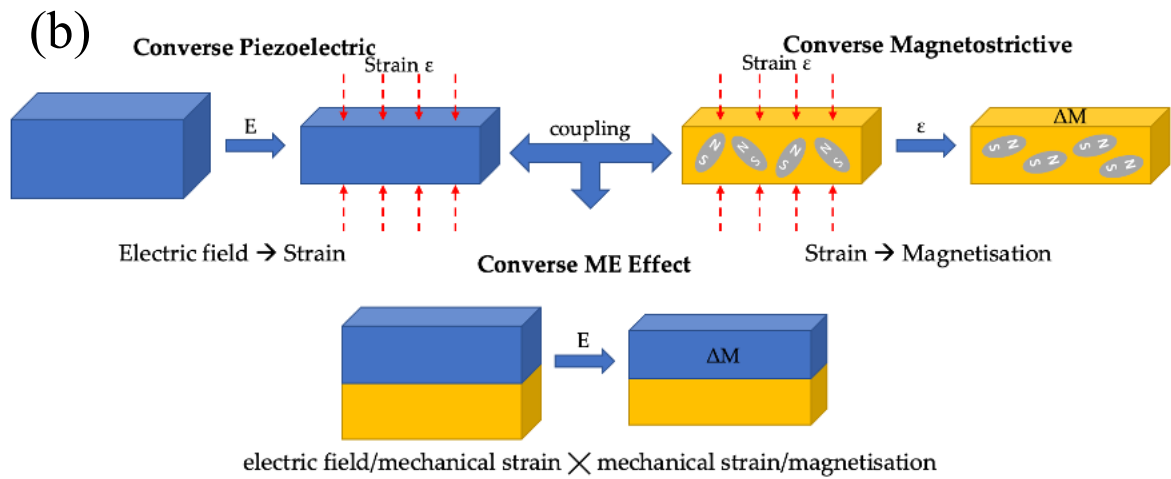


Figure 1.2. Schematics of (a) Direct ME effect and (b) Converse ME effect in ME composite heterostructures⁴¹

In **Figure 1.2**, the mechanisms of coupling and operation of the ME heterostructures are illustrated. In the case of the direct ME effect, the applied magnetic field causes mechanical strain in the magnetostrictive phase of the composite. The strain is then mechanically transferred to the piezoelectric phase causing electric polarization. Inversly, the converse ME effect is caused when an externally-applied electric field causes strain in the piezoelectric phase. The strain is then transferred to the magnetostrictive phase which causes magnetization change in the material (Viliari effect) by orientating its magnetic domains.

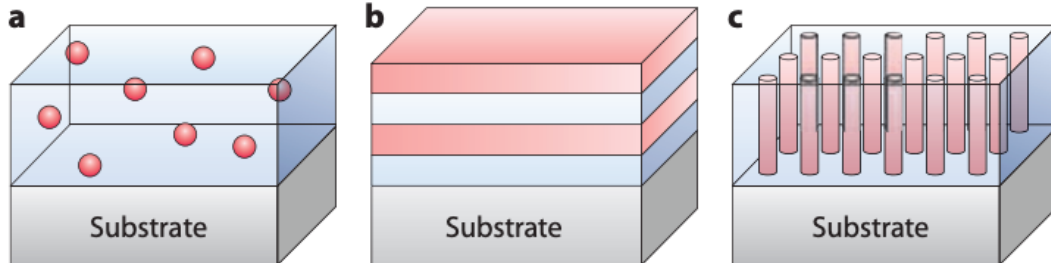


Figure 1.3. Illustration of three common ME composite heterostructures: (a) 0-3 particulate composite film with magnetic particles in a FE film; (b) 2-2 Laminate composites with alternating magnetic and piezoelectric layers; (c) 1-3 Rod composite⁴¹

Examples of different structure combinations of ME composites are illustrated in **Figure 1.3**. The notations used represent the number of coordinates in which there is interconnection between the components in the composite, with the first number representing the magnetostrictive phase and the second number representing the piezoelectric phase. For instance, 0-3 denotes single-phase magnetic particles (0) embedded in a piezoelectric matrix (3), and 2-2 is the planar composite of at least one magnetic (2) and one piezoelectric (2) layer.

1.1.3.1. Substrate Clamping Effect in ME Materials

The substrate clamping effect is a phenomenon which arises from the mechanical interaction between the piezoelectric or magnetostrictive materials and the rigid substrate on which they have been grown onto. This causes a reduction of the degree of freedom of movement of the layers, since the mechanical coupling to the substrate impedes the proper transmission of strain between the magnetostrictive and the piezoelectric layers, thereby significantly reducing the ME coefficient and leading to poor system performance.

There are a number of strategies to reduce this effect. A common approach is to use a buffer layer between the substrate and the grown ME materials. This layer can absorb the mechanical strain caused by the aforementioned interaction by acting essentially as a stress buffer. This method has been shown to be effective in reducing the substrate clamping effect in ME systems⁴².

Additionally, nanostructured materials, e.g., core/shell nanoparticles or nanowires⁴³, or patterning thin films have been demonstrated to reduce clamping effects⁴⁴. For example, by patterning the heterostructures into smaller sizes (**Figure 1.3a,c**), the mechanical constraint due to the substrate is localised and minimised, consequently increasing the degrees of freedom of movement of the structure. Namely, allowing the structures to have more flexibility individually, the overall performance of the device can be enhanced (**Figure 1.4**).

Furthermore, since the clamping effect originates from the interaction between grown ME layers and their rigid substrate, the use of flexible substrates, such as polymers, can also reduce the effect⁴⁵. Another related approach is to grow the magnetostrictive layer directly onto flexible ferroelectric materials (e.g., polyvinylidene fluorides), without the need of a rigid substrate⁴⁶. The flexible substrates can bend and deform, allowing the ME layer to conform to the substrate's shape, resulting to the reduction of the clamping effect and the improvement of the ME coefficient.

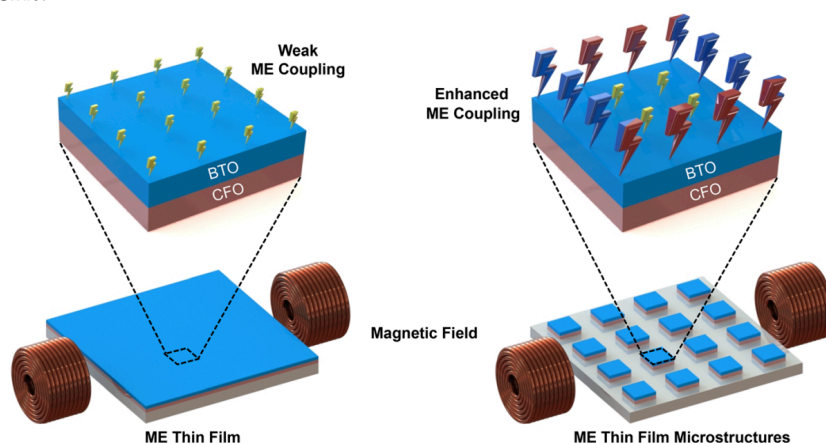


Figure 1.4: Comparison of ME coupling between plain ME bilayer (left) and micropatterned ME structure⁴⁴

1.1.4. Piezoelectric Effect

Piezoelectric materials are a subset group of dielectric materials and were first described by brothers Jacques and Pierre Curie⁴⁷ in 1880. The Curie brothers were able to prove that electric polarization occurred in hemihedral crystals under compression. In other words, piezoelectric materials have the ability to produce an *electric potential* when subjected to mechanical stress (*direct piezoelectric effect*). This phenomenon can be attributed to the atomic structure of these materials. This process is also reversible, meaning that they can generate internal strain with the application of an electric field (*converse piezoelectric effect*) (**Figure 1.5**).

The direct piezoelectric effect is expressed using the equation^{48,49}:

$$P_i = d_{ijk}\sigma_{jk} \quad (1.8)$$

, where P_i is the induced polarization (C/m^2), d_{ijk} is the piezoelectric charge coefficient (C/N) and σ_{jk} is the applied stress (N/m^2).

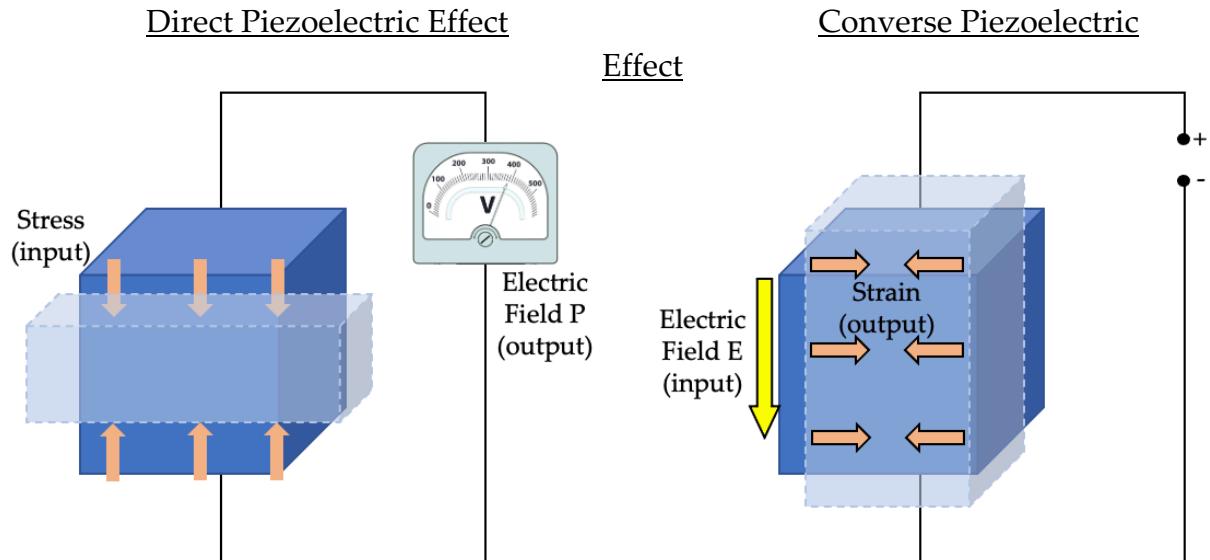


Figure 1.5. Schematic illustration of the direct and converse piezoelectric effects⁵⁰

The inverse, converse piezoelectric effect, occurs when an external electric field is applied to a piezoelectric material and internal strain is observed. The Curie brothers were also able to confirm its existence in 1881, and also prove reversibility of electro-elasto-mechanical deformations in piezoelectric crystalline structures⁴⁶. The converse piezoelectric is described as⁵¹:

$$\varepsilon_{jk} = d_{ijk}E_k \quad (1.9)$$

, where ε_{jk} is the induced strain and E_k is the applied electric field.

All piezoelectric materials are characterised by their non-centrosymmetric crystallographic structure. This means that the centre ion of the structure is not symmetric with respect to the other ions, as seen in **Figure 1.6a**. This displacement of the central ion creates an electrical polarity. By applying mechanical stress, the

position of the metal ion changes according to the direction of the applied stress, displacing the positive and negative ionic sublattices, alternating the asymmetrical shape of the structure and thus changing electrical polarity.

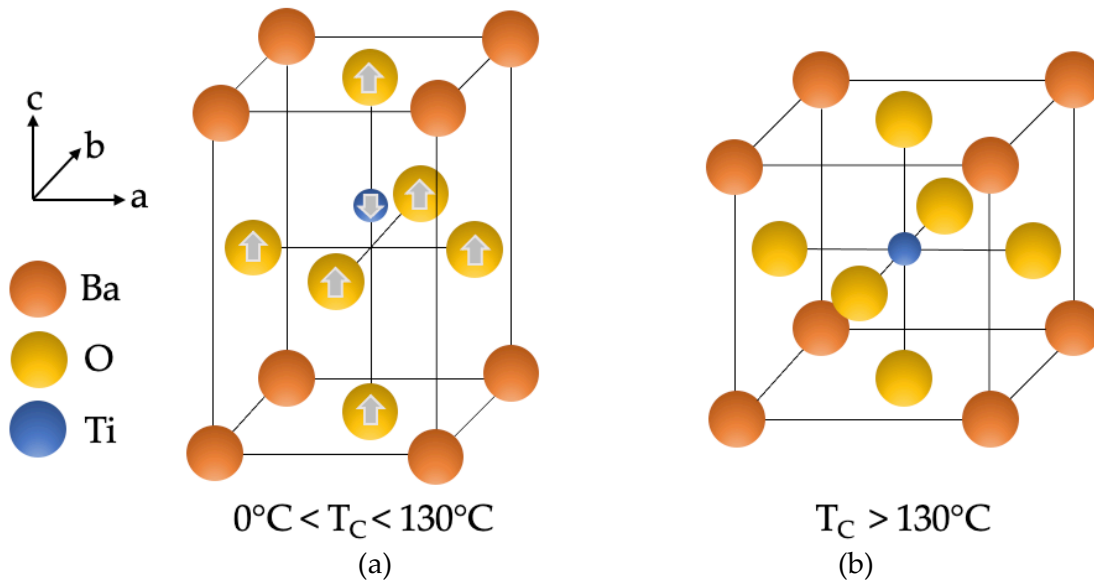


Figure 1.6. Schematic illustration of the perovskite structure of BaTiO_3 ⁵²

The *piezoelectric coefficient* is a parameter specific to each material, which relates the produced electric charge to the applied mechanical stress and its direction. It is expressed as⁵³:

$$d = \frac{\text{charge density (open circuit)}}{\text{applied stress}} = k\sqrt{\epsilon_0 k^T s^E} \quad (\text{C/N}) \quad (1.10)$$

where k is the electro-mechanical coupling coefficient, k^T is the dielectric constant of the material under constant stress, and s^E is the elastic compliance (10 m/N) under constant electrical field, which is described as the derivative of induced strain with respect to applied stress. The piezoelectric coefficient is measured in C/N units and is typically used to assess the efficiency of a piezoelectric material⁵⁴.

The piezoelectric coefficient is usually represented by a double subscript. The first subscript denotes the direction of polarization induced in the material, while the second subscript shows the direction of the applied stress or the induced stress. As observed in **Figure 1.7**, these directions are represented by the numbers 1, 2 and 3 for axes x , y and z , respectively and relative to the direction of the applied voltage or induced charge.

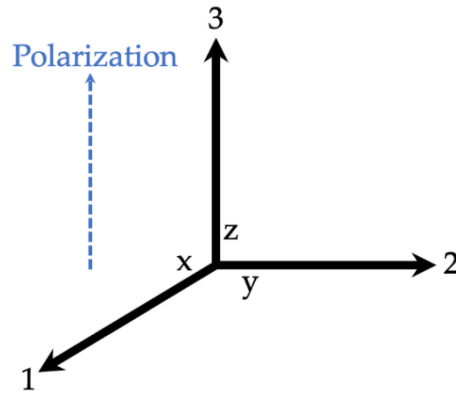


Figure 1.7: Directions of components which affect the piezoelectric coefficient⁵⁵

For example, d_{33} shows the piezoelectric coefficient when the material is polarized and when the applied stress (or induced strain) is in direction 3 (parallel to the material's polarization direction). In contrast, the coefficient d_{31} is the induced polarization in direction 3 when a stress (or induced strain) is applied in direction 1 (perpendicular to the material's polarization direction).

1.1.4.1. Ferroelectricity

A subcategory of piezoelectric and dielectric materials is *ferroelectric (FE) materials* (Figure 1.8). Ferroelectric materials, as they are piezoelectric, within a certain temperature range have non-centrosymmetric crystallographic structures and exhibit spontaneous and reversible electric polarization. In this case, polarization can also occur from an externally applied electric field and can remain even after the electric field has been removed (remanent polarization). For example, below 130°C, the *Curie Temperature* (T_c) of BaTiO₃, its phase is tetragonal, and the Ti ion shifts within the structure when an electric field is applied. This shift causes a structural asymmetry and depending on the location of the Ti ion in the cell relative to the centre the polarization changes and can be controlled accordingly⁵⁶.

As observed in Figure 1.6a, the BaTiO₃ FE oxide perovskite has a tetragonal structure. When the temperature exceeds the Curie Temperature, BaTiO₃ goes through a structural phase transition which results in a cubic structure, as seen in Figure 1.6b. Since it loses its asymmetry, above T_c the material is no longer ferroelectric and exhibits paraelectric properties⁵⁷, thus the relationship between induced polarization and external electric field becomes linear.

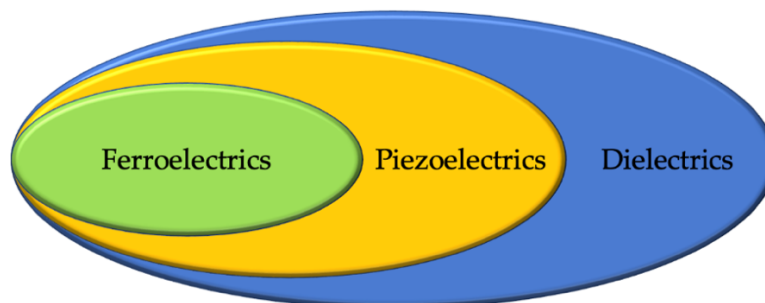


Figure 1.8. Relationship between FE, piezoelectric and dielectric materials⁵⁸

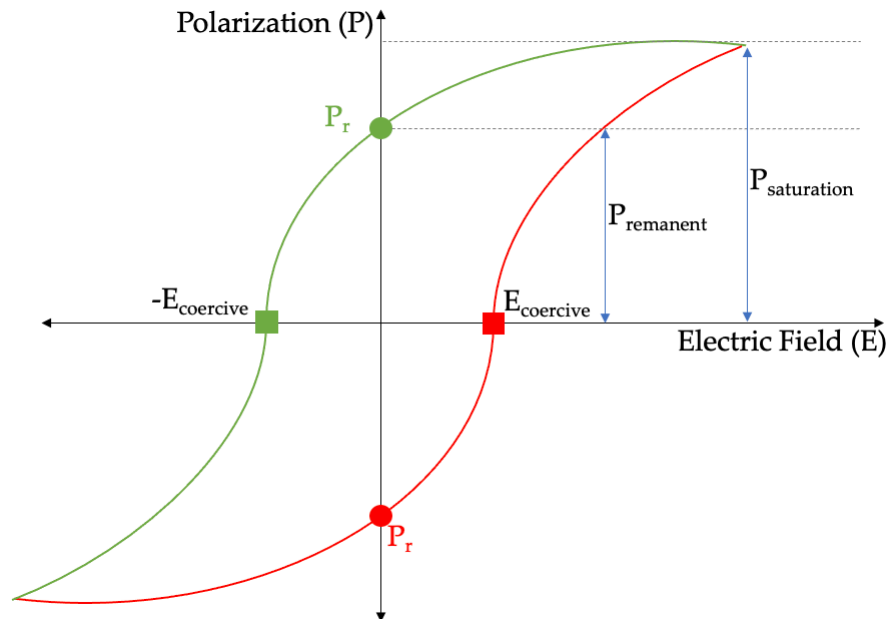


Figure 1.9. Typical hysteresis loop of a FE material

The typical hysteretic behaviour of a FE material is illustrated in **Figure 1.9**. It shows the relationship between polarization of the material with the externally-applied electric field. As a positive electric field is applied to the material, the polarization also aligns in the positive direction. The polarization increases until it reaches the saturation point ($P_{\text{saturation}}$) where it cannot be polarized anymore. If the electric field is removed, the polarization slightly decreases and reaches the remanent point (P_{remanent}). By applying negative electric field, the polarization reaches the zero point (E_{coercive}) and by increasing the intensity of the field, the polarization continues in the opposite direction, thus creating negative polarization³². The main attribute of FE materials is that when the electric field is removed, they retain their polarization (remnant polarization, hysteretic behaviour). This is also the difference between hysteresis loops of other dielectrics and ferroelectrics, in that non-ferroelectric dielectrics return to their neutral state when the electric field is removed as illustrated in **Figure 1.10**.

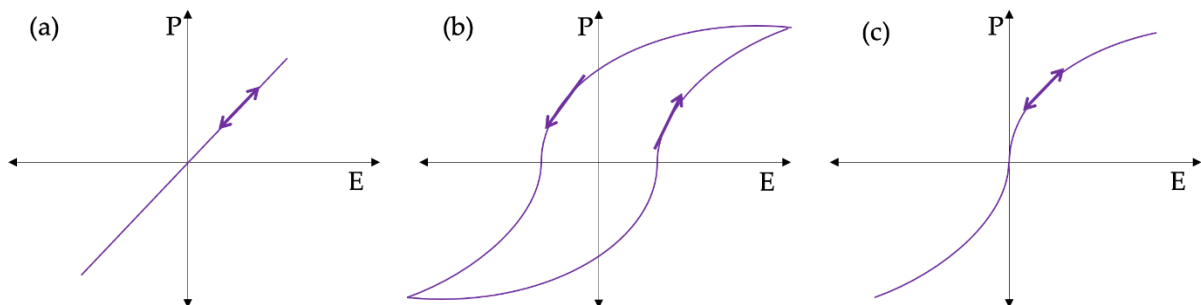


Figure 1.10: Electric polarization as a function of applied electric field in: (a) Dielectric; (b) Ferroelectric and (c) Paraelectric materials.

1.1.5. Magnetism and Magnetostriction

The magnetic nature of a material originates from the spin and orbital motion of electron pairs around the nucleus of their atoms. In most cases, the electrons are paired in opposite directions, thus the resulting magnetic moment is insignificant. However, in certain materials such as transition metals and rare earths, the electrons can be unpaired, leading to a net atomic moment. In solids, when the atomic moment of each atom order is random, thus the net magnetization, \mathbf{M} , (sum of all atomic moments) is negligible. However, in some cases the interaction between atoms (exchange interaction) can lead to the ordering of the atomic moments resulting in a net magnetization. Interestingly, depending on the distance between the atoms, the exchange interaction can be positive or negative, leading to parallel or antiparallel aligned atomic moments⁵⁹.

The response of a given material when subjected to an applied magnetic field, \mathbf{H} , is given by the susceptibility, χ .

$$\chi = M/H \quad (1.11)$$

Depending on material's response when placed under a magnetic field, magnetism can be divided into five categories^{61,61}:

Paramagnetism and *diamagnetism* is when a material is intrinsically either attracted to, or repelled by a magnetic field respectively, in a weakly manner. In the first case, magnetism originates from the existence of at least one unpaired electron whose moment aligns with the magnetic field, leading to a small net magnetization, with very small positive magnetic susceptibility. In the case of diamagnetism, there are no unpaired electrons, and the atoms have no magnetic moment. Instead, magnetism occurs from the realignment of the electron paths when a magnetic field is applied, which in turn creates a small negative magnetic susceptibility. In both these cases, when the field is removed, no magnetic response is retained.

Ferromagnetism is when a material has a large, positive magnetic susceptibility. As in paramagnetic materials, ferromagnetic materials have unpaired electrons, which align according to the applied magnetic field. In addition, ferromagnetic materials have a positive exchange interaction, which results in a collective response of the magnetic moment, creating a large magnetization and susceptibility.

Antiferromagnetism is similar to ferromagnetism in the sense that magnetic moments align in the presence of a magnetic field, but in this case, the alignment is antiparallel (negative exchange interaction), which makes them cancel each other's magnetic moments out. As a result, the net magnetization at zero field is zero. However, when a field is applied the atomic moments tends to align to the applied field leading to a net magnetization with a moderate susceptibility.

Ferrimagnetism is similar to antiferromagnetism with antiparallel magnetic moments. However, ferrimagnetic materials contain at least two different types of atoms with dissimilar magnetic moments. This inequality generates a response similar to ferromagnetic materials, but weaker.

The magnetic moment ordering of ferro-, antiferro- and ferrimagnetic materials is illustrated in **Figure 1.11**.

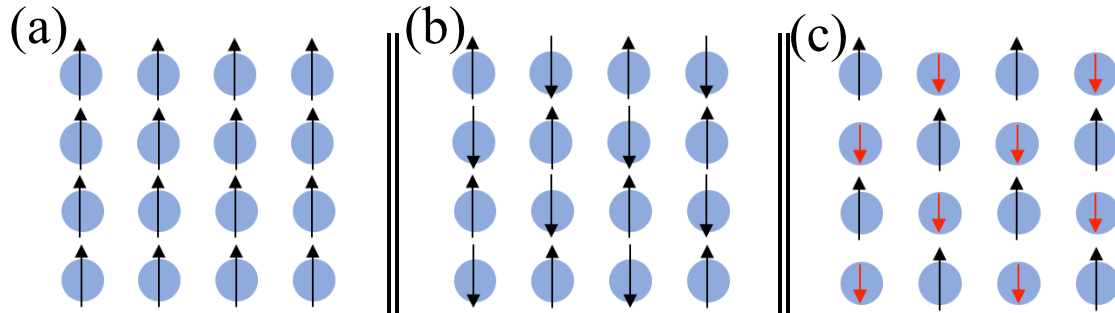


Figure 1.11: Magnetic moment ordering of: (a) Ferromagnetic materials; (b) Antiferromagnetic materials; (c) Ferrimagnetic materials

Interestingly, ferromagnetic and ferrimagnetic materials exhibit hysteretic behaviour (analogous to ferroelectric materials), as illustrated in **Figure 1.12**. Namely, after being magnetized at large fields (saturation magnetization, M_S), when the applied field is removed, they retain a certain amount of magnetization (remanent magnetization, M_R). To bring the magnetization back to zero, a negative applied field is required (coercivity, H_C).

In order to explain the hysteretic behaviour of polycrystalline ferro- and ferrimagnetic materials, the concept of *domains* is introduced. Domains refer to areas of a material where all the magnetic moments are aligned in the same direction. In polycrystalline materials under zero applied field (before any field is applied) the overall magnetization of the material is divided in a certain number of domains where the moments are aligned in different directions to minimize the energy. As the field is increased, two effects occur: (i) the moments in domains with a direction different to the direction of the applied field start to rotate towards the field, and (ii) domains with moments close to direction of the applied field merge creating larger domains. At saturation, all the domains have merged, and all the moments are aligned to the applied field. When the field is removed after saturation, the magnetization of the material breaks again into domains. At zero field (at remanence, M_R) there is domain configuration with domains in directions somewhat misaligned from the last applied field. At the coercivity H_C , the net sum of the moment of all the domains is zero (see **Figure 1.12**).

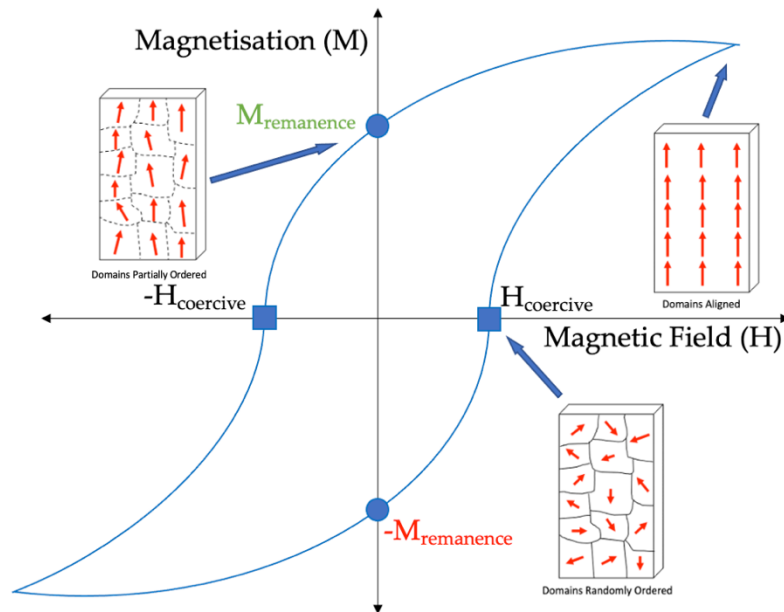


Figure 1.12. Magnetic hysteresis loop, where the main parameters, saturation magnetization, M_s , remanence, M_R , and coercivity, H_c , are indicated. The images schematically represent the evolution of the domain structure of the material at different stages of the magnetization process.

An interesting property of magnetic materials is magnetostriction. This refers to the capability of magnetic materials to deform when exposed to a magnetic field. It was first proven by James Joule⁶² who was able to observe a change in the length of iron bars when inserted in a current-carrying coil which generated a magnetic field (Figure 1.13a). This property originates from the motion of unpaired electrons in the atoms of magnetic materials, mainly due to the interaction between the spin and orbital motion of electrons, also called spin-orbit coupling. This coupling causes an asymmetry in the orbit of the electrons, which can induce small changes in the interatomic distances, resulting in changes in shape. This effect is weaker or stronger depending on the relative orientation between the magnetization and the applied field. Thus, in polycrystalline materials, the changes in shape depend on the evolution of the magnetic domains of the material, as they rotate and realign according to the direction of the magnetic field^{63,64}.

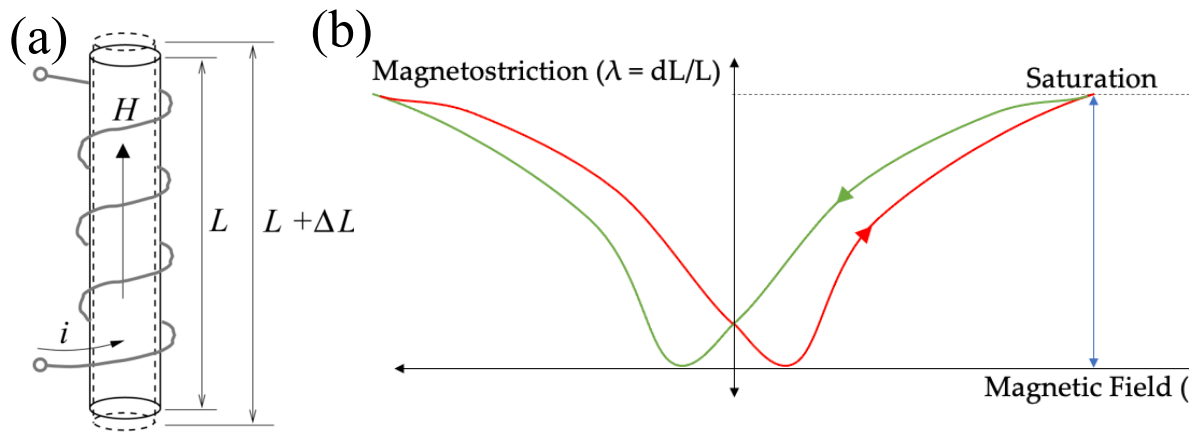


Figure 1.13. (a) Joule magnetostriction shape change caused by an H magnetic field^{65, 61}; (b) Typical magnetostriction curve of a FM material⁶⁶

As a positive magnetic field is applied, the domains start to align in the direction of the field, and the relative deformation of the material starts to increase. As the field intensity increases, more and more domains align until the saturation point is reached, where the material cannot deform anymore (**Figure 1.13b**). Contrary to the hysteresis loop of magnetization, when a negative magnetic field is applied, the deformation is in the positive direction⁶². The magnetostriction constant λ , is defined as the amount of deformation per unit length, i.e. $\lambda = dL/L$ ⁶⁸. The inverse of magnetostriction is called the *Villari effect* where a change in magnetization is observed when a material is subjected to mechanical stress. Emilio Villari was able to prove that by applying mechanical stress, it is possible to change the magnetic susceptibility of FM materials⁶⁹.

1.1.6. Applications of Magnetolectric Materials

1.1.6.1. Microelectronics

ME materials have attracted significant attention in the field of microelectronics for a variety of applications including magnetic field sensors, energy harvesters and devices which store information.

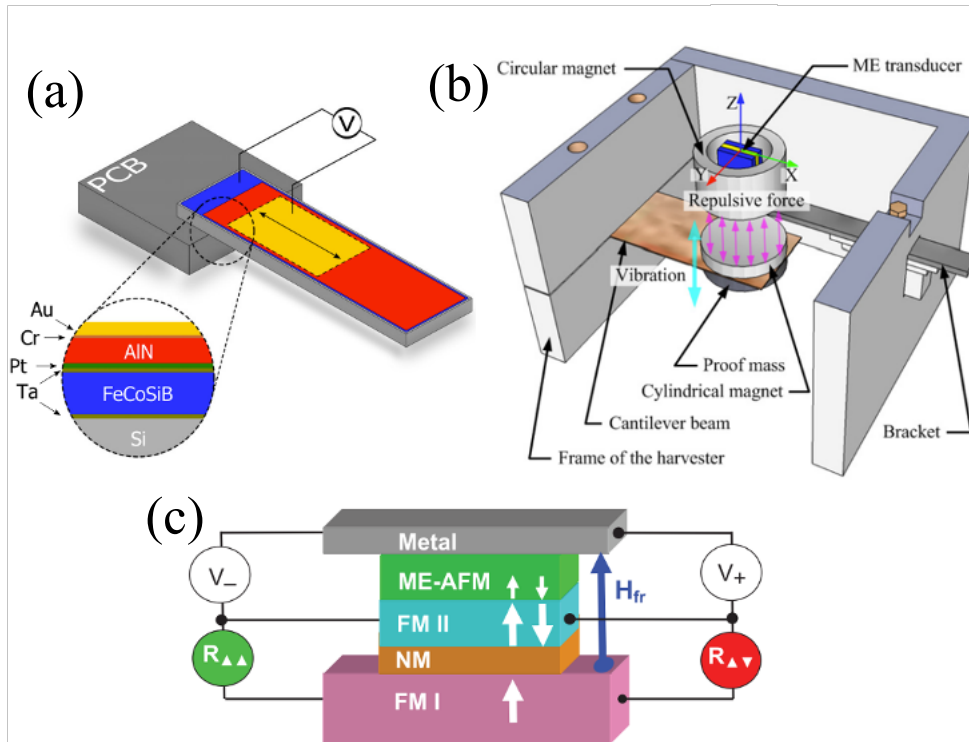


Figure 1.14: Microelectronic applications of ME Materials: (a) Si/SiO₂/Pt/AlN/FeCoSiB ME thin film magnetic field sensor⁷⁰; (b) ME energy harvester using Terfenol-D/PMNT/Terfenol-D plates⁷¹; (c) ME random access memory (MERAM) with a ME antiferromagnet (ME-AFM), a switchable ferromagnet (FM II), a non-magnetic barrier (NM) and a ferromagnet (FM I)⁷².

Magnetic Field Sensors

Magnetolectric materials are being implemented in magnetic field sensor applications due to their sensitivity, operating temperature independence, and ability to reduce magnetic noise generation by enhancing the magnetolectric coefficients or voltage gains^{73,74}. Magnetolectric magnetic field sensors can be used as magnetometers of different types (optically-pumped, giant magneto-impedance or fluxgate)⁷⁵. They have the ability to detect low frequency, resonant frequency, as well as DC magnetic fields. They can operate at room temperature, and also have relatively high sensitivity ($< pT/Hz^{1/2}$) which drastically reduces the cost of operation and also improves size restrictions and applicability. When a device such as the one in **Figure 1.14a** is exposed to a small magnetic field, the field induces the direct ME effect, creating polarization and a small current generation. Once the device is calibrated, this current gives a reading of the applied field⁷⁶⁻⁷⁸. In comparison, although devices such as superconducting quantum interference

devices (SQUID) (which are not magnetoelectric) have a better sensitivity, their use is limited by their high operational costs because of the need of cryogenic working temperatures and need for shielding to avoid interferences.

Energy Harvesters

Energy harvesting denotes the process in which forms of ambient energy, which would otherwise be wasted, are converted into a useful energy, usually an electric field. An example of neglected energy are electrical cables or electronic systems, where a parasitic magnetic field is induced due to current flow and electromagnetic induction (Faraday's law of induction). Conventional magnetic energy harvesters usually use coils to harvest the wasted magnetic field, which make them complex to implement. In the case of the ME harvesters (in **Figure 1.14b**), this limitation is negligible because they function using the direct ME effect, i.e., they use the parasitic magnetic fields to generate electricity, increasing efficiency, and alleviating size and frequency limitations⁷⁹⁻⁸¹.

Random Access Memory Devices

Currently, the vast majority of stored information is recorded by means of magnetic memories. However, the ME effect has been proven as a promising candidate in the field of data storage, and more specifically ME Random Access Memory Devices (ME-RAM), as illustrated in **Figure 1.14c**. By exploiting the inverse ME effect, these devices can be controlled using an externally applied electric field, with minimum heat losses and maximised speed and efficiency. It has been demonstrated⁸² that by changing the FE polarization of a ME material (e.g., BiFeO₃), the direction of the FM phase can be controlled. This is done via exchange coupling and is divided into two actions. Primarily, the ME coupling of the BiFeO₃ itself. Secondly, the interaction of the FE order of the BiFeO₃ with the FM order of a separate FM layer which induces magnetization^{71,83,84}. By incorporating the two phases, a non-volatile and fully reversible electric field-controlled ME memory can be implemented, with higher capacity, higher speed, and lower energy demand than conventional RAMs.

1.1.6.2. Biomedicine and Clinical Applications

In order to overcome the invasiveness of current therapeutic techniques and their associated health risks, researchers have shifted their focus towards investigating new, minimally- and non-invasive methods. ME heterostructures are a very promising candidate in a number of wireless clinical applications. Even though still in their early stages, a lot of studies (in vitro and in vivo) show their potential in terms of reduced invasiveness and increased efficacy and effectiveness (**Figure 1.15**).

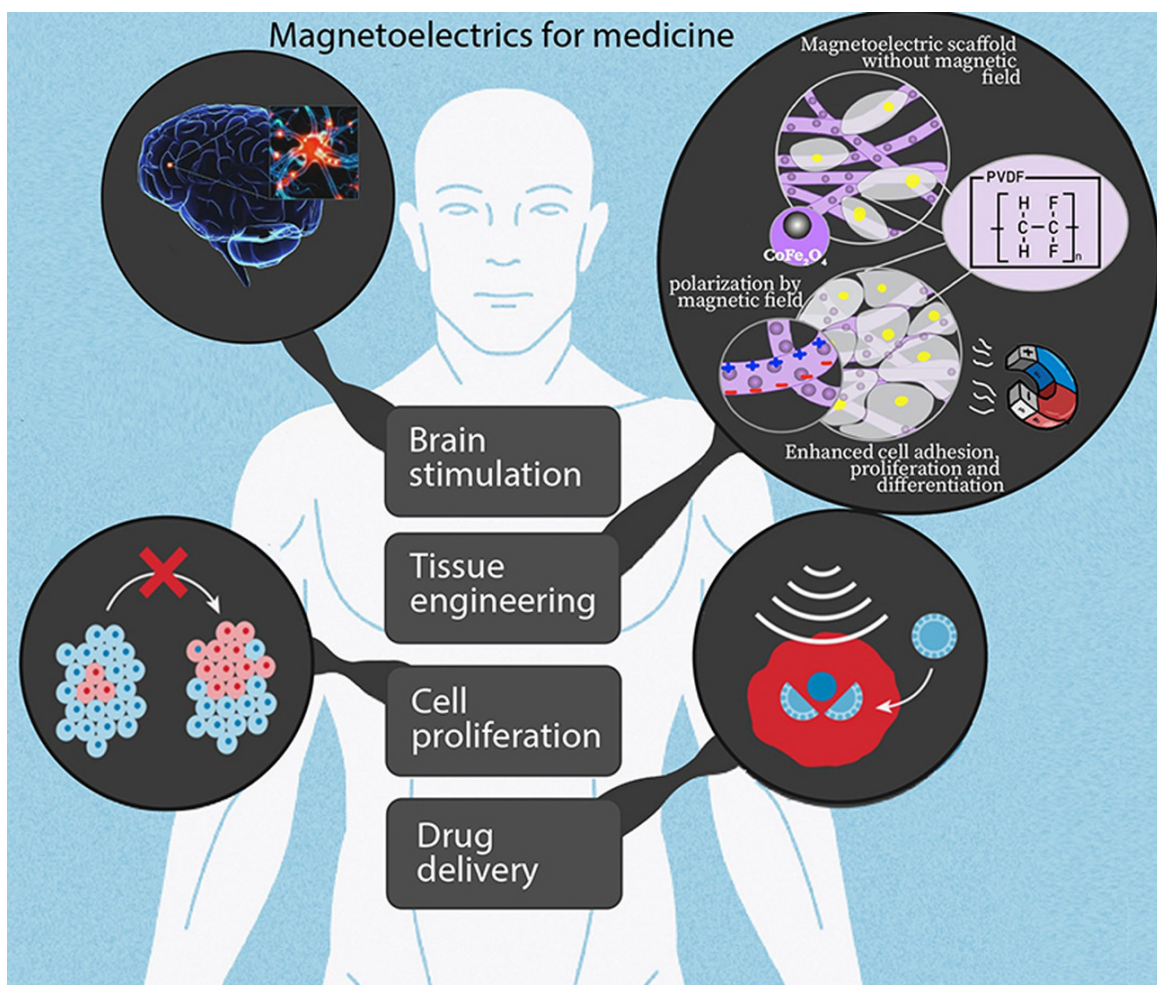


Figure 1.15. Graphic illustration of ME applications in biomedicine¹⁹

Brain Stimulation using ME Devices

One of the most promising, yet still in its infancy, biomedical application is wireless brain stimulation. This minimally-invasive technique has seen increasing interest over recent years with the development of more reliable, biocompatible and efficient ME devices. Currently, most of procedures which access the brain are highly invasive, which in itself can put the life or quality of life of a patient at risk by exposing them to infections and subsequent brain damage. Furthermore, these devices can be bulky due to the need of a battery to power them, which also needs replacing or recharging. Wireless brain stimulation can potentially pave the way to successful prevention and treatment of neurodegenerative diseases, such as

Parkinson's, ALS and other diseases related to primary and secondary defects of cell excitability and help with the recovery from strokes which can lead to partial or total paralysis.

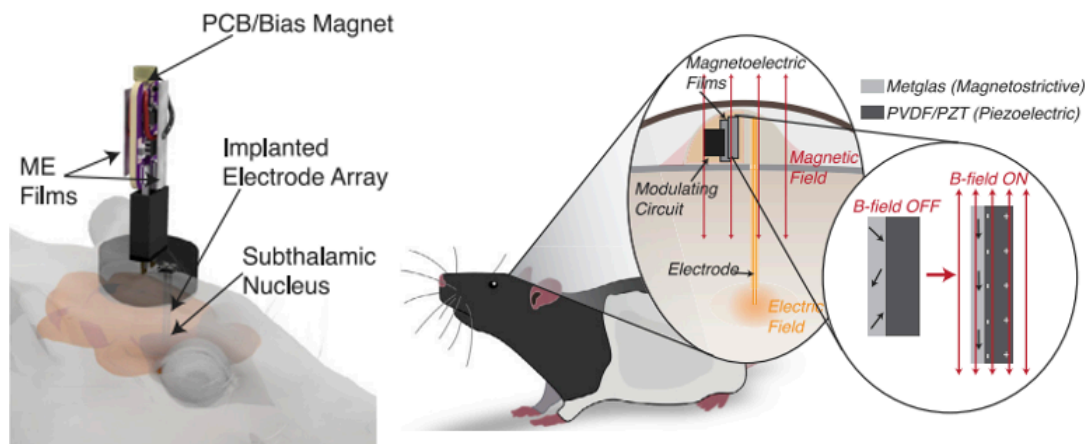


Figure 1.16. Illustration of a ME device and its components in a freely moving rat

Deep Brain Stimulation (DBS) has been proven to help with disorders such as Parkinson's, tremor, dystonia, and other neurodegenerative disorders which are caused by electrical signal misfiring within the brain^{85–87}. At a more localised level, ME devices can be used to treat diseases related to electrical brain activity. The principle of operation in this case is that the ME device is inserted in the brain either through the bloodstream via injection, or placed under the skin on top of the skull with a small incision (**Figure 1.16**). An externally-applied, low intensity, ac magnetic field is directed on the brain, which activates the ME effect and causes the generation of an electric charge of the same frequency in the device. The electric charge then interacts with the neurons, regulating electrical activity or causing them to create neural pathways faster and more effectively than they would do in an intrinsic manner. The ME effect in wireless brain stimulation is illustrated in **Figure 1.17**.

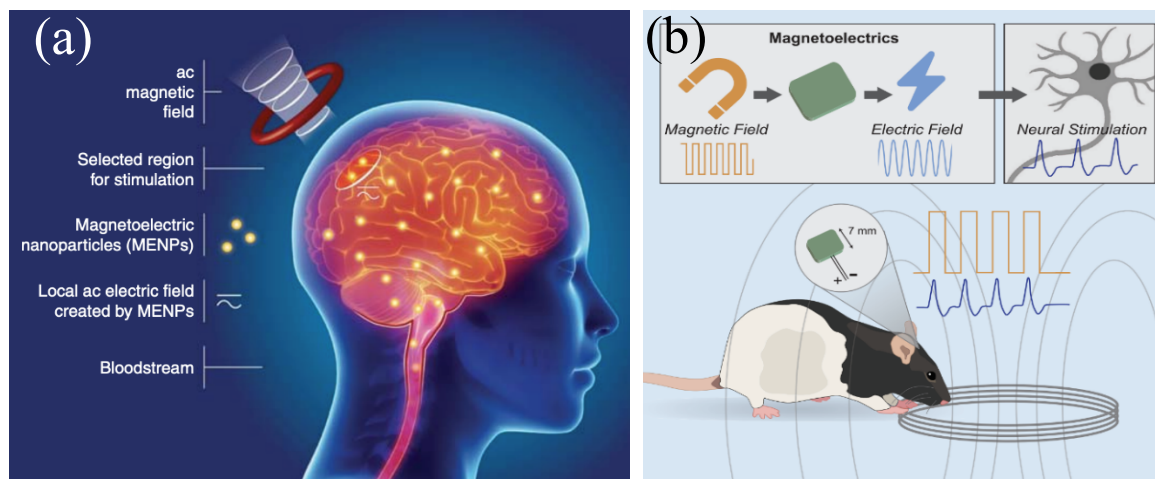


Figure 1.17. (a) Wireless ME stimulation using magnetolectric nanoparticles in ac magnetic fields⁸⁸; (b) Wireless deep brain stimulation in rodent model for Parkinson's disease⁸⁹

Drug Delivery

Cancer is nowadays one of the leading causes of death, according to the World Health Organisation (WHO)⁹⁰. Current therapeutic techniques tend to be very limited in terms of types of cancer that they can treat, and also their systemic approach causes damage to healthy cells which in turn can create other health problems.

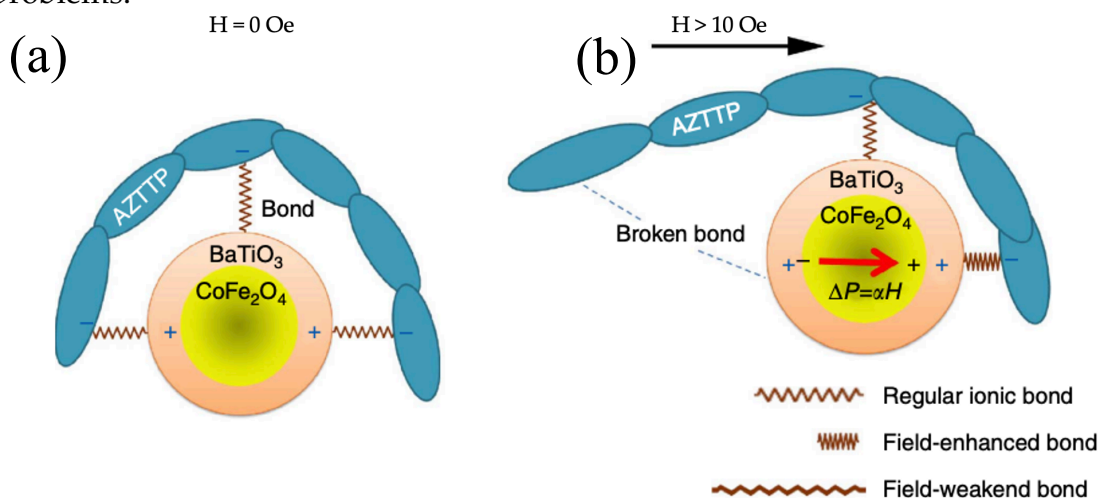


Figure 1.18. On-demand drug release using $\text{CoFe}_2\text{O}_4@/\text{BaTiO}_3$ magnetolectric nanoparticles using magnetic fields⁹¹.

Drug delivery using magnetolectric nanoparticles is an application of ME materials which offers site-specific and precise release of drugs for cancer treatment. The nanoparticles are loaded with the desired drug either by ionic bonding (as seen in **Figure 1.18** and **Figure 1.19**), or they are used as hollow core-shell nanocarriers^{93,94}. They are injected into the bloodstream and can then be wirelessly guided using a magnetic field. After reaching their destination organ, they are exposed to an alternating magnetic field which causes the ME effect and which due to the generated electric field breaks their ionic bonds and releases the drug directly onto

the site of action. Depending on the use and target of the nanoparticles, they can be manufactured in different shapes and sizes.

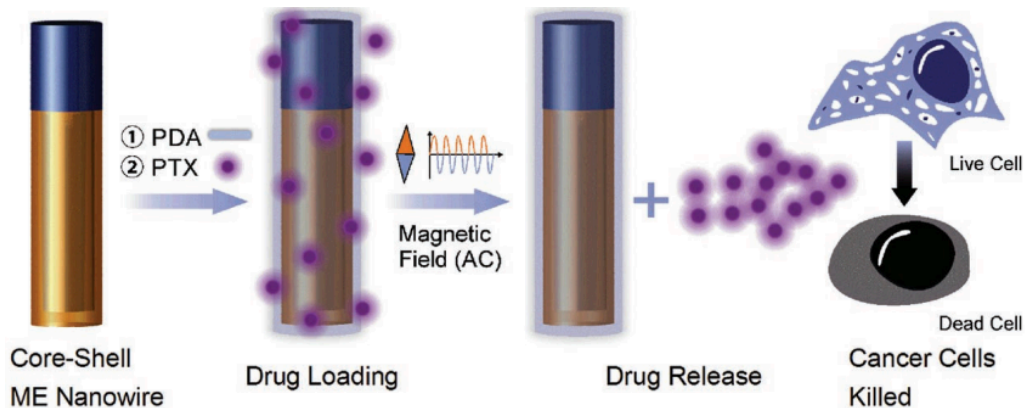


Figure 1.19. Anti-cancer drug delivery using ME bi-morph nanowire under magnetic fields⁹².

Cell Stimulation and Tissue Engineering

Numerous biological processes have electricity as the basic step to activate different responses. Thus, the ME effect has been proven as a strong candidate for tissue engineering. Currently, external biochemical methods for promoting human tissue (neuron, bone, etc.) regeneration include growth hormones formed during developmental embryogenesis. These external stimuli, even though effective, are held back by the slow speed with which they promote cell signalling. Furthermore, it has been previously shown that the application of a magnetic field activates surface receptors to promote cell activity^{93,94}. The polarization induced by the ME effect promotes further the activation and acceleration of cellular responses such as cell adhesion, proliferation and differentiation required for the process of regeneration, by increasing Ca contents^{95–98} as illustrated in **Figure 1.20**.

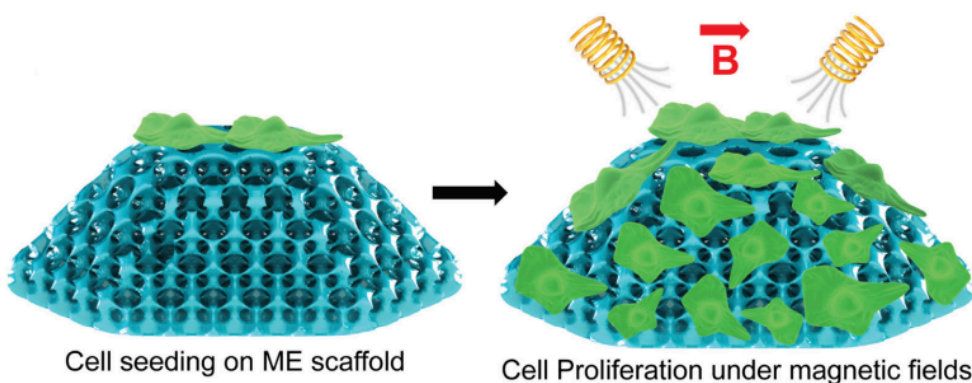


Figure 1.20. Enhanced cell proliferation under magnetic fields due to ME effect in 3D ME scaffold⁹⁹

1.2. REFERENCES

1. Schmid, H. Magnetic ferroelectric materials. *Bull Mater Sci* **17**, 1411–1414 (1994).
2. Spaldin, N. A. & Ramesh, R. Advances in magnetoelectric multiferroics. *Nat Mater* **18**, 203–212 (2019).
3. Vopson, M. M. Fundamentals of Multiferroic Materials and Their Possible Applications. *Crit Rev Solid State Mater Sci* **40**, 223–250 (2015).
4. Spaldin, N. A. & Fiebig, M. The Renaissance of Magnetoelectric Multiferroics. *Science* **309**, 391–392 (2005).
5. Khojah, R. *et al.* Single-Domain Multiferroic Array-Addressable Terfenol-D (SMArT) Micromagnets for Programmable Single-Cell Capture and Release. *Adv Mater* **33**, 2006651 (2021).
6. Martin, L. W. *et al.* Multiferroics and magnetoelectrics: thin films and nanostructures. *J Phys Condens Matter* **20**, 434220 (2008).
7. Eerenstein, W., Mathur, N. D. & Scott, J. F. Multiferroic and magnetoelectric materials. *Nature* **442**, 759–765 (2006).
8. Röntgen, W. C. Ueber die durch Bewegung eines im homogenen electrischen Felde befindlichen Dielectricums hervorgerufene electro-dynamische Kraft. *AdP* **271**, 264–270 (1888).
9. Fiebig, M. Revival of the magnetoelectric effect. *J Phys D Appl Phys* **38**, R123–R152 (2005).
10. Curie, P. Sur la symétrie dans les phénomènes physiques, symétrie d'un champ électrique et d'un champ magnétique. *J Phys Theor Appl* **3**, 393–415 (1894).
11. Debye, P. Bemerkung zu einigen neuen Versuchen über einen magneto-elektrischen Richteffekt. *Z Phys* **36**, 300–301 (1926).
12. Wilson, H. III. On the electric effect of rotating a dielectric in a magnetic field. *Philos Trans R Soc Lond Ser A* **204**, 121–137 (1905).
13. Rado, G. T. & Folen, V. J. Magnetoelectric Effects in Antiferromagnetics. *J Appl Phys* **33**, 1126–1132 (1962).
14. Rado, G. T. & Folen, V. J. Observation of the Magnetically Induced Magnetoelectric Effect and Evidence for Antiferromagnetic Domains. *Phys Rev Lett* **7**, 310–311 (1961).
15. Folen, V. J., Rado, G. T. & Stalder, E. W. Anisotropy of the Magnetoelectric Effect in Cr₂O₃. *Phys Rev Lett* **6**, 607–608 (1961).
16. Astrov, D. The magnetoelectric effect in antiferromagnetics. *Sov Phys JETP* **11**, 708–709 (1960).
17. Dzyaloshinskii, I. On the Magneto-Electrical Effect in Antiferromagnets. *Zh Eksp Teor Fiz* **37**, 628–629 (1960).
18. Eerenstein, W., Mathur, N. D. & Scott, J. F. Multiferroic and magnetoelectric materials. *Nature* **442**, 759–765 (2006).

19. Kopyl, S., Surmenev, R., Surmeneva, M., Fetisov, Y. & Kholkin, A. Magnetoelectric effect: principles and applications in biology and medicine—a review. *Mater Today Bio* **12**, 100149 (2021).
20. Das, R. Study of Magnetic, Ferroelectric and Magnetoelectric properties in bulk and nanostructured Multiferroics. (University of Calcutta, 2013).
21. Khomskii, D. Classifying multiferroics: Mechanisms and effects. *Physics (College Park Md)* **2**, 20 (2009).
22. Spaldin, N. A. & Ramesh, R. Advances in magnetoelectric multiferroics. *Nat Mater* **18**, 203–212 (2019).
23. Fina Martínez, I. Ferroelectricity and magnetoelectric coupling in magnetic ferroelectrics and artificial multiferroic heterostructures. PhD Thesis (Universitat de Barcelona, 2012).
24. Wang, J. (Ed.). Multiferroic Materials: Properties, Techniques, and Applications. (CRC Press, 2016).
25. Allahyarov, E. *et al.* Nano/Micro-Structured Materials for Energy and Biomedical Applications. vol. 4 (Springer Singapore, 2018).
26. M. Rabe, K. (Ed.), H. Ahn, C. (Ed.) & Triscone, J.-M. (Ed.). Physics of Ferroelectrics: A Modern Perspective. (Springer, 2007).
27. Olsen, G. H., Sørby, M. H., Selbach, S. M. & Grande, T. Role of Lone Pair Cations in Ferroelectric Tungsten Bronzes. *Chem Mater* **29**, 6414–6424 (2017).
28. Cheong, S.-W. & Mostovoy, M. Multiferroics: a magnetic twist for ferroelectricity. *Nat Mater* **6**, 13–20 (2007).
29. Eerenstein, W., Mathur, N. D. & Scott, J. F. Multiferroic and magnetoelectric materials. *Nature* **442**, 759–765 (2006).
30. Shen, Y. *et al.* Role of Lone-Pairs in Driving Ferroelectricity of Perovskite Oxides: An Orbital Selective External Potential Study. *Adv Theory Simul* **2**, 1900029 (2019).
31. Fiebig, M., Lottermoser, T., Meier, D. & Trassin, M. The evolution of multiferroics. *Nat Rev Mater* **1**, 16046 (2016).
32. Van Aken, B. B., Palstra, T. T. M., Filippetti, A. & Spaldin, N. A. The origin of ferroelectricity in magnetoelectric YMnO_3 . *Nat Mater* **3**, 164–170 (2004).
34. Tohei, T. *et al.* Geometric ferroelectricity in rare-earth compounds RGaO_3 and RInO_3 . *Phys Rev B* **79**, 144125 (2009).
35. Kimura, T. *et al.* Magnetic control of ferroelectric polarization. *Nature* **426**, 55–58 (2003).
36. Hur, N. *et al.* Electric polarization reversal and memory in a multiferroic material induced by magnetic fields. *Nature* **429**, 392–395 (2004).
37. Kimura, T. Spiral Magnets as Magnetoelectrics. *Annu Rev Mater Res* **37**, 387–413 (2007).
38. Picozzi, S. & Stroppa, A. Advances in ab-initio theory of multiferroics. *Eur Phys J B* **85**, 240 (2012).
39. Tokura, Y., Seki, S. & Nagaosa, N. Multiferroics of spin origin. *Rep Prog Phys* **77**, 076501 (2014).

40. Hu, J.-M., Chen, L.-Q. & Nan, C.-W. Multiferroic Heterostructures Integrating Ferroelectric and Magnetic Materials. *Adv Mater* **28**, 15–39 (2016).
41. Wang, Y., Hu, J., Lin, Y. & Nan, C.-W. Multiferroic magnetoelectric composite nanostructures. *NPG Asia Mater* **2**, 61–68 (2010).
42. Ma, J., Pei, Y., Sun, Y., Li, F. & Fang, D. Wrinkles of magnetoelectric composite thin films bonded on compliant buffer-layers. *J Appl Phys* **115**, 083515 (2014).
43. Wang, S., Shan, Z. & Huang, H. The Mechanical Properties of Nanowires. *Adv Sci* **4**, 1600332 (2017).
44. Kim, D. *et al.* Magnetoelectric coupling in micropatterned BaTiO₃/CoFe₂O₄ epitaxial thin film structures: Augmentation and site-dependency. *Appl Phys Lett* **119**, 012901 (2021).
45. Almusallam, A. *et al.* Clamping effect on the piezoelectric responses of screen-printed low temperature PZT/Polymer films on flexible substrates. *Smart Mater Struct* **24**, 115030 (2015).
46. Enea, N., Ion, V., Moldovan, A., Bonciu, A. & Scarisoreanu, N. D. Piezoelectric Hybrid Heterostructures PVDF/(Ba,Ca)(Zr,Ti)O₃ Obtained by Laser Techniques. *Coatings* **10**, 1155 (2020).
47. Curie, J. & Curie, P. Développement par compression de l'électricité polaire dans les cristaux hémiedres à faces inclinées. *Bull Soc Minéral. Fr.* **3**, 90–93 (1880).
48. Ahmed, R., Mir, F. & Banerjee, S. A review on energy harvesting approaches for renewable energies from ambient vibrations and acoustic waves using piezoelectricity. *Smart Mater Struct* **26**, 085031 (2017).
49. Trolrier-McKinstry, S. Crystal Chemistry of Piezoelectric Materials. in *Piezoelectric and Acoustic Materials for Transducer Applications* vol. 3 39–56 (Springer US, 2008).
50. Mishra, S., Unnikrishnan, L., Nayak, S. K. & Mohanty, S. Advances in Piezoelectric Polymer Composites for Energy Harvesting Applications: A Systematic Review. *Macromol Mater Eng* **304**, 1800463 (2019).
51. Curie, J. & Curie, P. Contractions et dilatations produites par des tensions électriques dans les cristaux hémiedres à faces inclinées. *Compt. Rend* **93**, 1137–1140 (1881).
52. Korkmaz, S. & Kariper, I. A. BaTiO₃-based nanogenerators: fundamentals and current status. *J Electroceram* **48**, 8–34 (2022).
53. Neppiras, E. A. Piezoelectric ceramics 1971. *J Sound Vib* **20**, 562–563 (1972).
54. Zhang, S., Malič, B., Li, J.-F. & Rödel, J. Lead-free ferroelectric materials: Prospective applications. *J Mater Res* **36**, 985–995 (2021).
55. Priya, S. *et al.* A Review on Piezoelectric Energy Harvesting: Materials, Methods, and Circuits. *Energy Harvesting Syst* **4**, 3–39 (2019).
56. Acosta, M. *et al.* BaTiO₃-based piezoelectrics: Fundamentals, current status, and perspectives. *Appl Phys Rev* **4**, 041305 (2017).

57. Zhang, Q., Cagin, T. & Goddard, W. A. The ferroelectric and cubic phases in BaTiO₃ ferroelectrics are also antiferroelectric. *Proc Nat Acad Sci USA* **103**, 14695–14700 (2006).
58. Stefani, C. Mechanical and electromechanical properties of ferroelectrics at the nanoscale studied by Atomic Force Microscopy. PhD Thesis (Universitat Autònoma de Barcelona, 2022).
59. Coey, J. M. D. Magnetism and hysteresis. (Cambridge University Press, 2009).
60. Spain, E. & Venkatanarayanan, A. Review of Physical Principles of Sensing and Types of Sensing Materials. *Compr Mater Process* **13**, 5–46 (2014).
61. Néel, L. Antiferromagnetism and Ferrimagnetism. *Proc Phys Soc Sec A* **65**, 869–885 (1952).
62. Joule, J. P. On the effects of magnetism upon the dimensions of iron and steel bars. *Lond. Edinb. Dublin Philos Mag J Sci* **30**, 76–87 (1847).
63. Ekreem, N. B., Olabi, A. G., Prescott, T., Rafferty, A. & Hashmi, M. S. J. An overview of magnetostriction, its use and methods to measure these properties. *J Mater Process Technol* **191**, 96–101 (2007).
64. James, R. D. & Wuttig, M. Magnetostriction of martensite. *Philos Mag A* **77**, 1273–1299 (1998).
65. Dapino, M. J. On magnetostrictive materials and their use in adaptive structures. *Struct Eng Mech* **17**, 303–329 (2004).
66. Hall, D. L. & Flatau, A. B. Broadband Performance of a Magnetostrictive Shaker. *J Intell Mater Syst Struct* **6**, 109–116 (1995).
67. Bras, Y. le & Greneche, J.-M. Magneto-Elastic Resonance: Principles, Modeling and Applications. in *Resonance* (InTech, 2017).
68. Nataf, G. F. *et al.* Domain-wall engineering and topological defects in ferroelectric and ferroelastic materials. *Nat Rev Phys* **2**, 634–648 (2020).
69. Hristoforou, E. & Ktena, A. Magnetostriction and magnetostrictive materials for sensing applications. *J Magn Magn Mater* **316**, 372–378 (2007).
70. Leung, C. M., Li, J., Viehland, D. & Zhuang, X. A review on applications of magnetoelectric composites: from heterostructural uncooled magnetic sensors, energy harvesters to highly efficient power converters. *J Phys D Appl Phys* **51**, 263002 (2018).
71. Kleemann, W. Magnetoelectric spintronics. *J Appl Phys* **114**, 027013 (2013).
72. Naifar, S., Bradai, S., Viehweger, C. & Kanoun, O. Survey of electromagnetic and magnetoelectric vibration energy harvesters for low frequency excitation. *Measurement* **106**, 251–263 (2017).
73. Bichurin, M. *et al.* Magnetoelectric Magnetic Field Sensors: A Review. *Sensors* **21**, 6232 (2021).
74. Wang, Y., Li, J. & Viehland, D. Magnetoelectrics for magnetic sensor applications: status, challenges and perspectives. *Mater Today* **17**, 269–275 (2014).
75. Gao, J. *et al.* Review of Magnetoelectric Sensors. *Actuators* **10**, 109 (2021).

76. Srinivasan, G. Magnetoelectric Composites. *Annu Rev Mater Res* **40**, 153–178 (2010).
77. Nan, C.-W., Bichurin, M. I., Dong, S., Viehland, D. & Srinivasan, G. Multiferroic magnetoelectric composites: Historical perspective, status, and future directions. *J Appl Phys* **103**, (2008).
78. Lawes, G. & Srinivasan, G. Introduction to magnetoelectric coupling and multiferroic films. *J Phys D Appl Phys* **44**, 243001 (2011).
79. Ghosh, S. K. *et al.* Rollable Magnetoelectric Energy Harvester as a Wireless IoT Sensor. *ACS Sustain Chem Eng* **8**, 864–873 (2020).
80. Bai, X. *et al.* A magnetoelectric energy harvester with the magnetic coupling to enhance the output performance. *J Appl Phys* **111**, 07A938 (2012).
81. Zhou, Y. *et al.* Magnetoelectric energy harvester in *Composite Magnetoelectrics* (Woodhead Publishing, 2015) p. 161-207.
82. Lebeugle, D., Mougin, A., Viret, M., Colson, D. & Ranno, L. Electric Field Switching of the Magnetic Anisotropy of a Ferromagnetic Layer Exchange Coupled to the Multiferroic Compound BiFeO₃. *Phys Rev Lett* **103**, 257601 (2009).
83. Åkerman, J. Toward a Universal Memory. *Science* **308**, 508–510 (2005).
84. Parkin, S. S. P., Hayashi, M. & Thomas, L. Magnetic Domain-Wall Racetrack Memory. *Science* **320**, 190–194 (2008).
85. Kringelbach, M. L., Jenkinson, N., Owen, S. L. F. & Aziz, T. Z. Translational principles of deep brain stimulation. *Nat Rev Neurosci* **8**, 623–635 (2007).
86. Ashkan, K., Rogers, P., Bergman, H. & Ughratdar, I. Insights into the mechanisms of deep brain stimulation. *Nat Rev Neurol* **13**, 548–554 (2017).
87. Visser-Vandewalle, V. *et al.* Deep brain stimulation for obsessive–compulsive disorder: a crisis of access. *Nat Med* **28**, 1529–1532 (2022).
88. Khizroev, S. Technobiology’s Enabler: The Magnetoelectric Nanoparticle. *Cold Spring Harb Perspect Med* **9**, a034207 (2019).
89. Singer, A. *et al.* Magnetoelectric Materials for Miniature, Wireless Neural Stimulation at Therapeutic Frequencies. *Neuron* **107**, 631-643 (2020).
90. World Health Organization (WHO). The top 10 causes of death. <https://www.who.int/news-room/fact-sheets/detail/the-top-10-causes-of-death> (Accessed May 10, 2023).
91. Nair, M. *et al.* Externally controlled on-demand release of anti-HIV drug using magneto-electric nanoparticles as carriers. *Nat Commun* **4**, 1707 (2013).
92. Chen, X.-Z. *et al.* Hybrid Magnetoelectric Nanowires for Nanorobotic Applications: Fabrication, Magnetoelectric Coupling, and Magnetically Assisted In Vitro Targeted Drug Delivery. *Adv Mater* **29**, 1605458 (2017).
93. Zhu, Y. *et al.* Protein Corona of Magnetic Hydroxyapatite Scaffold Improves Cell Proliferation via Activation of Mitogen-Activated Protein Kinase Signaling Pathway. *ACS Nano* **11**, 3690–3704 (2017).

94. Huang, H.-M., Lee, S.-Y., Yao, W.-C., Lin, C.-T. & Yeh, C.-Y. Static Magnetic Fields Up-regulate Osteoblast Maturity by Affecting Local Differentiation Factors. *Clin Orthop Relat Res* **447**, 201–208 (2006).
95. Arjmand, M., Ardeshirylajimi, A., Maghsoudi, H. & Azadian, E. Osteogenic differentiation potential of mesenchymal stem cells cultured on nanofibrous scaffold improved in the presence of pulsed electromagnetic field. *J Cell Physiol* **233**, 1061–1070 (2018).
96. Wang, J. *et al.* The effects of pulsed electromagnetic field on the functions of osteoblasts on implant surfaces with different topographies. *Acta Biomater* **10**, 975–985 (2014).
97. Fernandes, M. M. *et al.* Bioinspired Three-Dimensional Magnetoactive Scaffolds for Bone Tissue Engineering. *ACS Appl Mater Interfaces* **11**, 45265–45275 (2019).
98. Shuai, C. *et al.* A magnetic micro-environment in scaffolds for stimulating bone regeneration. *Mater Des* **185**, 108275 (2020).
99. Mushtaq, F. *et al.* Magnetoelectric 3D scaffolds for enhanced bone cell proliferation. *Appl Mater Today* **16**, 290–300 (2019).

2. Introduction to Human Electrophysiology

2.1. PHYSIOLOGY OF EXCITABLE TISSUES

The first suggestion that electricity existed in biological systems, was made by Luigi Galvani, who in 1789 performed experiments on frog cadavers. He would expose the sciatic nerve in the leg of the frog, and by touching the nerve with an electrically charged scalpel, he noted muscle movements. He concluded that these contractions, under circumstances which the animal was alive, came from electricity being produced by the animal itself, intrinsically¹. Alessandro Volta, after repeating Galvani's experiments, had doubts about this conclusion, and supported that, even though electrical current did cause muscle contractions, it did not originate from the animal intrinsically. Rather, he believed that an electrical potential existed within tissues which originated from dissimilar metals².

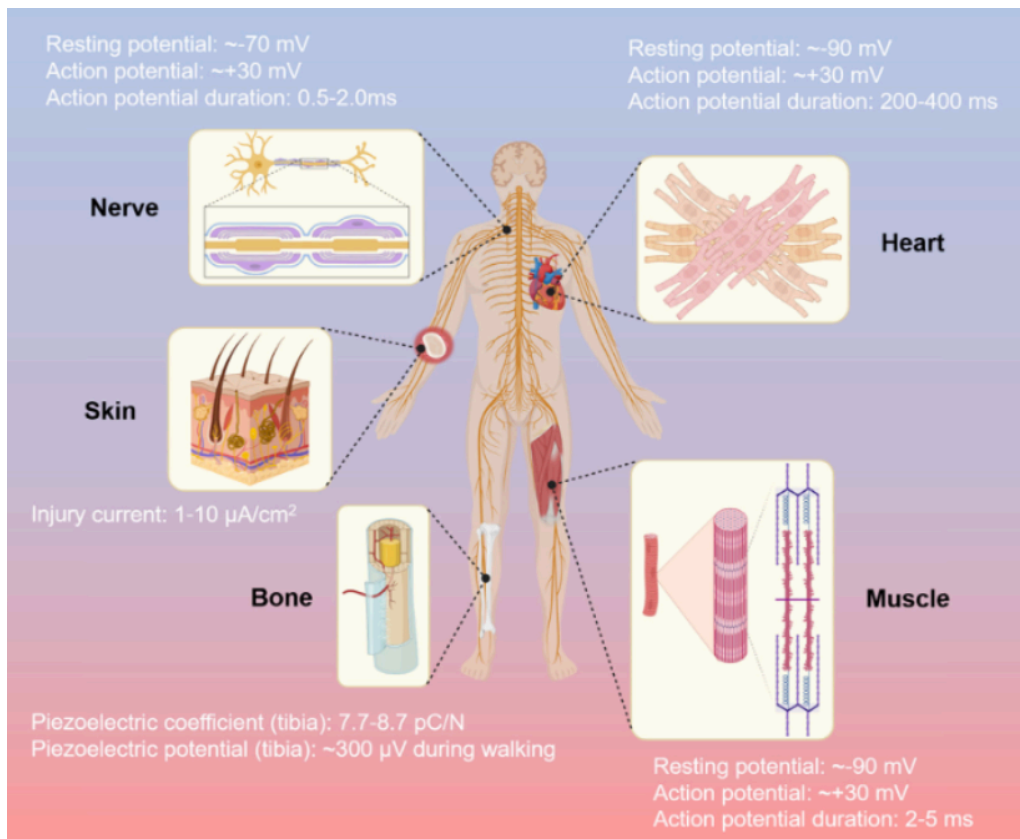


Figure 2.1. Electrical activity in the human body³

The human body is a “machine” which operates using a complex orchestration of bioelectrical signals and biological functions within tissues and cells as observed in **Figure 2.1**. Excitability of excitable tissues refers to the ability of these cells to respond to mechanical and electrochemical stimuli.

There are three main types of excitable cells. These include neurons, muscle cells (Myocytes)⁴, and some cells from the endocrine system (insulin-releasing pancreatic β cell).

Neurons are the main components of the central nervous system, and their function is to transmit and receive information via electrical and chemical signalling. As illustrated in **Figure 2.2**, they are comprised of three main parts: (a) the **soma** (cell body) which contains the nucleus of the neuron and maintains its viability, (b) the **dendrites** which receive signals from neighbouring cells and relay the signals to the soma, and (c) the **axon** which is used to transmit signals towards other neurons or muscle cells. Based on their stimuli and function, they are differentiated between: (a) **sensory neurons** which are stimulated by environmental means such as touch, taste, smell and sight, relaying information to the central nervous system; (b) **motor neurons**, which are responsible for relaying information and electrical signals from the brain down the spinal cord and to muscles, and (c) **interneurons**, which enable the interconnection of neurons (sensory, motor and other interneurons), thus creating complex neural circuits between the brain, the spinal cord and the organs⁵⁻¹⁰.

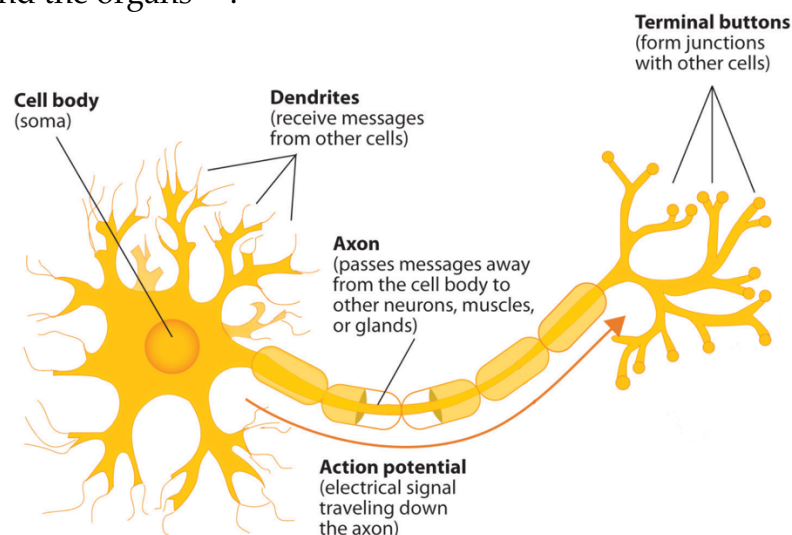


Figure 2.2: Neuron components¹¹

Myocytes are cells found in muscle tissue and function using electrical impulses which cause contraction within the muscle. They can be divided into three subcategories based on their function: (a) skeletal myocytes, (b) cardiac myocytes and (c) smooth muscle cells. These are illustrated in **Figure 2.3**.

Skeletal myocytes are found in muscle attached to bones via connective tissue (tendons) and are responsible for controlling voluntary body locomotion. This motion is controlled by the brain, which sends electrical signals to the muscle via neurons, causing muscle contraction¹²⁻¹⁵.

Cardiac myocytes are found in the wall linings of the heart. This type of muscle tissue does not need external stimulation. They function intrinsically, hence inducing the involuntary sequential beating of the heart (self-contraction)¹⁶⁻¹⁸.

Smooth muscle cells also function in an involuntary manner. They are found in the wall linings of organs which partake in systems including the digestive, reproductive, urinary, and respiratory, and also in blood vessels^{19,20}.

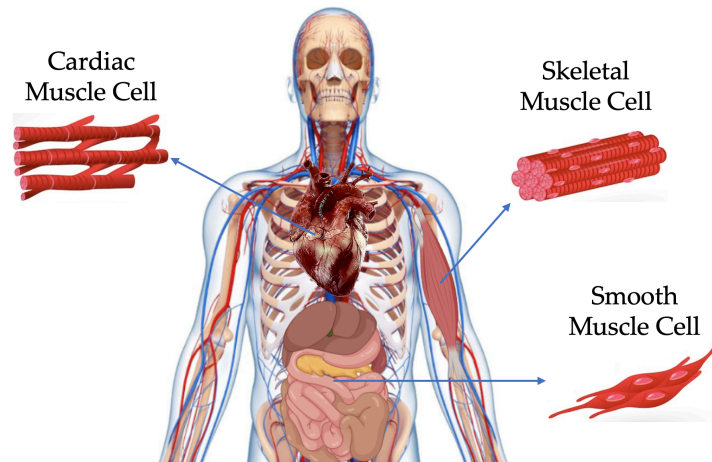


Figure 2.3: Types of muscle tissue²¹

The *endocrine system* is a multiplexed arrangement of glands which are responsible for secreting hormones from endocrine organs that travel along the bloodstream to other organs which control physiological and behavioural activities^{22,23}. The secretion of hormones is a response to different stimuli, including electrical signals. An example of endocrine cells are the pancreatic β -cells used to produce insulin and amylin that reduce glucose in the bloodstream. Voltage-gated Ca^{2+} channels in the membrane of the cells are activated by the generation of an action potential when the concentration of glucose exceeds a limit²⁴⁻²⁶.

2.2. MECHANISMS OF EXCITABLE CELLS

Excitable cells regulate the electrical activity and bodily functions of our bodies. This is done by the generation of action potentials, which allows electrical impulses to propagate across the human body, creating an intricate network of electrical signalling mechanisms. One of the key components of these cells is the cell membrane. The different ion concentrations between two sides of the cell membrane are what ultimately guarantees a normal bodily function. Degenerative diseases which affect the central nervous system, are directly linked with the malfunction of cell excitability.

Although excitable cells generate action potentials and regulate bodily functions, non-excitable cells, like bone and skin cells also respond to electric fields. While they lack the ability to transmit electrical signals, these cells are sensitive to electric fields in their environment. Bone cells, such as osteocytes, respond to electric fields by influencing bone formation and repair processes, while skin cells, like keratinocytes, display responses that affect cell migration, wound healing, and the release of growth factors. These facts highlight the complex relationship between electric

fields and cellular functions, offering insights into, for example, tissue homeostasis, regeneration, and disease mechanisms^{4,27, 28}.

2.2.1. Cell Membrane

All cells contain a semi-permeable membrane known as the *cell membrane*. The cell membrane separates the interior (intracellular) part from the exterior (extracellular) part of the cell and is composed of a double layer of phospholipids made of the hydrophobic tail and the hydrophilic head parts as in **Figure 2.4b**.

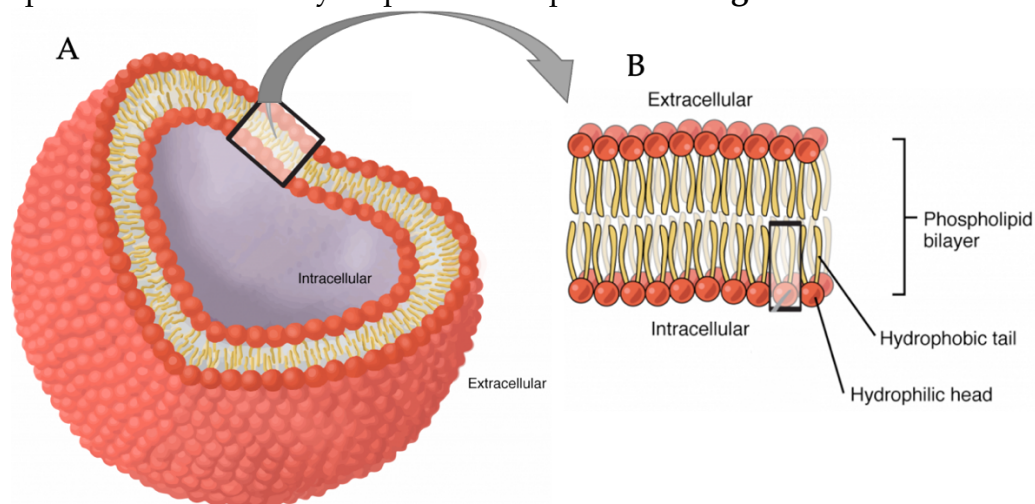


Figure 2.4: Cell membrane: (a) The normal form of a cell; (b) Cell membrane cross-section consisting of the phospholipid layers, the hydrophobic tail, and the hydrophilic head²⁹

The cell membrane protects the cell from the outside environment and also provides its structure and shape, in order to form tissues. It also regulates the flow of substances between the inside and the outside of the cell itself. Mainly, it regulates the flow of *ions* by means of *ion channels* in order to control the *resting membrane potential*, or to induce controlled membrane potential changes, thus enabling physiological processes such as contraction of muscle tissues, neurotransmitter (signalling molecule) release, nerve impulses, etc.

2.2.2. Ion Channels and Resting Membrane Potential

Ion channels are protein molecules integrated in the cell membrane whose function is to regulate the ions' migration from one side of the cell membrane to the other. This regulation occurs by the opening and closing of the channel, which depending on their responses to different stimuli, have different activation methods. They can be divided into 4 categories: (a) Ligand-gated ion channels; (b) mechanically-gated ion channels; (c) leakage-gated ion channels and (d) voltage-gated ion channels, illustrated in **Figure 2.5**^{30,31}.

Ligand-gated Channels

Ligand-gated ion channels are opened when a neurotransmitter receptor or another chemical ligand binds to it. This changes the protein structure of the channel and allows ion flow. They are found mainly in the nerve cells, neurons, and myocytes.

Mechanically-gated Channels

Found in sensory receptors (eyes, ears, nose and mouth), mechanically-gated channels respond to temperature, pressure or mechanical vibrations caused by external means such as touch or sound waves. They convert these stimuli into electrical signals.

Non-gated Leakage Channels

The non-gated ion channels are always open. Ions are allowed to migrate between the two sides of the membrane freely.

Voltage-gated Channels

Voltage-gated channels' permeability is influenced in response to changes in the *membrane potential* caused mostly by *action potentials*. They are very selective and allow the flow of only one type of ion in the channel (Na^+ channel, K^+ channel). These channels enable external electrostimulation to regulate biological processes, with the introduction of an applied external voltage. They can be found in cells such as neurons and muscle cells, but also in non-excitable cells such as osteoblasts, which have been reported to have types of Ca^{2+} channels³².

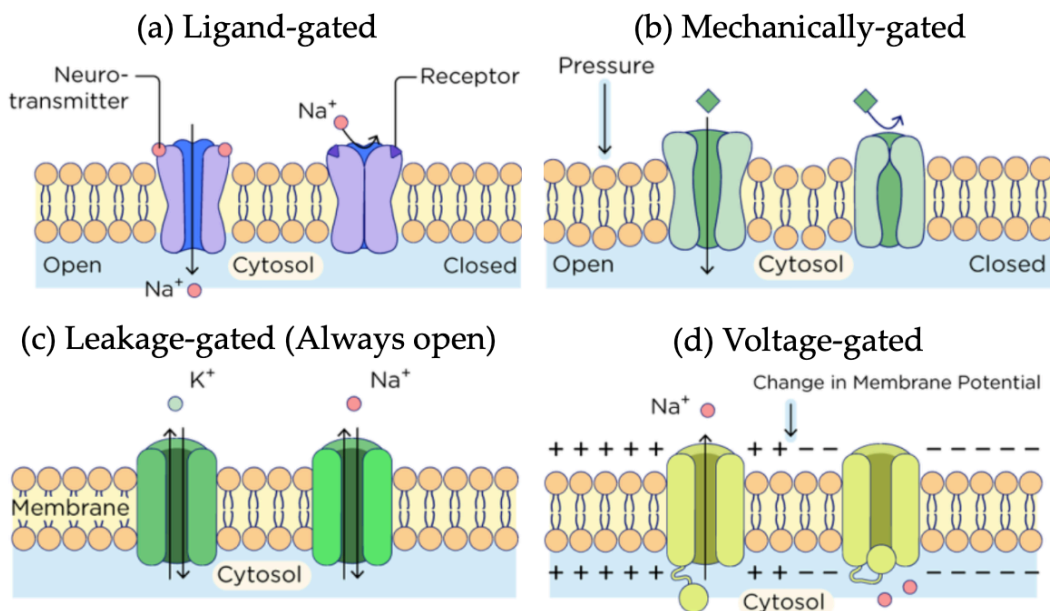


Figure 2.5: Ion channel types: (a) Ligand-gated ion channel; (b) Mechanically-gated ion channel; (c) Leakage ion channel; (d) Voltage-gated ion channel³³

One of the most important functions of ion channels is to maintain the *resting membrane potential* and generating controlled voltage changes by regulating the intracellular and extracellular ion concentrations, as tabulated in **Table 1**. The ions

around the cell membrane include Na^+ sodium, K^+ potassium, Ca^{2+} calcium, and Cl^- chloride. These elements have a specific electrical charge, and they are used to generate electrical impulses which regulate the normal function of all organs³⁴⁻³⁷. The difference between intracellular and extracellular concentration of ions is what creates the *resting membrane potential*.

Ion	Intracellular Concentration (mM)	Extracellular Concentration (mM)	Ratio
Na^+	12	145	~ 12
K^+	155	4	$\sim 40^{-1}$
Ca^{2+}	$< 10^{-4}$	1.5	$\sim 10^4$
Cl^-	4.2	123	~ 30

Table 1: Ion Concentrations in mammalian myocytes³⁸

A *membrane potential* is found between the extracellular and the intracellular part of all biological cells due to the different concentration of ions inside and outside the cells (Table 1), and it depends on the distribution of ions across the cell membrane, as well as the membrane permeability as observed in **Figure 2.6**.

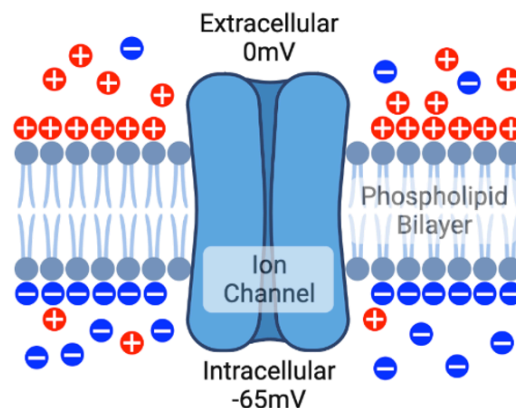


Figure 2.6: Charge separation between phospholipid layers³¹

When the cell is in a resting (normal) phase, a voltage difference across the phospholipid layers between 60 to 80 mV is observed, which is known as the *resting membrane potential*. Therefore, the whole structure forms a capacitor and the phospholipid layers act as the capacitor's dielectric layer³¹. The ion channels are also responsible for triggering and controlling action potentials.

2.2.3. Action Potentials

An *action potential* is a rapid event where an electrical impulse causes the cell membrane to depolarize and repolarize in a very short time period. It can be thought of as a method of communication of excitable tissue using electrical signals, and allows for muscle contractions in myocytes, and neuron and endocrine cell intercommunication. The action potential can be divided into four phases as seen in

Figure 2.7: (A) resting membrane potential, (B) membrane depolarization, (C) membrane repolarization and (D) membrane hyperpolarization^{39,40}.

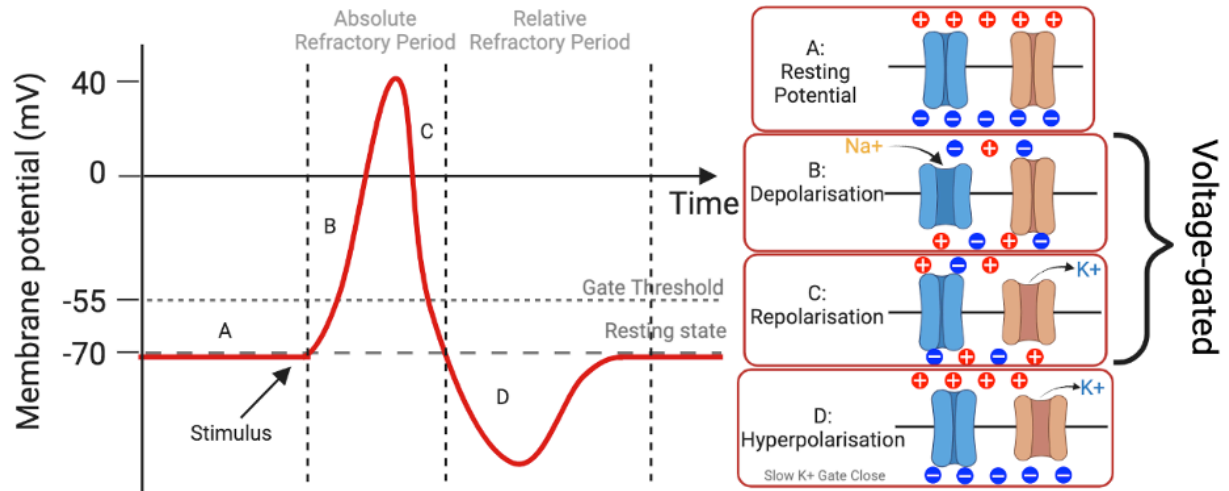


Figure 2.7: Schematic of an idealised action potential event

Action Potential Phases:

- (A) *Resting Membrane Potential:* In this phase, the membrane potential is at its normal phase without any electrical excitation.
- (B) *Membrane Depolarization:* As soon as the electrical impulse event occurs, Na^+ channels open, allowing positive Na^+ ions to enter the cell. This increase in positive ions increases the membrane potential until the gate threshold is reached, activating more sodium channels, and the action potential is rapidly created.
- (C) *Membrane Repolarization:* As soon as the cell membrane potential reaches its peak value, Na^+ channels start closing, and at the same time K^+ channels start opening, allowing for the positive ions to exit the cell's interior, causing a rapid voltage drop, back to the negative region.

The time period which depolarization and repolarization occur is called *Absolute Refractory Period* and it lasts between 2 and 4 ms for myocytes and between 1 and 2 ms for neurons.

- (D) *Membrane Hyperpolarization:* As the K^+ channels do not close instantly after repolarization, a potential undershoot is observed as an excess of K^+ ions exit the cell. As they start to close, the membrane potential returns to the resting phase.

The time period which hyperpolarization occurs is called *Relative Refractory Period* and it lasts approximately 5 ms.

2.2.4. Synaptic Transmission

By using action potentials at their interface, excitable cells are able to communicate with each other using a process called *synaptic transmission*. This process occurs when electrical information contained in an action potential travels to another cell, where it needs to be converted into a different form of signal which can be read by the second cell. They take place in the synapse junction which can be also called neuromuscular junction if the signal exchange is between a (presynaptic) neuron and a myocyte.

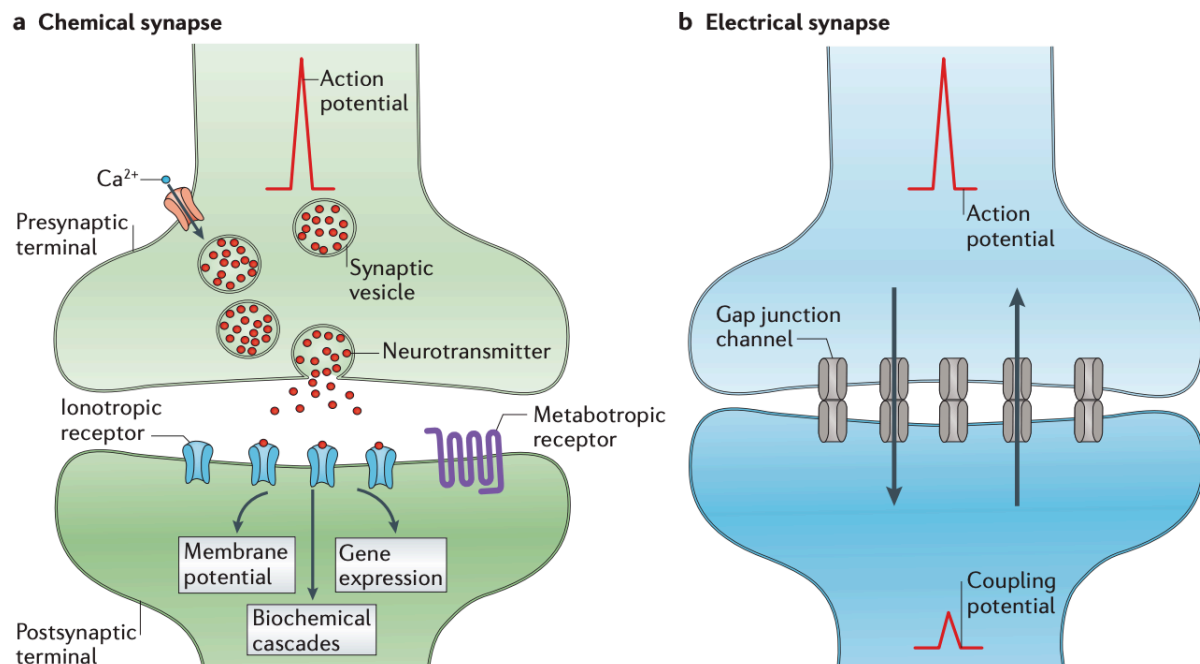


Figure 2.8: Synaptic transmission methods: (a) Chemical synapse; (b) Electrical synapse⁴¹

Depending on their mechanism of operation, they can be divided into (a) chemical synapse and (b) electrical synapse as illustrated in **Figure 2.8**. In both modalities, the process takes place from the presynaptic terminal of one cell and ends in the postsynaptic terminal of the second cell⁴²⁻⁴⁴. Usually, chemical, and electrical synapses coexist.

2.2.5. Diseases Associated with Defects of Tissue Excitability

The proper function of cells excitability is vital in order to maintain normal electrophysiological activity in the body. Any impairments of neurons, myocytes or endocrine cells can lead to a number of degenerative diseases which inhibit the quality of life as well as life expectancy.

Neurodegenerative diseases such as Parkinson's (PD), Alzheimer's (AD) diseases, Amyotrophic Lateral Sclerosis (ALS), originate from either neuron loss or defective neural activity of specific clusters of neurons. These diseases are directly associated with necrosis and deficiencies of astrocytes, which are in charge of regulating the ionic concentration inside and outside neurons and cells, and ultimately determining the correct electrochemical activity (action potential and synapse) of excitable cells and the central nervous system. Parkinson's disease affects the regions of the brain called basal ganglia and substantia nigra. In these regions, the neurotransmitter dopamine is being produced. In individuals with PD, neurons within the substantia nigra necrotise, thus inhibiting the production of dopamine, causing tremors, bradykinesia, and ultimately death. In the case of AD, the morphology of neurons is changed by the abnormal accumulation of a protein called the amyloid precursor protein, creating amyloid plaques and disrupting normal neuron function. AD affects the parts of the brain involved with memory, language, and behaviour, such as the entorhinal cortex, the hippocampus, and the cerebral cortex, affecting cognitive and memory abilities. ALS primarily affects motor neurons which control voluntary muscle movement. Motor neurons progressively die and do not regenerate, making it impossible for normal neuron function. A person with ALS experiences weakening of the muscles which leads to total paralysis and death⁴⁵⁻⁴⁷.

Myocyte degeneration can lead to a number of myopathies. These diseases can either be directly associated with neurons (neuromuscular) or can be of musculoskeletal nature. For example, cardiopathies occur when cardiomyocytes degenerate and are caused by the ineffectiveness or dysfunction of sodium cells in the membrane. An example is cardiac arrhythmia, which originates from action potential time variations which cause irregular cardiac contractions. In this case, the heart can either beat too slow (bradycardia) or too fast (tachycardia), creating unstable blood pressure and ultimately leading to stroke, heart failure, or cardiac arrest, causing loss of consciousness, and in some instances, death⁴⁸.

2.3. ELECTROSTIMULATION OF EXCITABLE CELLS FOR CLINICAL TREATMENTS

Electrostimulation therapies have been extensively researched and implemented against excitable tissue degeneration disorders. Due to their ability to effectively regulate electrical activity, there has been ongoing research focused on how to make them as effective as possible. Unfortunately, at the moment, almost all of them require invasive surgery, which in itself carries a lot of risks. Even though there is no cure for several of these diseases, artificial excitability offers improvement of symptoms, pain relief and increased mobility. First of all, it is critical to establish the mechanisms behind artificial cell excitability.

2.3.1. Mechanism of Artificial Excitable Cell Stimulation

In order to produce the required action potentials that normally are produced by the cells themselves, an external voltage potential is applied which stimulates the voltage-gated ion channels. This can be achieved by attaching an external electrode to the cell membrane. The first model of cell membranes was first developed by Alan Hodgkin and Andrew Huxley in 1952⁴⁹. The model uses a set of differential equations that mimic neuronal and myocyte electrical behaviour and explains the mechanisms of ion migration that occur during action potentials, as illustrated in **Figure 2.9a**.

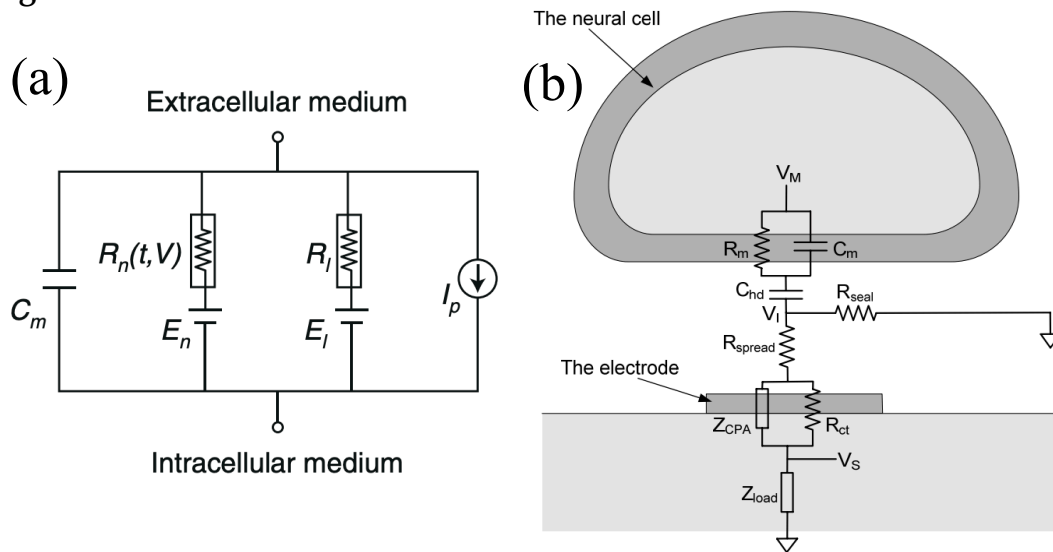


Figure 2.9: (a) Hodgkin-Huxley Membrane Potential RC Equivalent Circuit⁴⁹, where C_m is the lipid bilayer of the cell membrane, R_n are voltage-gated ion channels, R_l are leakage ion channels, E_n and E_l are the ion gradients in charge of ion gradient and ion migration, and I_p are ion pumps which transfer the ions between membrane sides; (b) Point-contact Cell-electrode electrical model, where V_M is the intracellular potential, V_S is the sensed potential, R_m and C_m are the membrane's resistance and capacitance respectively, C_{hd} is the membrane-electrolyte capacitance, R_{seal} is the sealing resistance (between gap junction and electrolyte), R_{spread} is the spreading resistance, R_{ct} is the charge transfer resistance, Z_{CPA} is the constant phase angle impedance and Z_{load} is the load impedance⁵⁰.

A more simplified model of the cell membrane using passive components is shown in **Figure 2.9b**, where the interface with the electrode is also modelled. The electrical interaction between the components provides faradaic and capacitive charge transfer mechanisms that occur when the cell and the electrode, which are in contact, become electrically stimulated. The nature of the charge interactions depends on the material of the metal electrode.

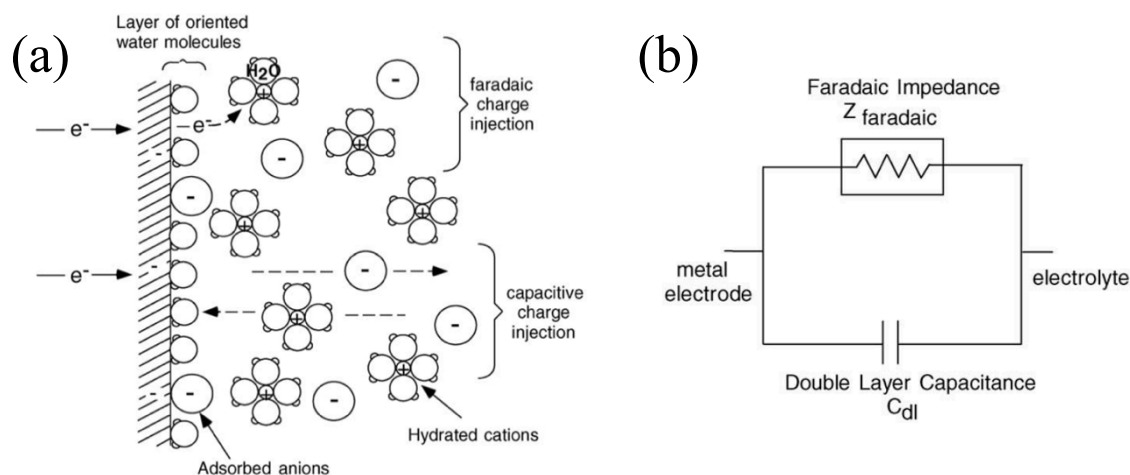


Figure 2.10: Faradaic and capacitive charge interactions; (b) Electrical circuit model mechanisms of charge interactions at the interface²⁷

As illustrated in **Figure 2.10a** (top), during the **faradaic process**, charge injection is achieved when the electrons are transferred during the redox (oxidation-reduction) reaction. Reduction requires the addition of an electron, thus is achieved with a negative electrode, while oxidation which requires the removal of an electrode occurs when the electrode is positive. This reaction is non-reversible. During the **capacitive process**, **Figure 2.10a** (bottom), if the electrode is charged negatively, positive cations from within the solution are attracted to it and negative anions are repelled. If the electrode is charged positively, the opposite effect takes place. If the charge created by is not big enough for electron transfer, charge redistribution will occur. This process is represented by a double-layer capacitor C_{dl} , where the said charge distribution causes charging and discharging of the capacitor at the interface between the electrode and the electrolyte⁵⁰.

2.4. ESTABLISHED CLINICAL TREATMENTS USING WIRED ELECTROSTIMULATION

Modern medicine has implemented a variety of electrostimulation treatments to tackle the effects of cell degeneration. Namely, for cardiac arrhythmias caused by cardiomyocyte dysfunction, about 3 million artificial cardiac pacemakers are implanted each year that regulate heart contractions (**Figure 2.11a**)⁵¹. Moreover, the debilitating effects of Parkinson's disease, epilepsy and stroke are being alleviated by Functional Electrical Stimulation (FES) and Deep Brain Stimulation (DBS) (**Figure 2.11b** and **f**)^{52,53}, by improving mobility, which would otherwise be completely lost. Cochlear and retina implants are also being used to restore hearing and sight, problems caused by sensory neuron degeneration (**Figure 2.11c** and **d**)⁵⁴. Finally, other bodily function associated with the bladder, bowel, or pelvic floor are treated by electrostimulation of the sacral nerve. Problems with this nerve can be hereditary, or they can be due to nerve damage, ultimately causing nerve malfunction (**Figure 2.11e**)⁵¹.

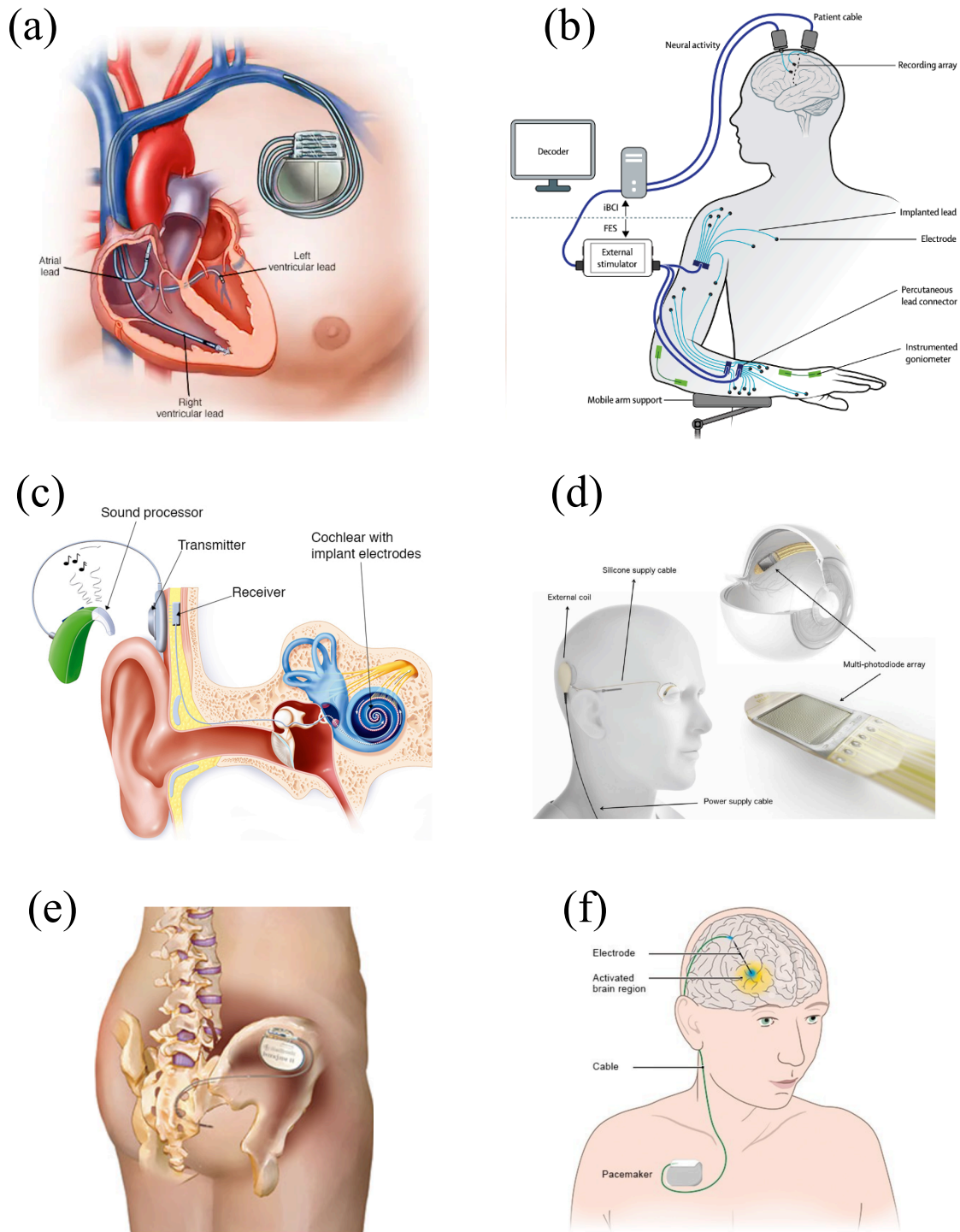


Figure 2.11: Implantable medical devices for electrostimulation: (a) Artificial cardiac pacemaker⁵¹; (b) functional electrical stimulation (FES)⁵² to externally translate neural activity into electrical signals; (c) Cochlear implants which stimulate the nerve fibres of the inner ear using signals from the sound processor; (d) Retina implant Alpha AMS System⁵⁴; (e) Medtronic InterStim[®] system for neurostimulation of the sacral nerve, in charge of bodily functions of bladder, bowel and pelvic floor⁵¹; (f) Deep brain stimulation (DBS) for therapies of diseases associated with neuron degeneration⁵⁵

2.4.1. Limitations of Clinical Treatments Using Wired Electrostimulation

Despite their high efficacy, these devices are often inhibited by secondary, yet crucial, drawbacks. These include complications surfacing from their need of an external power source (e.g., battery) which would require recharging after a given period of time, as well as wiring which could increase the risk of infection and inflammation. Furthermore, these devices tend to excite not only the specific region they are placed in, but also surrounding excitable tissue. This can have adverse side effects to the bodily functions and central nervous system. Finally, these devices require invasive procedures in order to be installed. This suggests a direct risk of surgery complications which can lead to bacterial infections, bleeding, breathing and heart problems, seizures, etc. These facts emphasise the need for devices that can be as effective, but via non-invasive means which can be controlled remotely^{56,57}.

2.5. WIRELESS TISSUE ELECTROSTIMULATION

Over the last three decades, non-invasive electrical stimulation of tissues for biomedical applications has been an area of great interest in wireless therapeutics. The non-invasiveness of these techniques has attracted the attention of researchers and has led to the development of systems which convert stimuli such as optical energy, ultrasounds and magnetic fields into electrical signals.

2.5.1. Wireless Optical Stimulation

Wireless Optical Stimulation is the exploitation of light in order to wirelessly electrostimulate tissues. One of the most notable area of optical stimulation is optogenetics. Optogenetic stimulation, allows for genetically-engineered ion channels, pumps and other proteins to be activated using optical modulation. The selected cells are artificially coupled with microbial photoreceptors. This allows for fast, precise and cell-specific optical control of electrochemical signalling in otherwise non-photosensitive cells. On the other hand, these devices are hindered by low depth of penetration, as well as the required high intensity, which can cause tissue damage due to photothermal effects. Even though this method is still in its early infancy and has not been applied in humans with complete effectiveness, scientists have been able to control the behaviour of animals⁵⁸. Also, there have been substantial progress in some clinical cases in the form of partial restoration of vision of blind patients⁵⁹. The process of gene modification is illustrated in **Figure 2.12**⁶⁰.

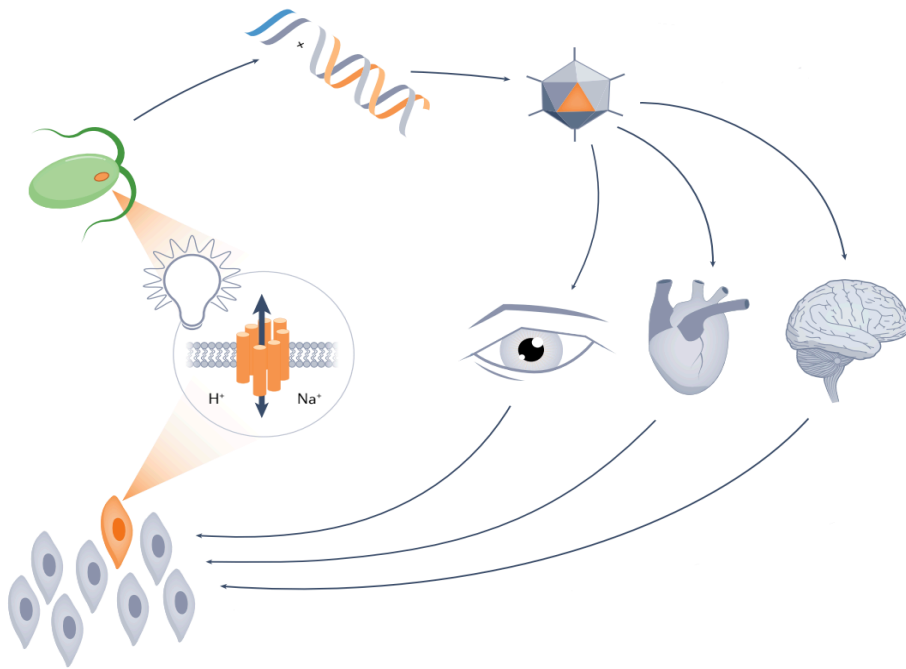


Figure 2.12: Optogenetics mechanism: Genetic modification of tissue of interest by implanting cloned microbial photoreceptors into bacteria and introduced to the target via injection. The specified cells are now photosensitive and can be controlled using light⁶⁰

Furthermore, non-genetic *optically-controlled implantable devices* are increasingly being investigated and developed for their use in neural and excitable tissue disorders. These light-powered devices are capable of delivering electrical stimulation (photovoltaic effect) or thermal stimulation (photothermal effect). Particularly, silicon-based, gold-based and organic semiconductors devices have shown increasing interest and progress. The photovoltaic effect originates from the generation of voltage by illumination (photovoltage). Depending on the emission of light and material characteristics, these voltages can induce photocapacitive or photoelectrochemical actuation, and can have different charge interactions in the interface, which create a transient of the concentrations of ions around the membrane. In contrast, during the photothermal effect, heat is generated locally in the material by the concentrated photon energy. The temperature fluctuations can excite tissues by temperature-induced currents. Silicon-based devices can be used in many different biological applications due to their biocompatibility and natural abundance. They have high tunability and can effectively absorb light over a broad spectrum. They can easily be fabricated into different nanodevices and have been used in both neurostimulation and excitable tissue excitation⁶¹. In **Figure 2.13a**, neural activity was recorded after a nanopatterned Si mesh film was placed on the brain of a live mouse and visible light was emitted on the film⁶². Secondly, gold nanostructures are also vastly investigated due to their enhanced photothermal properties and high biocompatibility⁶². When light is projected on the Au nanostructured devices, because of its high thermal efficiency, depolarization can occur, and action potentials can be generated by the induced temperature increase

and the concomitant change of membrane capacitance. **Figure 2.13b** illustrates gold-covered titania nanowire arrays used as artificial photoreceptors on the retina of a blind mouse, used for vision restoration⁶³. Lastly, organic semiconductor devices are being researched in biomedicine, also due to their biocompatibility as well as photostability. They display exceptional optoelectronic properties and are able to generate photocurrent for neuron or tissue excitation. When light is emitted onto a semiconductor, instead of free electron-hole pairs, a generation of excitons (mobile excited state) is observed. The generated excitons are confined into a few cubic nanometres, and a large eV Coulombic barrier is induced. The excitons then disperse within the organic semiconductor until they arrive at an electrode. An efficient induction of photocurrent is directly associated with a heterojunction between a material which donates electrons and one which accepts electrons. **Figure 2.13c** illustrates a single-component organic film of poly(3-hexylthiophene) (P3HT) used for light sensitivity restoration in the retina of a rat⁶⁴⁻⁶⁶.

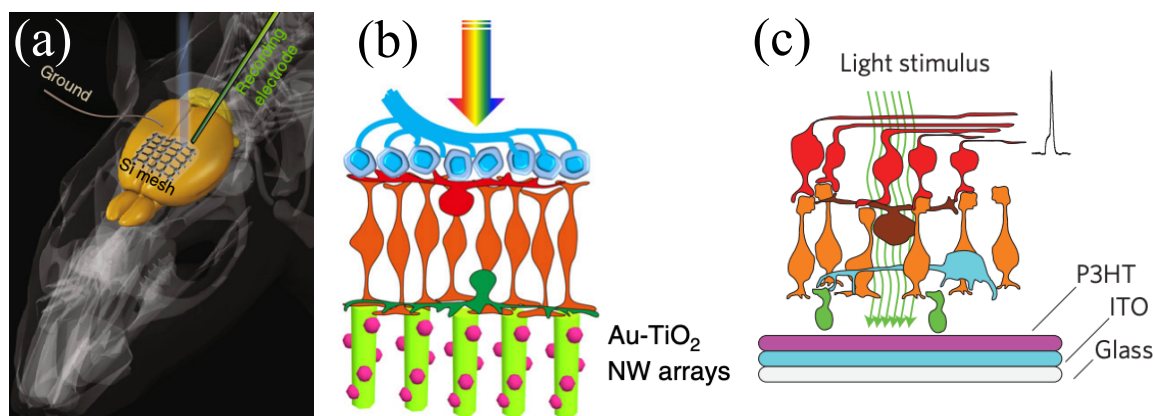


Figure 2.13: Optically-controlled implantable devices for electrostimulation: (a) Photostimulation of mouse brain using an implanted Si mesh⁶²; (b) Illustration of a retina with degenerated photoreceptors, coupled with Au/TiO₂ nanowire (NW) arrays acting as artificial photoreceptors. A healthy retina has normal photoreceptors where the NWs are shown⁶³; (c) Illustration of a retina with degenerated photoreceptors, coupled with P3H organic semiconductor device for photosensitivity restoration⁶⁴.

2.5.2. Wireless Magnetic Stimulation

Wireless magnetic stimulation is another method of externally stimulating tissues, but in this case the stimulus is in the form of applied magnetic field. The lack of need for highly invasive surgery has made this technique highly desirable in the field of biomedicine. An example for electrostimulating the brain in a wireless, non-invasive manner, is transcranial magnetic stimulation (TMS; **Figure 2.13**)^{67,68}. TMS involves a very powerful (1.5 – 3 T), yet very short (1 – 30 Hz) pulse of magnetic field generated by bursts of high current through a magnetic coil, which is placed near the scalp. With the principles of electromagnetic induction, electric pulses are generated, depolarizing the membrane potential and causing action potentials. TMS has been mainly used to treat neurological problems as well as mental health problems. Even though it has been used as a powerful tool to help with the study of the brain, it suffers from poor spatial resolution and low depth of stimulation^{69,70}.

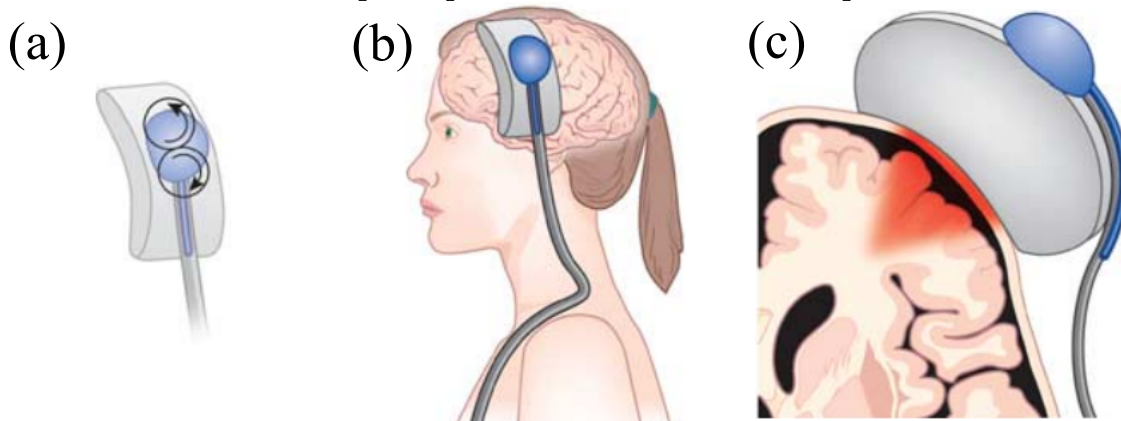


Figure 2.14: Transcranial magnetic stimulation (TMS)⁷¹: (a) Magnetic coil that produces magnetic field showing the direction of current; (b) Illustration of placement of coils on the scalp; (c) Illustration of limitation of depth of effectiveness of TMS.

2.5.3. Wireless Ultrasound Stimulation

Recent research has shown great promise in the harnessing of focused ultrasound (FUS) waves to achieve wireless brain stimulation⁷². The principle of FUS relies on the transmission of a low power pulse of acoustic energy with high spatial resolution and depth control. The pulse travels through the skull to a targeted, specific region of the brain (illustrated in **Figure 2.15**) and has been shown that this non-invasive technique can even target specific neurons⁷³. Due to the fact that this technology is relatively in its infancy, the mechanism of operation and electrophysiological effects are not yet known. However, it has been theorised that the localised acoustic energy exerts pressure around the cell and membrane, causing mechanical deformation, and consequently the activation of mechanically-gated ion channels. This causes the generation of action potentials. Currently, the safety and region of application of FUS are still being investigated⁷⁴⁻⁷⁷.

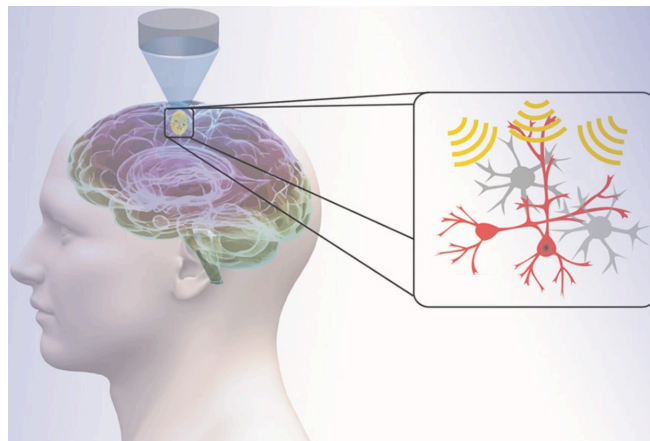


Figure 2.15: Transcranial Focused Ultrasound (tFUS) for wireless neuromodulation⁷⁸

2.5.4. Limitations of Current Wireless Electrostimulation Techniques

Even though they are highly effective, current wireless electrostimulation techniques are inhibited by high power consumption and more importantly, lack of spatial selectivity. This means that in the case of tissue stimulation for example, surrounding tissue might be unwillingly stimulated causing muscle contractions and potentially more serious side effects. Ongoing research aims to minimize this effect by incorporating nanostructures to improve cell selectivity and wireless controllability down to a nanoscale spatial resolution⁷⁹⁻⁸¹. With the use of magnetolectric materials, different wireless procedures such as brain stimulation, drug delivery, and lastly cell and tissue electrostimulation have been made possible. Additionally, these materials improve overall system efficiency when compared to other techniques, as they have higher magnetic field penetration and require much lower magnetic field intensities. Wireless electrostimulation of excitable cells using magnetolectric materials for biomedical applications are elaborated in **Chapter 1**.

2.6. REFERENCES

1. Galvani, L. De viribus electricitatis in motu musculari. *Bononiae: Ex Typographia Instituti Scientiarium* (1791).
2. Volta, A. Untersuchungen über den Galvanismus. **118**, 1796–1800 (1900).
3. Zhang, X. *et al.* Electroactive electrospun nanofibers for tissue engineering. *Nano Today* **39**, 101196 (2021).
4. Hendry, B. *Membrane Physiology and Cell Excitation*. vol. 3 (Springer US, 1981).
5. Lara-González, E., Padilla-Orozco, M., Fuentes-Serrano, A., Bargas, J. & Duhne, M. Translational neuronal ensembles: Neuronal microcircuits in psychology, physiology, pharmacology and pathology. *Front Syst Neurosci* **16**, 979680 (2022).
6. Frank, J. A., Antonini, M.-J. & Anikeeva, P. Next-generation interfaces for studying neural function. *Nat Biotechnol* **37**, 1013–1023 (2019).
7. Holt, C. E., Martin, K. C. & Schuman, E. M. Local translation in neurons: visualization and function. *Nat Struct Mol Biol* **26**, 557–566 (2019).
8. Furness, J. B. Types of neurons in the enteric nervous system. *J Auton Nerv Syst* **81**, 87–96 (2000).
9. Abraira, V. E. & Ginty, D. D. The Sensory Neurons of Touch. *Neuron* **79**, 618–639 (2013).
10. Roper, S. D. Introduction to signal processing in peripheral sensory organs. *Semin Cell Dev Biol* **24**, 1–2 (2013).
11. Stangor, C. & Walinga, J. The Neuron Is the Building Block of the Nervous System. in *Introduction to Psychology* vol. 4 (BCcampus, 2014).
12. Kim, Y., Lindberg, E., Bleck, C. K. E. & Glancy, B. Endothelial cell nanotube insertions into cardiac and skeletal myocytes during coordinated tissue development. *Cardiovasc Res* **116**, 260–261 (2020).
13. Chen, J., Liang, H., Gao, A. & Li, Q. Generation of Skeletal Myocytes from Embryonic Stem Cells Through Nuclear Receptor Signaling. in *NR* (ed. Badr, M. Z.) vol. 1966 247–252 (Humana New York, 2019).
14. Brazhe, N. A., Nikelshparg, E. I., Prats, C., Dela, F. & Sosnovtseva, O. Raman probing of lipids, proteins, and mitochondria in skeletal myocytes: a case study on obesity. *J Raman Spectrosc* **48**, 1158–1165 (2017).
15. Henry, R., Ciaraldi, T. & Chaudhary, S. Human Skeletal Myocytes. *Cell Biology* (Elsevier, 2006) p. 121-125.
16. Severs, N. J. Functional Morphology of the Cardiac Myocyte. in *Muscle and Exercise Physiology* (Elsevier, 2019) p. 459–466.
17. Ko, C. Y., Smith, C. E. R. & Grandi, E. Calcium-Dependent Signaling in Cardiac Myocytes. in *Cardiovascular Signaling in Health and Disease* (Springer International Publishing, 2022) p. 3–37.
18. Ai, X., Yan, J. & Bare, D. J. Stress Kinase Signaling in Cardiac Myocytes. in *Cardiovascular Signaling in Health and Disease* (Springer, 2022) p. 67–110.

19. Rasmussen, L. M., Andresen, J. L. & Ledet, T. Vascular Smooth Muscle Cells. in *Clinically Applied Microcirculation Research* (Routledge, 2019) p. 467–480.
20. Bourke, J. *et al.* Smooth Muscle Cells. in *Encyclopedia of Respiratory Medicine* (Elsevier, 2022) p. 37–51.
21. Rehfeld, A., Nylander, M. & Karnov, K. Muscle Tissue. in *Compendium of Histology* (Springer, 2017) p. 217–245.
22. Bakhti, M., Böttcher, A. & Lickert, H. Modelling the endocrine pancreas in health and disease. *Nat Rev Endocrinol* **15**, 155–171 (2019).
23. Saper, C. B. & Lowell, B. B. The hypothalamus. *Curr Biol* **24**, R1111–R1116 (2014).
24. de Vos, A. *et al.* Human and rat beta cells differ in glucose transporter but not in glucokinase gene expression. *J Clin. Investig* **96**, 2489–2495 (1995).
25. Boland, B. B., Rhodes, C. J. & Grimsby, J. S. The dynamic plasticity of insulin production in β -cells. *Mol Metab* **6**, 958–973 (2017).
26. Ashcroft, F. M. & Rosman, P. ATP-sensitive K⁺ channels: a link between B-cell metabolism and insulin secretion. *Biochem Soc Trans* **18**, 109–111 (1990).
27. Merrill, D. R., Bikson, M. & Jefferys, J. G. R. Electrical stimulation of excitable tissue: design of efficacious and safe protocols. *J Neurosci Methods* **141**, 171–198 (2005).
28. Moldovan, A.-S. *et al.* The treatment of Parkinson's disease with deep brain stimulation: current issues. *Neural Regen Res* **10**, 1018 (2015).
29. Biga, L. M., Bronson, S., Dawson, S., Harwell, A., Hopkins, R., Kaufmann, J., LeMaster, M., Matern, P., Morrison-Graham, K., Oja, K., Quick, D., & Runyeon, J. (n.d.). 3.1 The Cell Membrane – Anatomy & Physiology. 3.1 the Cell Membrane – Anatomy & Physiology. <https://open.oregonstate.edu/aandp/chapter/3-1-the-cell-membrane/> (Accessed May 20 , 2023)
30. Shad, K. F., Salman, S., Afridi, S., Tariq, M. & Asghar, S. Introductory Chapter: Ion Channels. in *Ion Channels in Health and Sickness* (InTech, 2018) p. 3-10.
31. Luan, S., Williams, I., Nikolic, K. & Constandinou, T. G. Neuromodulation: present and emerging methods. *Front Neuroeng* **7**, 27 (2014).
32. An, H. Ion Channels and Bone Homeostasis Imbalance. *Biomed J Sci Tech Res* **16**, 12088-12093 (2019).
33. Gated Ion Channels - Biosignalling - MCAT Content. (2020, March 24). Jack Westin. <https://jackwestin.com/resources/mcat-content/biosignalling/gated-ion-channels> (Accessed May 20 , 2023)
34. Terlau, H. & Stühmer, W. Structure and Function of Voltage-Gated Ion Channels. *Naturwissenschaften* **85**, 437–444 (1998).
35. Huang, Y., Fliedert, R., Guse, A. H., Lü, W. & Du, J. A structural overview of the ion channels of the TRPM family. *Cell Calcium* **85**, 102111 (2020).
36. Bates, E. Ion Channels in Development and Cancer. *Annu Rev Cell Dev Biol* **31**, 231–247 (2015).

37. Bartos, D. C., Grandi, E. & Ripplinger, C. M. Ion Channels in the Heart. in *Comprehensive Physiology* (Wiley, 2015) p. 1423–1464.
38. Rettinger, J., Schwarz, S. & Schwarz, W. *Electrophysiology: Basics, Modern Approaches and Applications. Electrophysiology* (Springer Nature, 2016).
39. Bu, G., Adams, H., Berbari, E. J. & Rubart, M. Uniform Action Potential Repolarization within the Sarcolemma of In Situ Ventricular Cardiomyocytes. *Biophys J* **96**, 2532–2546 (2009).
40. Huxley, A. F. & Stämpfli, R. Direct determination of membrane resting potential and action potential in single myelinated nerve fibres. *J Physiol* **112**, 476–495 (1951).
41. Pereda, A. E. Electrical synapses and their functional interactions with chemical synapses. *Nat Rev Neurosci* **15**, 250–263 (2014).
42. Li, X., Hémond, G., Godin, A. G. & Doyon, N. Computational modeling of trans-synaptic nanocolumns, a modulator of synaptic transmission. *Front Comput Neurosci* **16**, 969119 (2022).
43. Atlas, D. Revisiting the molecular basis of synaptic transmission. *Prog Neurobiol* **216**, 102312 (2022).
44. Wang, B. & Dudko, O. K. A theory of synaptic transmission. *eLife* **10**, e7358 (2021).
45. Phatnani, H. & Maniatis, T. Astrocytes in Neurodegenerative Disease: Table 1. *Cold Spring Harb Perspect Biol* **7**, 20628 (2015).
46. Jellinger, K. A. Basic mechanisms of neurodegeneration: a critical update. *J Cell Mol Med* **14**, 457–487 (2010).
47. Gorman, A. M. Neuronal cell death in neurodegenerative diseases: recurring themes around protein handling. *J Cell Mol Med* **12**, 2263–2280 (2008).
48. Braunwald, E. Cardiomyopathies. *Circ Res* **121**, 711–721 (2017).
49. Hodgkin, A. L. & Huxley, A. F. A quantitative description of membrane current and its application to conduction and excitation in nerve. *J Physiol* **117**, 500–544 (1952).
50. Joye, N., Schmid, A. & Leblebici, Y. Electrical modeling of the cell–electrode interface for recording neural activity from high-density microelectrode arrays. *Neurocomputing* **73**, 250–259 (2009).
51. Zheng, G., Shankaran, R., Orgun, M. A., Qiao, L. & Saleem, K. Ideas and Challenges for Securing Wireless Implantable Medical Devices: A Review. *IEEE Sens J* **17**, 562–576 (2017).
52. Ajiboye, A. B. *et al.* Restoration of reaching and grasping movements through brain-controlled muscle stimulation in a person with tetraplegia: a proof-of-concept demonstration. *Lancet* **389**, 1821–1830 (2017).
53. Parkinson’s disease: Deep brain stimulation. *Institute for Quality and Efficiency in Health Care (IQWiG, Germany)*.
<https://www.informedhealth.org/parkinsons-disease-deep-brain-stimulation.html>
(Accessed May 20, 2023)

54. Bloch, E., Luo, Y. & da Cruz, L. Advances in retinal prosthesis systems. *Ther Adv Ophthalmol* **11**, (2019).
56. Nardone, R. *et al.* Invasive and non-invasive brain stimulation for treatment of neuropathic pain in patients with spinal cord injury: A review. *J Spinal Cord Med* **37**, 19–31 (2014).
57. Dolbow, D. R., Gorgey, A. S., Sutor, T. W., Bochkezanian, V. & Musselman, K. Invasive and Non-Invasive Approaches of Electrical Stimulation to Improve Physical Functioning after Spinal Cord Injury. *J Clin Med* **10**, 5356 (2021).
58. Towne, C. & Thompson, K. R. Overview on Research and Clinical Applications of Optogenetics. *Curr Protoc Pharmacol* **75**, 11.19 (2016).
59. Sahel, J.-A. *et al.* Partial recovery of visual function in a blind patient after optogenetic therapy. *Nat Med* **27**, 1223–1229 (2021).
60. Emiliani, V. *et al.* Optogenetics for light control of biological systems. *Nat Rev Methods Primers* **2**, 55 (2022).
61. Parameswaran, R. *et al.* Photoelectrochemical modulation of neuronal activity with free-standing coaxial silicon nanowires. *Nat Nanotechnol* **13**, 260–266 (2018).
62. Jiang, Y. *et al.* Nongenetic optical neuromodulation with silicon-based materials. *Nat Protoc* **14**, 1339–1376 (2019).
63. Tang, J. *et al.* Nanowire arrays restore vision in blind mice. *Nat Commun* **9**, 786 (2018).
64. Ghezzi, D. *et al.* A polymer optoelectronic interface restores light sensitivity in blind rat retinas. *Nat Photonics* **7**, 400–406 (2013).
65. Janssen, R. A. J. & Nelson, J. Factors Limiting Device Efficiency in Organic Photovoltaics. *Adv Mater* **25**, 1847–1858 (2013).
66. Bareket-Keren, L. & Hanein, Y. Novel interfaces for light directed neuronal stimulation: advances and challenges. *Int J Nanomedicine* **9**, 65–83 (2014).
67. Hallett, M. Transcranial magnetic stimulation and the human brain. *Nature* **406**, 147–150 (2000).
68. Walsh, V. & Cowey, A. Transcranial magnetic stimulation and cognitive neuroscience. *Nat Rev Neurosci* **1**, 73–80 (2000).
69. Groppa, S. *et al.* A practical guide to diagnostic transcranial magnetic stimulation: Report of an IFCN committee. *Clin Neurophysiol* **123**, 858–882 (2012).
70. George, M. S. & Post, R. M. Daily Left Prefrontal Repetitive Transcranial Magnetic Stimulation for Acute Treatment of Medication-Resistant Depression. *Am J Psychiatry* **168**, 356–364 (2011).
71. George, M. S. & Aston-Jones, G. Noninvasive techniques for probing neurocircuitry and treating illness: vagus nerve stimulation (VNS), transcranial magnetic stimulation (TMS) and transcranial direct current stimulation (tDCS). *ACNP* **35**, 301–316 (2010).
72. Lee, J. *et al.* A MEMS ultrasound stimulation system for modulation of neural circuits with high spatial resolution in vitro. *Microsyst Nanoeng* **5**, 28 (2019).

73. Yu, K., Niu, X., Krook-Magnuson, E. & He, B. Intrinsic functional neuron-type selectivity of transcranial focused ultrasound neuromodulation. *Nat Commun* **12**, 2519 (2021).
74. Lee, W. *et al.* Image-Guided Transcranial Focused Ultrasound Stimulates Human Primary Somatosensory Cortex. *Sci Rep* **5**, 8743 (2015).
75. Baek, H., Pahk, K. J. & Kim, H. A review of low-intensity focused ultrasound for neuromodulation. *Biomed Eng Lett* **7**, 135–142 (2017).
76. Legon, W. *et al.* Transcranial focused ultrasound modulates the activity of primary somatosensory cortex in humans. *Nat Neurosci* **17**, 322–329 (2014).
77. Kim, H. *et al.* Noninvasive Transcranial Stimulation of Rat Abducens Nerve by Focused Ultrasound. *Ultrasound Med Biol* **38**, 1568–1575 (2012).
78. Vaccar, S. Focused Ultrasound Enables Precise Noninvasive Therapy. *Carnegie Mellon University*
<https://www.cmu.edu/news/stories/archives/2021/may/noninvasive-ultrasound.html> (Accessed May 20, 2023)
79. Hu, J.-M., Chen, L.-Q. & Nan, C.-W. Multiferroic Heterostructures Integrating Ferroelectric and Magnetic Materials. *Adv Mater* **28**, 15–39 (2016).
80. Fiebig, M. Revival of the magnetoelectric effect. *J Phys D Appl Phys* **38**, R123–R152 (2005).
81. Kopyl, S., Surmenev, R., Surmeneva, M., Fetisov, Y. & Kholkin, A. Magnetoelectric effect: principles and applications in biology and medicine—a review. *Mater Today Bio* **12**, 100149 (2021).

3. Experimental Techniques

3.1. FABRICATION

3.1.1. Substrate preparation

In both chapters, prior to starting any fabrication steps, $20 \text{ mm}^2 \times 20 \text{ mm}^2$ pieces were cut from [100]-oriented Si wafers. They were rinsed with ethanol and milli-Q water and blow-dried with N_2 gas. Then, they were treated with O_2 reactive ion etching (RIE) for 5 minutes to remove surface contaminants using a PVA Tepla PS-210 at the cleanroom of the Nanofabrication Facility of the Catalan Institute of Nanoscience and Nanotechnology (ICN2).

3.1.2. Thin Film Deposition

Electron Beam Evaporation Deposition

For the preparation of the samples used in Chapters 4 and 5, metal deposition by electron beam (e-beam) evaporation was carried out at room temperature using an *ATC-8E Orion* of *AJA International Inc* evaporator. The deposition rates used were 0.05 nm/s, 0.1 nm/s and 0.15 nm/s for the deposition of Au, Ti and Al, respectively. The base pressure of main chamber was 1×10^{-8} Torr.

The e-beam depositions were carried out by me, at the cleanroom of the Nanofabrication Facility of the Catalan Institute of Nanoscience and Nanotechnology (ICN2).

Magnetron Sputtering Deposition

In order to deposit the ferromagnetic FeGa layers used in Chapters 4 and 5, magnetron sputtering was used at room temperature. The *ATC Orion 5* from *AJA International* was used to sputter FeGa using a $\text{Fe}_{80}\text{Ga}_{20}$ (at %) target at 100 W at deposition rate of 0.132 nm/s. The pressure of the sputtering chamber was at $\sim 10^{-7}$ Torr, while during sputtering, the pressure was $\sim 3 \times 10^{-3}$ Torr.

The magnetron sputtering deposition was done by Pau Solsona of the Group of Smart Nanoengineered Materials Nanomechanics and Nanomagnetism (GNM3) at the Universitat Autònoma de Barcelona (UAB).

Pulsed Laser Deposition (PLD)

In Chapter 5, the BaTiO_3 layers were deposited using pulsed laser deposition (PLD). The layer was grown using a *Lambda Physic Compex 201 KrF* pulsed excimer laser with a wavelength of 248 nm, fluence 5.4 J/cm^2 and a repetition rate of 2 Hz. A stoichiometric BaTiO_3 ceramic target was ablated with a total of 590 pulses performed at a rate of 0.054 nm/pulse in order to achieve the final thickness of grown BaTiO_3 of 32 nm. The BaTiO_3 layer was deposited at a temperature of $700 \text{ }^\circ\text{C}$ in an O_2 atmosphere pressurised to $p\text{O}_2 = 100 \text{ mTorr}$. After the deposition, it was cooled down in an O_2 saturated atmosphere $p\text{O}_2 = 10^4 \text{ mTorr}$ at a rate of $3 \text{ }^\circ\text{C/min}$.

The pulsed laser deposition was done by José Manuel Caicedo Roque of the Nanomaterials Growth Unit at the Catalan Institute of Nanoscience and Nanotechnology (ICN2).

Hydrothermal Synthesis

In order to grow the ZnO layers of Chapter 4, 50 mL of equimolar aqueous solution of Zinc Oxide Hexafluoride ($\text{Zn}(\text{NO}_3)_2$) and Hexamethylenetetramine (HMTA) (both purchased from *Sigma Aldrich*) was magnetically stirred and then sonicated for 10 minutes.

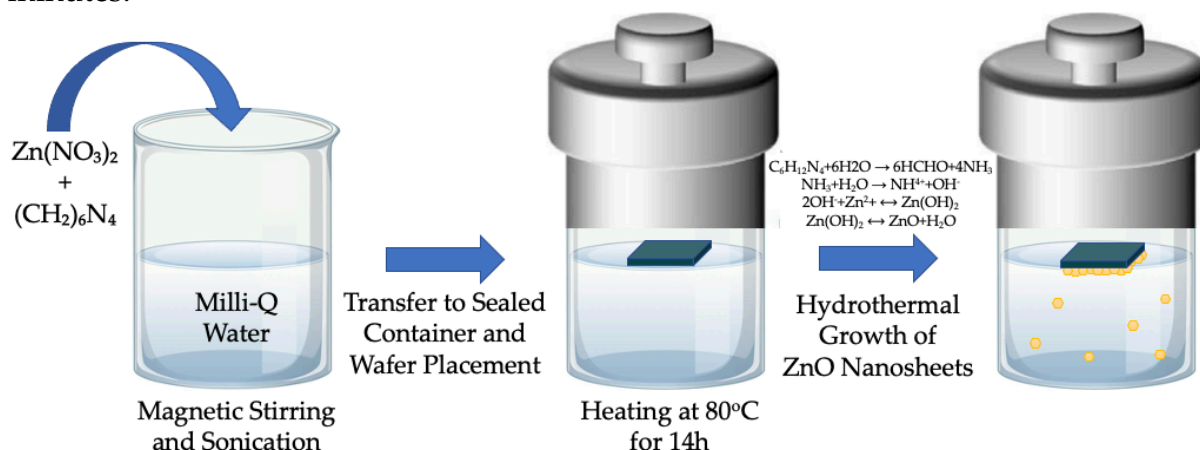


Figure 3.1: Hydrothermal Synthesis of ZnO Growth Steps

A substrate with a Au (50 nm)/Ti (10 nm)/Al (100 nm) seed layer was placed upside down on the surface of the solution, hermetically sealed and placed inside a convection oven at 80 °C for 14 hours. During the synthesis, the $\text{Zn}(\text{NO}_3)_2$ provides Zn^{2+} ions, while the HMTA provides an alkaline environment and OH^- ions¹. The Zn^{2+} ions react with OH^- ions forming zinc hydroxide. The zinc hydroxide then undergoes dehydration and recrystallization to form the ZnO nanostructures on the surface of the sample¹⁻³. The Al layer is dissolved during the reaction and is assimilated into the grown structures, creating Al-doped ZnO nanosheets^{4,5}. The sample was then removed, dipped in ethanol to avoid stiction aggregation of the nanostructures from the surface tension caused by the evaporation of water⁶ of the nanosheets. Finally, the sample was allowed to dry at room temperature.

The hydrothermal synthesis of ZnO nanosheets was done by me, at the laboratory of Magnetic Nanostructures of the Catalan Institute of Nanoscience and Nanotechnology (ICN2).

3.1.3. Polymer Substrate Fabrication

Polydimethylsiloxane (PDMS) Deposition and Curing

PDMS is a soft thermoset polymer used Chapter 4 to create the thin film substrate into which the FeGa/ZnO layers were embedded. The *SYLGARD™ 184 Silicone Elastomer Kit* was selected for the PDMS preparation.

Firstly, the base polymer and the curing agent were mixed at a ratio of 10:1. The mixture was stirred thoroughly and placed in a low vacuum environment for 15 minutes or until all visible bubbles were removed. To achieve the thickness of 50 μm , the mixture was poured onto the sample ($20\text{ mm}^2 \times 20\text{ mm}^2$), and using a spin-coating machine the sample was spun at 1000 rpm for a total of 60 seconds. The sample was then placed in a convection oven at 100 °C for 1 hour, until the PDMS film was cured. Finally, the film was cut to $10 \times 10\text{ mm}^2$ squares and peeled off the wafer using tweezers.

The deposition of PDMS was done by me, at the laboratory of Magnetic Nanostructures at the Catalan Institute of Nanoscience and Nanotechnology (ICN2).

3.1.4. Micropatterning

The structures presented in Chapter 5 were fabricated by micropatterning, which involved several steps.

Electrostatic Colloidal Self-Assembly

The shape of the microdisc structures in Chapter 5, was based on the use of commercial silica microspheres which were used as masks in order to achieve the round form. The surface of the sample was first treated with positively charged polydiallyldimethylammonium chloride (PDDA) diluted to 2%, for 5 minutes. The surface was rinsed with milli-Q water and dried with N_2 gas, leaving it positively charged. Then, negatively charged silica spheres (*Sigma Aldrich*, 5 % w/v, diameter 2 μm) were diluted to 1% w/v in milli-Q water, sonicated for 10 minutes, and placed on the surface for 5 minutes. The surface was rinsed with milli-Q water to remove the surplus of spheres and gently dried using N_2 gas to leave an ordered array of silica microspheres.

Inductively Coupled Plasma - Reactive Ion Etching (ICP-RIE)

To create the microdiscs, we use a *PlasmaPro Cobra 100* from *Oxford Instruments*. By performing Ar RIE (HF 30 W, ICP 1000 W, 5 mTorr, 50 sccm) for 45 minutes, the metallic and BaTiO_3 layers around the base of the microspheres were removed, leaving a microdiscs structure (see **Figure 5.1e** and **f** in Chapter 5). Finally, SF_6 RIE (HF 10 W, ICP 1000 W, 12 mTorr, 20 sccm) was performed for 90 seconds, to isotropically etch the Si of the substrate not protected by the previously patterned discs. This process leads to the suspended microdiscs with a central pillar of Si holding the discs (see **Figure 5.1g** in Chapter 5).

The electrostatic self-assembly was carried out by me at the Institute of Microelectronics of Barcelona (IMB-CNM, CSIC), while the ICP-RIE was done by me at the cleanroom of the Nanofabrication Facility of the Catalan Institute of Nanoscience and Nanotechnology (ICN2).

3.2. CHARACTERISATION

3.2.1. Morphological and Structural

In Chapters 4 and 5, different morphological and structural measurements were performed in order to observe the shape and size of the structures, as well as their composition and crystal structure. This was necessary for guaranteeing the quality and reproducibility of the structures. The morphological and structural characterisations were performed by electron microscopy (scanning and transmission) and x-ray diffraction.

Scanning Electron Microscopy (SEM)

Scanning Electron Microscopy (SEM) was used to perform morphological characterisation of the micro- and nanostructures. The images were obtained using the *Quanta 650 FEG* at 7.5 kV under high vacuum. Energy dispersive X-ray spectroscopy (EDX) mode was also used to determine the composition of the materials in the samples.

The SEM images were taken by me, at the Electron Microscopy Unit of the Catalan Institute of Nanoscience and Nanotechnology (ICN2).

Transmission Electron Microscopy (TEM)

To prepare the cross-section specimens of the samples for the TEM studies, lamellas of the structures were prepared using focused ion beam (FIB) milling using a gallium ion source (*FEI Nanolab Helios 650 - FIB*).

A *TEM/STEM Jeol ARM 200* operated at 80 kV and a *FEI Tecnai G2 F20* with a 200 kV field emission gun (FEG) were utilised for the transmission electron microscopy (TEM) and high-resolution TEM (HR-TEM) measurements.

Electron energy loss spectroscopy (EELS) analysis was carried out in the *TEM/STEM Jeol ARM 200 CF STEM*, which was equipped with a *Jeol Centurio EDXS* system with a 100 mm² SDD detector and a *Gatan Quantum ER Dual Electron Energy Loss Spectroscopy (EELS)* system.

The preparation of the lamellas was carried out by Bojan Ambrožič at the Jožef Stefan Institute (JSI) and Francisco Javier Belarre Triviño of the Electron Microscopy Unit of the Catalan Institute of Nanoscience and Nanotechnology (ICN2). The TEM/STEM experiments were carried out by Goran Dražić at the National Institute of Chemistry in Ljubljana and by Belén Ballesteros Pérez of the Electron Microscopy Unit of the Catalan Institute of Nanoscience and Nanotechnology (ICN2).

X-Ray Diffraction (XRD)

In Chapters 4 and 5, x-ray diffraction (XRD) was used to determine the crystallographic structure and crystallite sizes of the BaTiO₃, ZnO and FeGa layers. A *Malvern PANalytical X'pert Pro MRD* with Cu K α radiation ($\lambda = 1.540 \text{ \AA}$) was used.

The XRD analysis was carried out by Jessica Padilla Pantoja of the X-ray Diffraction Facilities of the Catalan Institute of Nanoscience and Nanotechnology (ICN2) and were analysed by me.

3.2.2. Magnetometry

Vibrating Sample Magnetometer (VSM)

In order to obtain the magnetic behaviour of the samples in Chapters 4 and 5, a *MicroSense (LOT-Quantum Design)* was used. A magnetic field was applied from -20,000 Oe to +20,000 Oe and the voltage induced by the magnetic flux oscillations was measured by pickup coils (Figure 3.2). The produced data give us information about the coercivity, remanence, as well as the saturation magnetization of the structures.

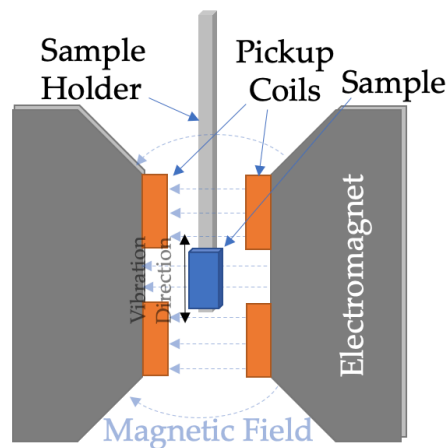


Figure 3.2: Schematic of Operation of the VSM

The VSM measurements were carried out by me with the help of Aliona Nicolenco of the Group of Smart Nanoengineered Materials Nanomechanics and Nanomagnetism (GNM3) of the Universitat Autònoma de Barcelona (UAB) and were analysed by me.

3.2.3. Scanning Probe Microscopy (SPM)

Piezoresponse Force Microscopy (PFM)

In order to evaluate the piezoelectric and ferroelectric properties of the nanostructures in Chapters 4 and 5, atomic force microscopes (AFM) in piezo force microscopy (PFM) mode were used. These high-resolution scanning probe microscopes consist of the stage onto which the sample was placed, a cantilever with a sharp tip which rested on the sample, a laser beam which was directed onto the back of the cantilever, the photodiode and the detector and lock-in amplifier (Figure 3.3: Schematic of the AFM Components⁷⁻⁹)

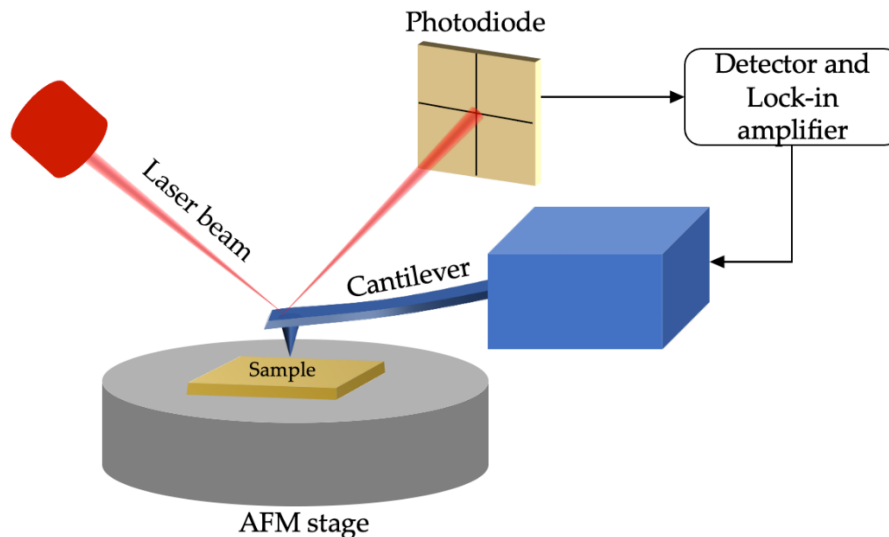


Figure 3.3: Schematic of the AFM Components⁷⁻⁹

Due to the converse piezoelectric effect, deformations (contracting or expanding) on the surface of the piezoelectric (or ferroelectric) materials are observed when a voltage is applied through the tip. In PFM mode, these deformations cause the cantilever to displace, creating changes of the laser beam reflected to the photodiode detector, which converts them into vertical displacements (**Figure 3.4**)^{7,10,11}. Using the PFM mode, the piezoelectric, ferroelectric, and by applying an external magnetic field, the magnetoelectric nature of materials can be assessed.

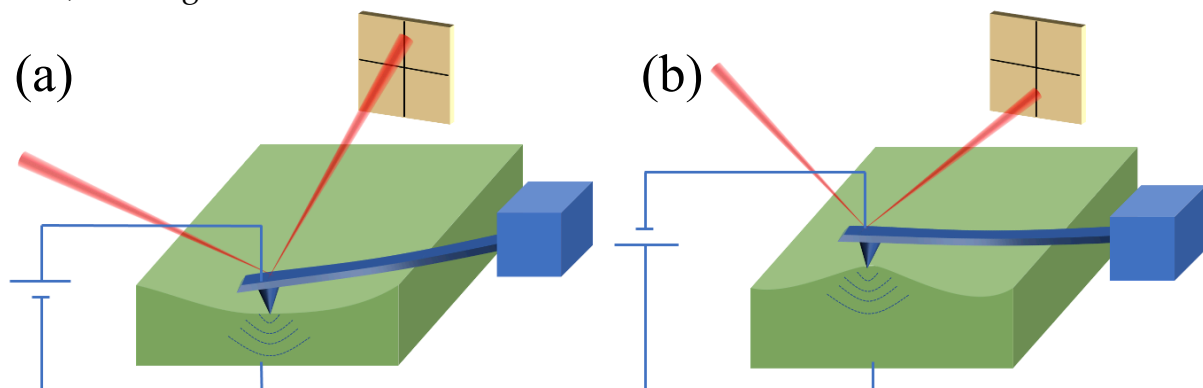


Figure 3.4: Illustration of the operation of the PFM when a voltage is applied between the tip and the sample, (a) contract or (b) expand the sample, depending on the applied voltage⁷

An *Asylum MFP-3D Classic AFM* with a PtIr5-coated tip was used in PFM mode in order to estimate the piezoelectric coefficients of the structures in Chapters 4 and 5. The AFM used a cantilever with a spring constant of $k = 2.8 \text{ Nm}^{-1}$ to apply a bias voltage and then measure the mechanical deformation of the material caused by the converse piezoelectric effect. The error of the piezoelectric coefficients was estimated by carrying out three different measurements at the same location. Additionally, the ferroelectric nature of the BaTiO₃ layer of Chapter 5 was evaluated by poling two concentric squares with opposite polarizations ($\pm 9 \text{ VDC}$). This method involves applying voltage on the surface of the ferroelectric material

through the tip of the PFM, causing the polarization to align along the voltage direction. The two squares are then scanned without bias voltage, providing information about the ferroelectric domains' orientations, namely, coercivity of the material and remanent polarization, which is exhibited by ferroelectric materials. These experiments were carried out by Christina Stefani of the Group of Smart Nanoengineered Materials Nanomechanics and Nanomagnetism (GNM3) of the Universitat Autònoma de Barcelona (UAB).

A *NT-MDT NTEGRA Prima AFM* with a Pt-coated tip and cantilever with a spring constant of $k = 2.8 \text{ Nm}^{-1}$ was used in PFM mode to estimate the local magnetoelectric coupling coefficient in Chapter 5. A bias voltage was applied through the tip onto the surface to extract the piezoresponse amplitude and phase hysteresis loops of the structure while applying different magnetic field values. In magnetoelectric materials, when comparing a hysteresis loop obtained while applying zero magnetic field with a hysteresis loop obtained while applying non-zero magnetic field, a difference in the coercive voltages is observed. By assuming that the coercive voltage differences of each hysteresis loop are due to a generation of an internal electric field, we can estimate the local magnetoelectric coefficient (a_E) by using:

$$a_E = \frac{\Delta E}{\Delta H} \quad (3.1)$$

, where ΔH is the increment of the applied magnetic field which causes the electric field generation and ΔE is the increment of electric field generated by the applied magnetic field. The error of the magnetoelectric coefficients was estimated using five measurements. These experiments were carried out by me with the help of Joaquim Llacer Wintle and Xiangzhong Chen of the Multi-Scale Robotics Lab of ETH Zürich.

3.2.4. Magneto-Mechanical Flexibility Assessment

To study the mechanical flexibility of the thin film structures in Chapter 4 under external magnetic field, a *Dino-Lite AD4113T-I2V* digital microscope camera was used. The software used to capture and analyse the images were *Dino-Lite* and *ImageJ* respectively. In these analyses, the angle of curvature at the tip of a laser-cut cantilever was measured in relation to either the intensity or direction of magnetic field.

Cantilever Laser Cutting

The samples were cut into cantilevers of specified dimensions designed on *Inkscape*, using an *Epilog* Laser cutter.

Magneto-mechanical Responses

The magnetic field used to induce the magneto-mechanical actuation of the cantilevers was generated using a spherical, 12 mm diameter, FeNdB permanent magnet which was approached towards the sample from different directions and

orientations. The applied magnetic field was calibrated using a *Magnet-Physik FH-52* Gaussmeter.

The cantilevers were cut with the help of Pau Güell-Grau, and the magneto-mechanical response experiments were performed by me, again with the help of Pau Güell-Grau at the laboratory of Magnetic Nanostructures of the Catalan Institute of Nanoscience and Nanotechnology (ICN2).

3.2.5. Magnetic Stimulation System

3.2.5.1. Generating ac Magnetic Fields Using the Resonance Technique

An ac magnetic field can be generated when a time-varying current passes through a coil. The intensity, frequency and direction of the generated magnetic field depend on the intensity, frequency, and direction of the applied current. In first approximation, the field produced by a coil is given by:

$$H = \mu_r \cdot n \cdot I \quad (3.2)$$

, where μ_r is the relative permeability of the material inside the core, n is the number of turns of the coil per unit of length, and I is the current intensity.

The current running through the coil can be calculated using Ohm's law of impedance:

$$I = \frac{V}{Z_{coil}} \quad (3.3)$$

, where I , V and Z_{coil} correspond to the current intensity, voltage across and the impedance of the coil respectively. The coil impedance is expressed as the sum of the parasitic Ohmic resistance (R) and the inductive reactance (X_L) of the coil, and can be calculated as:

$$|Z_{coil}| = \sqrt{R^2 + X_L^2} \quad (3.4)$$

Moreover, the inductive reactance of the coil is the product of the inductance value and the operating frequency:

$$X_L = \omega \cdot L_C = 2 \cdot \pi \cdot f \cdot L_C \quad (3.5)$$

, where f is the operating frequency and L_C is the inductance value of the coil in Henrys. Therefore, as the frequency is increased, the inductive reactance increases, increasing the coil total impedance, limiting the current flowing through the coil and, consequently, reducing the magnetic field intensity generated.

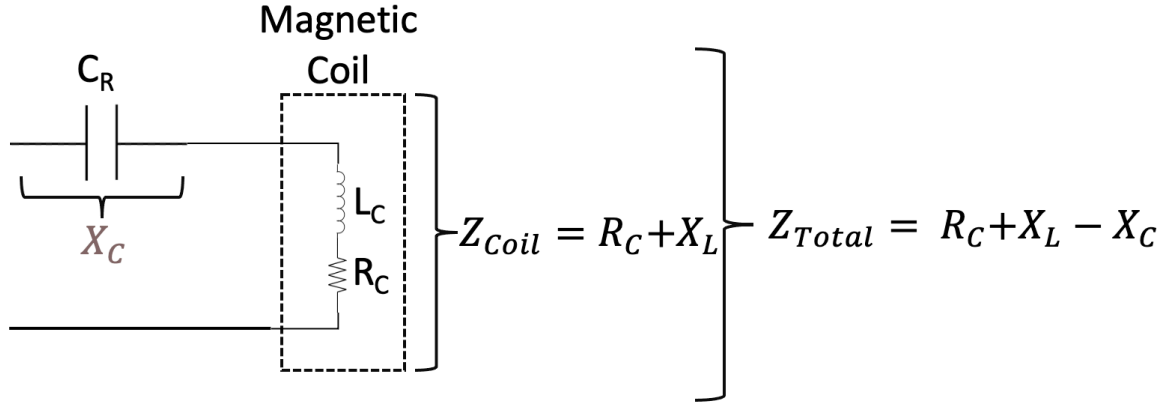


Figure 3.5: Schematic representation of the equivalent circuit of the magnetic coil setup paired with a capacitor in-series.

The optimal impedance value of the coil which would maximise the current flow, would be the one whose total reactance is zero, and only the Ohmic resistance is taken into account. In order to achieve this, a capacitor (C_R) of a specific value is connected in series with the coil (**Figure 3.5**). The value of this capacitor is calculated for a specific operating (resonance) frequency which produces a capacitive reactance equal to the inductive reactance, thus cancelling each other out. This value can be calculated as:

$$X_C = X_L \therefore \frac{1}{2 \cdot \pi \cdot f_r \cdot C_R} = 2\pi f_r L_C \therefore C_R = \frac{1}{(2 \cdot \pi \cdot f_r)^2 \cdot L_C} \quad (3.6)$$

, where X_C is the capacitive reactance, f_r is the resonance frequency and C_R is the capacitor value in Farads used to achieve resonance at the specified frequency. Using this technique, the sum of the reactances at resonance is equal to zero and therefore the total impedance of the system can be expressed as:

$$Z_{Total} = R_C \quad (3.7)$$

3.2.5.2. Magnetic Actuator System

The magnetic actuator system was powered using a *Siglent SDG-1025* signal generator and an *Accel TS200* power supply (**Figure 3.6a**). The magnetic coil was fabricated using a ferrite toroid with a 13 mm gap, which creates a circular magnetic field along the circumference of the loop, reducing the electromagnetic interference (EMI) emitted by the winding. Ferrite was chosen as the material for the core of the coil due to its reduced core losses over different frequencies. The core was wrapped with 65 turns of laminated copper wire (**Figure 3.6b**) which resulted in an inductance of $L_C = 0.671 \text{ mH}$ and an Ohmic resistance of $R_C = 0.03 \Omega$, measured using a multimeter.

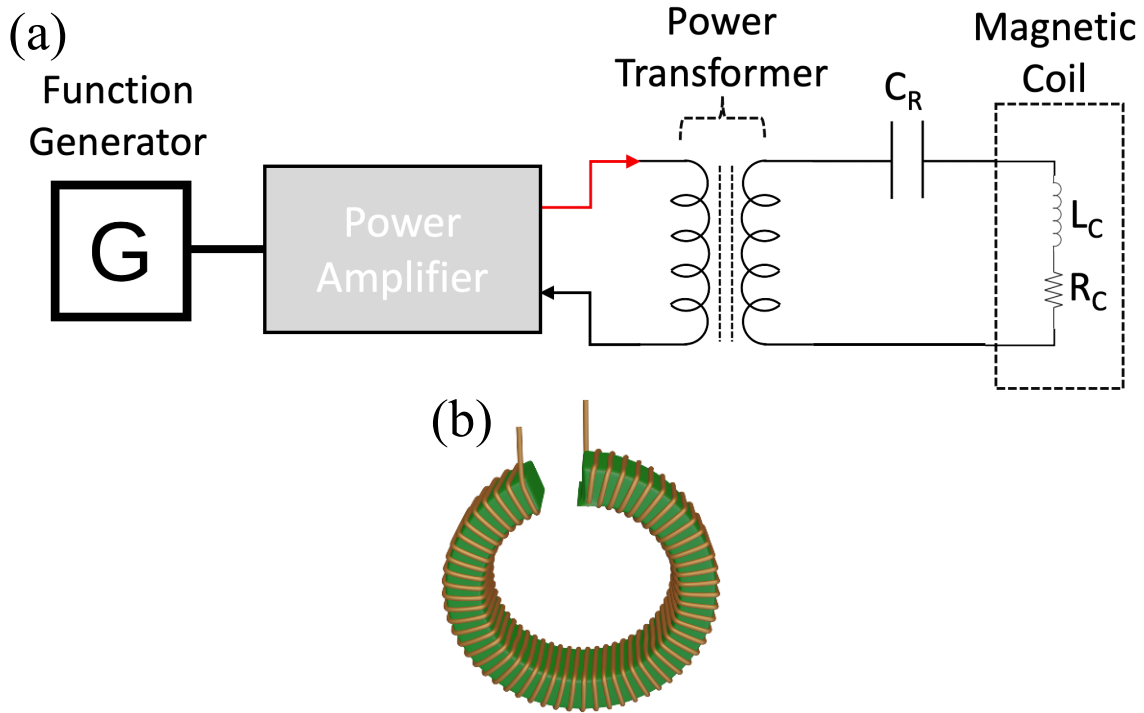


Figure 3.6: (a) Schematic of the magnetic actuator system; (b) Illustration of the magnetic coil.

By using the resonance technique and the appropriate capacitors (**Figure 3.7a**), the setup was able to achieve magnetic field values between 100 to 1000 Oe over frequencies between 1 Hz to 110 kHz in the gap of the core.

Measuring the generated magnetic fields at high frequencies can be quite complex. In our case, the magnetic field generated by our set up was measured using a pickup coil (**Figure 3.7b**) designed to pick up magnetic varying magnetic flux $\frac{d\Phi}{dt}$ and converted into flux density (B). In order to do so, the transfer function $V = f(B)$ originating from Faraday's law of induction was considered¹²:

$$V = -n \cdot \frac{d\Phi}{dt} = -n \cdot A \cdot \frac{dB}{dt} \quad (3.8)$$

, where n is the number of turns in the pickup coil with an area A , and $d\Phi$ is the magnetic flux through it. Then, by assuming that the picked-up signal is a sine wave ($B \cdot \sin(2\pi f \cdot t)$) and that the pick-up coil is in a ring form ($A = \frac{\pi \cdot D_c^2}{4}$), equation 1.8 was rewritten as:

$$V = \frac{1}{2} \cdot B \cdot \pi^2 \cdot D_c^2 \cdot n \cdot f \quad \therefore \quad B = \frac{2V}{\pi^2 \cdot n \cdot f} \quad (3.9)$$

, where V is the measured induced voltage value in the coil, B is the magnetic flux density, D_c is the coil diameter and f is the operating frequency of the system¹³.

Finally, the magnetic flux density is converted into magnetic field intensity:

$$H = B \cdot \mu_0 = B \cdot (4 \cdot \pi \cdot 10^{-7}) \quad (3.10)$$

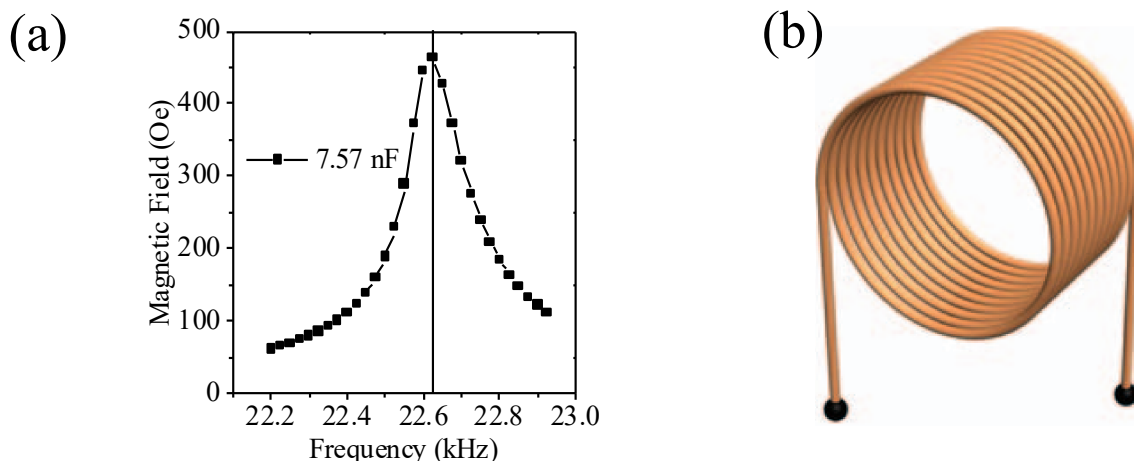


Figure 3.7: (a) Resonance frequency at 22.625 kHz using a 7.57 nF capacitor to achieve 460 Oe; (b) Coil-based magnetic flux sensor¹³

The field generated across the gap was observed to be homogeneous across the gap, and rapidly reduced and reached almost zero values while moving away from the gap. This magnetic field was used to actuate the heterostructures in Chapters 4 and 5 to evaluate the relative electric field by catalytic pollutant degradation and to wirelessly electrostimulate the cells.

The magnetic actuator system design, development and optimization was done by me at the laboratory of Magnetic Nanostructures of the Catalan Institute of Nanoscience and Nanotechnology (ICN2), and the pickup coil was developed by the company BlackHand Dynamics.

3.2.6. Indirect Evaluation of the Global ME-induced Electric Fields by Catalytic Degradation of Methylene blue

The field induced ME response of the structures in Chapters 4 and 5 was demonstrated by observing their catalytic effect in pollutant degradation.

Since quantifying the global electric field generated by nanostructured materials is very complex, an indirect way was used to evaluate the generated electric fields. Namely, the electric field induced methylene blue (MB) dye degradation was used as indirect evidence of the generation of electric fields. Note that, although this approach is not quantitative, the relative changes in degradation induced by the different conditions (materials, magnetic fields, frequencies) can be readily compared.

The procedure involves mixing the MB with peroxymonosulfate (PMS) at 0.3 mM, which initiated the degradation procedure¹⁴. The process entails the generation of sulfate radicals ($\text{SO}_4^{\bullet-}$) by the PMS, which are oxidising agents, and react with the MB molecules, breaking them down into less toxic molecules (e.g., CO_2 , H_2O , and simpler organic compounds such as CH_2O and CH_2O_2). The introduction of an electric field into the reaction activates the PMS by electro-oxidation, generating

additional reactive species such as hydroxyl radicals ($\text{OH}\bullet$) and hydrogen peroxide (H_2O_2), accelerating the degradation of the dye.

Note that the MB has an absorbance peak at 664 nm. This makes it straightforward to track the degree of degradation simply by monitoring the intensity of the absorbance peak with time.

The heterostructure (size 1 cm x 1 cm) was placed in a quartz cuvette and immerse in 2 mL of the MB-PMS solution. The cuvette was then placed inside the gap of the electromagnet with magnetic fields of different values (0 Oe to 300 Oe) and frequencies (0 Hz to 10 kHz). The samples were orientated in-plane to the applied field. The progress of degradation was monitored at room temperature by measuring the absorbance at 664 nm using a Flame-NIR miniature spectrometer. The measurements were taken in 30-minute intervals for 3 hours.

3.2.7. Biological Characterisation

3.2.7.1. Cell Viability, Proliferation Assays

Human osteoblast cells (hOBs), isolated from trabecular bone explants, were obtained from human bones with the approval of the Ethics Committee (Comissió d'Ètica en Experimentació Animal i Humana) of the Universitat Autònoma de Barcelona (CCEAH-2672). The hOBs were cultured in Dulbecco's Modified Eagles Medium (DMEM, ThermoFisher Scientific) supplemented with 20% foetal bovine serum (FBS, ThermoFisher Scientific) and 2% Penicillin-Streptomycin (P/S, Biowest) under standard conditions (37 °C and 5% CO_2).

The Au/ZnO/FeGa/PDMS thin films from Chapter 4 were sterilized by UV light and introduced into a 6-multiwell cell culture plate. Then, 100,000 cells were seeded into each well and cultured for 24 h to allow cell adhesion. After that, the films were transferred to special cuvettes for culturing cells under magnetic field. The films were subjected to a daily magnetic field of 400 Oe (at 100 Hz) for 1 h to induce an electrical stimulation (ES). In parallel, control films were cultured under standard conditions without the magnetic field (n-ES). After 7 days in culture, cell viability and cell proliferation were evaluated using the Live/Dead Viability/Cytotoxicity kit for mammalian cells (Invitrogen), according to the manufacturer's protocol. Images from randomly selected regions for ES and n-ES conditions were obtained using an Olympus IX71 inverted microscope. The experiments were performed in triplicate. A minimum of 500 cells were analysed per group. For the proliferation evaluation, the percentage of the layers covered by cells on day 7 after culture was quantified using Image J software (NIH).

Cell viability and biocompatibility of the Au/FeGa/BaTiO₃ heterostructure configurations was evaluated under the same experimental parameters, but were grown over 3 days.

The statistical analysis of cell viability and proliferation were performed using the Fisher's exact test and t-student test, respectively. Statistical significance was considered when $p < 0.05$.

3.2.7.2. Calcium Transient Assays

The ME response of the Au/FeGa/BaTiO₃ suspended microdiscs was qualitatively evaluated by observing the calcium internal peaks generated by the stimulations of voltage gated Ca channels of Saos-2 human osteosarcoma cells, under magnetic field actuation. The human osteosarcoma cell line Saos-2 (American Type Culture Collection, USA) was cultured in Dulbecco's modified Eagle medium (DMEM; ThermoFisher Scientific, UK) with 10% fetal bovine serum (FBS; Life Technologies, UK) under standard conditions (37 °C and 5% CO₂) on the samples for 24 h. Then, cells were loaded with 2 μM Fluo-4 AM (Life Technologies) in serum-free DMEM for 30 min in the dark. Samples were washed with serum-free DMEM and transferred to special culture dish with fresh medium.

The cells cultured on the Au/FeGa/BaTiO₃ suspended microdiscs were exposed to a magnetic field of 200 Oe ac (at 100 Hz), and their intracellular calcium levels were studied over time. The study consisted of 5 minutes of no magnetic stimulation, followed by 15 minutes of magnetic stimulation. Confocal laser scanning microscopy (Leica SP5) was used to detect intracellular calcium fluctuations over time. Fluorescent calcium indicators were used which selectively bind to the generated calcium ions (Ca²⁺), thereby generating the fluorescence signal. When the laser in the confocal microscope interacts with the calcium-bound indicators, it excites the fluorophores (fluorescent molecules) and causes them to emit fluorescent light. The emitted light is then detected by the microscope's detectors, allowing the visualization and measurement of the fluorescence signal. Images of osteoblasts were captured every 1 s during 20 min. These assays provided insights into the cellular processes, including cell signalling and cell responses caused by the ME effect. For reference, the same experiment was carried out on a plain Si substrate.

3.4. REFERENCES

1. Gerbредers, V. *et al.* Hydrothermal synthesis of ZnO nanostructures with controllable morphology change. *Cryst Eng Comm* **22**, 1346–1358 (2020).
2. Padvі, M. N., Harale, N. S., Patil, P. S., Dhas, S. D. & Moholkar, A. v. Hydrothermal synthesis of NO₂ gas-sensitive and hydrophobic zinc oxide thin films. *J Mater Sci Mater Electron* **32**, 3140–3154 (2021).
3. Mohan, S., Vellakkat, M., Aravind, A. & U, R. Hydrothermal synthesis and characterization of Zinc Oxide nanoparticles of various shapes under different reaction conditions. *Nano Express* **1**, 030028 (2020).
4. Murillo, G. *et al.* Role of aluminum and HMTA in the hydrothermal synthesis of two-dimensional n-doped ZnO nanosheets. *Nano Energy* **60**, 817–826 (2019).
5. Shrishа, B. V., Bhat, S., Kushavah, D. & Gopalakrishna Naik, K. Hydrothermal growth and characterization of Al-doped ZnO nanorods. *Mater Today Proc* **3**, 1693–1701 (2016).
6. Murillo, G., Lozano, H., Cases-Utrera, J., Lee, M. & Esteve, J. Improving Morphological Quality and Uniformity of Hydrothermally Grown ZnO Nanowires by Surface Activation of Catalyst Layer. *Nanoscale Res Lett* **12**, 51 (2017).
7. Stefani, C. Mechanical and electromechanical properties of ferroelectrics at the nanoscale studied by Atomic Force Microscopy. PhD Thesis (Universitat Autònoma de Barcelona, 2022).
8. Kholkin, A. L., Kiselev, D. A. & Heredia, A. Piezoresponse Force Microscopy. in *Encyclopedia of Materials: Science and Technology* (Elsevier, 2011) p. 1–8.
9. Stefani, C. *et al.* Mechanical reading of ferroelectric polarization. *J Appl Phys* **130**, 074103 (2021).
10. Gruverman, A., Alexe, M. & Meier, D. Piezoresponse force microscopy and nanoferroic phenomena. *Nat Commun* **10**, 1661 (2019).
11. Caruntu, G., Yourdkhani, A., Vopsaroiu, M. & Srinivasan, G. Probing the local strain-mediated magnetoelectric coupling in multiferroic nanocomposites by magnetic field-assisted piezoresponse force microscopy. *Nanoscale* **4**, 3218 (2012).
12. Kinsler, P. Faraday’s Law and Magnetic Induction: Cause and Effect, Experiment and Theory. *Physics (College Park Md)* **2**, 148–161 (2020).
13. Tumanski, S. Induction coil sensors—a review. *Meas Sci Technol* **18**, R31–R46 (2007).
14. Khan, I. *et al.* Review on Methylene Blue: Its Properties, Uses, Toxicity and Photodegradation. *Water (Basel)* **14**, 242 (2022).

4. Highly Flexible FeGa/ZnO Magnetoelectric Thin Films

4.1. INTRODUCTION

Magnetolectric (ME) materials are structures in which the magnetic and electrical properties are coupled to each other. This coupling allows for the control of electric polarization by magnetic fields or magnetization by electric fields, making these materials appealing for a wide range of applications¹⁻⁴. Importantly, in many applications such as biomedicine⁵⁻⁸, sensing and monitoring⁹⁻¹², and energy harvesting^{11,13,14} require these materials to be conformable. Thus, in recent years there has been a considerable effort towards the development of flexible ME films and, hence reduction of the substrate clamping effect^{15,16} (see Section 1.1.3.1). Two common approaches are: (i) growing or embedding ME composites using flexible polymer-based substrates, such as polyurethane (PU)¹⁷ or polyethylene terephthalate (PET)^{18,19}, or (ii) using a flexible piezoelectric polymer, such as polyvinylidene fluoride-based polymers (PVDF)^{20,21} as an active part of the ME structure.

Despite their highly desirable properties, in most cases both types of approaches exhibit a somewhat moderate stiffness originating from the relatively high Young's modulus of the flexible layers or the overall structure, which may, to a certain extent hinder their mechanical properties. Therefore, highly flexible ME systems would be appealing for a range of applications due to their ease of integration into various types of devices that require very flexible or highly conformable structures.

Here, we have fabricated a highly flexible magnetolectric film composed of hydrothermally synthesized piezoelectric ZnO nanosheets covered with magnetostrictive FeGa layer and embedded in a polydimethylsiloxane (PDMS) elastomer layer. The heterostructure shows excellent flexibility and good ME properties. The performance of the structure was demonstrated by inducing an enhanced cell proliferation of on human osteoblast cells under magnetic field induced electric stimulation.

4.2. RESULTS AND DISCUSSION

4.2.1. Design and Fabrication

The magnetoelastic films are composed of Au (50 nm) / Ti (10 nm) (electrode) / ZnO (8.5 μm) (piezoelectric) / FeGa (100 nm) (magnetostrictive) layers in a flexible PDMS (52 μm) layer (**Figure 4.1**).

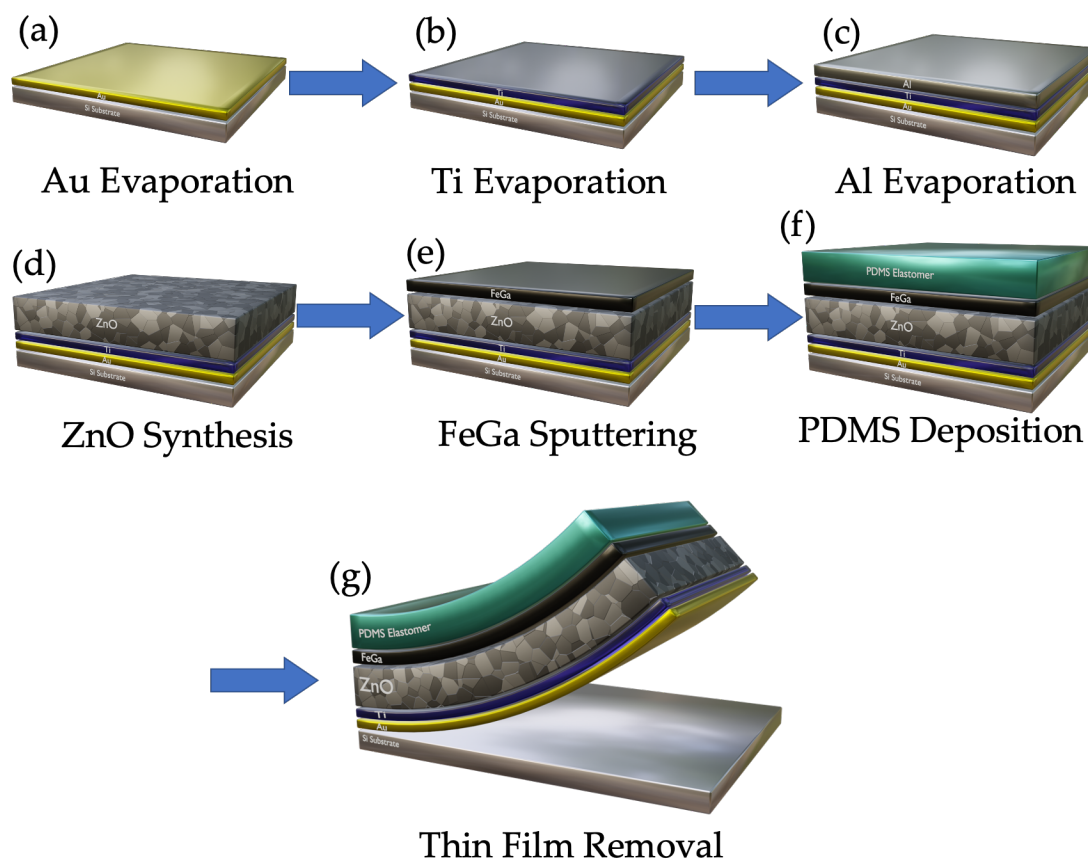


Figure 4.1: Fabrication process of the FeGa/ZnO composite integrated in the PDMS film.

The fabrication of the thin film involved the hydrothermally synthesized piezoelectric ZnO nanosheets on deposited Au/Ti/Al layers on a Si substrate (**Figure 4.1a, b, c, d**). Then, the ZnO nanosheets were covered by a layer of magnetostrictive FeGa (**Figure 4.1e**). The flexible elastomer was deposited on top using spin-coating (**Figure 4.1f**) and placed in a convection oven in order to cure it. Thereafter, the thin film was removed from the substrate, leaving all the layers inside the elastomer (see Experimental Techniques Section).

4.2.2. Morphological Characterization

The scanning electron microscopy (SEM) image of ZnO layer shows that it grows as highly dense, uniformly distributed ZnO nanosheets, oriented perpendicular to the film plane (**Figure 4.2a**). This “flaky” morphology is typical of the hydrothermal synthesis of ZnO²².

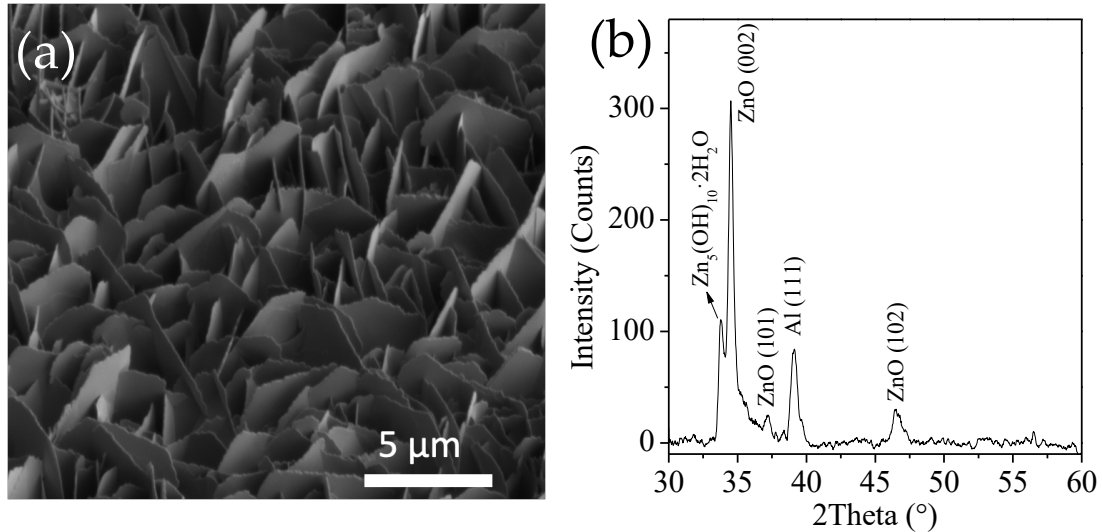


Figure 4.2: (a) SEM image of the ZnO layer; (b) X-ray diffraction pattern of the ZnO layer.

X-ray diffraction (XRD) evidences that the ZnO layer is hexagonal (hcp) (**Figure 4.2b**) and it grows textured along the c-axis. Note that the XRD also shows the presence of a layered double zinc hydroxide, which is likely an intermediate phase in the growth of the hcp-ZnO phase.

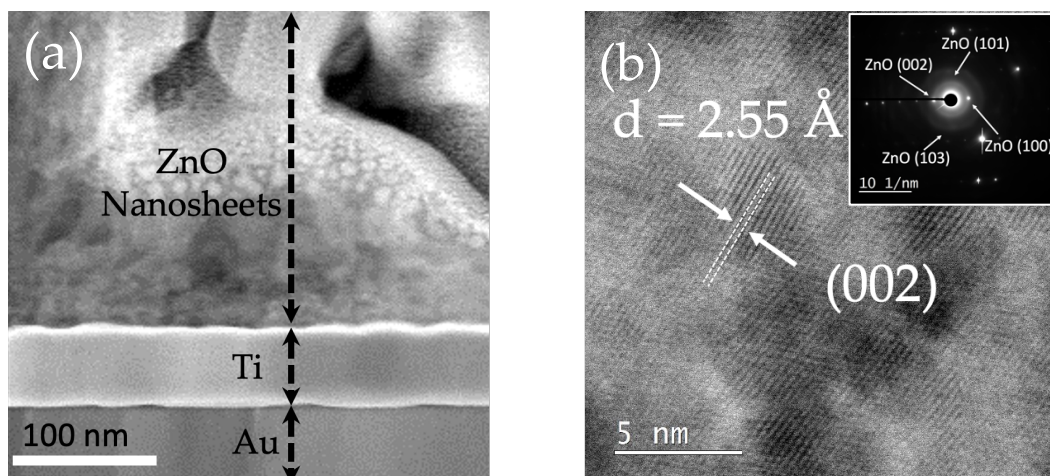


Figure 4.3: (a) Low-resolution cross-section TEM Image and (b) High-resolution cross-section TEM image of the FeGa/ZnO thin film. The interplanar distance of 2.55 Å corresponds to the hcp-ZnO (002) plane. The inset in (b) shows the corresponding selected area electron diffraction pattern (SAED) of the image.

The low-resolution transmission electron microscopy (TEM) images show the Au and the Ti layers (**Figure 4.3a**). The images also show that at the interface the ZnO layer is somewhat inhomogeneous, probably due to the growth of intermediate phases. After about 100 nm, the ZnO layer becomes more homogeneous and branches out into the nanosheets observed in the SEM (**Figure 4.2a**). The interplanar distance and the selected area diffraction of the high-resolution TEM image confirm the hcp character of the ZnO layer (**Figure 4.3b**).

To confirm the overall structure, electron energy loss spectroscopy (EELS) mapping of the TEM cross section of the Au/Ti/ZnO/FeGa/PDMS composite structure was carried out. The ZnO nanosheets were estimated using the Kramers-Kronig sum method²³ to be about 11 nm thick (**Figure 4.4a**) and about 8.5 μm long, in concordance with the SEM results. Interestingly, the Al sheet deposited as a seed layer (**Figure 4.4b**) rather than remaining as a layer in the bottom like the Au or Ti layers (**Figure 4.4c**), it is spread over the whole structure. Namely, during the ZnO growth process, the Al layer is dissolved and integrated into the newly formed structures during the ZnO deposition process forming Al doped ZnO sheets^{24,25} (**Figure 4.4d**). Interestingly, due to the flaky structure of the ZnO, the FeGa layer does not form a homogenous coating, but it deposits mainly on the top part of the ZnO flakes (**Figure 4.4e**). The thickness of the deposited PDMS elastomer was measured by observing the SEM image of the cross-section to be about 52 μm (**Figure 4.4f**).

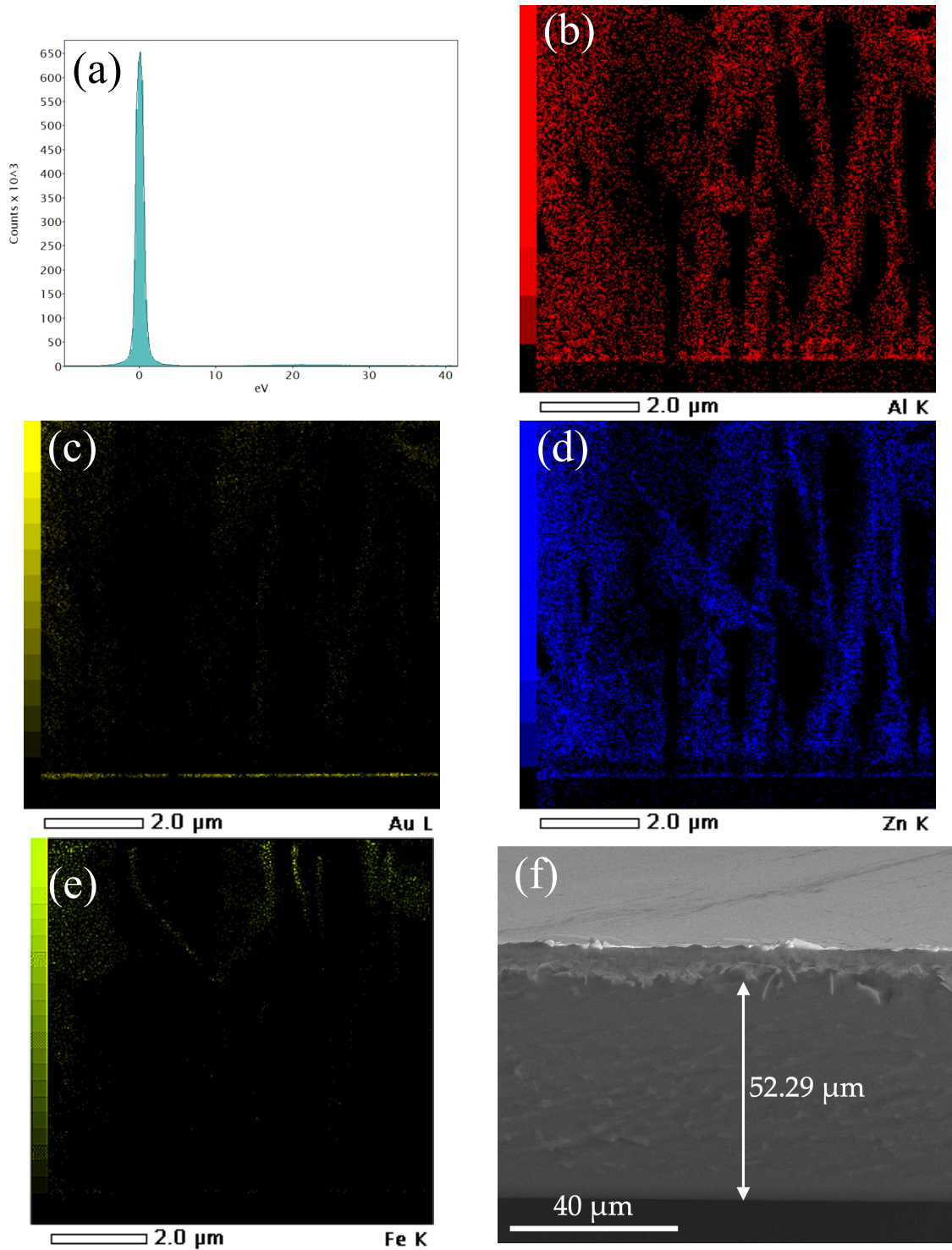


Figure 4.4: (a) Low-loss spectra EELS measurements for ZnO nanosheet thickness determination; Elemental mapping of the ZnO/FeGa structures using the (b) Al; (c) Au; (d) Zn; (e) Fe edges, respectively; and (f) SEM cross-section of the Au/Ti/ZnO/FeGa/PDMS film.

4.2.3. Magnetic Characterization

The magnetization properties of the structures were investigated using a variable sample magnetometer (VSM). Shown in **Figure 4.5**, the magnetization measurements of the composite Au/Ti/ZnO/FeGa/PDMS structures show that the structure has an in-plane magnetization with a moderate coercivity ($H_c = 200$ Oe).

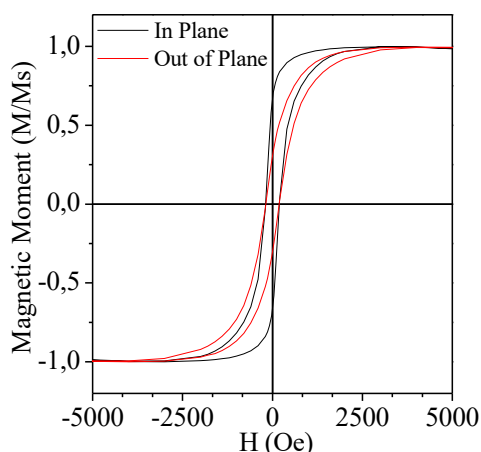


Figure 4.5: Normalized in-plane and out-of-plane magnetic hysteresis loops of the FeGa/ZnO composite.

4.2.4. Piezoelectric Characterization

The piezoelectric character of the ZnO nanosheets was confirmed by piezo force microscopy (PFM). From the slope of the displacement curve obtained from the PFM analysis (**Figure 4.6**), the estimated piezoelectric coefficient of the ZnO nanosheets in the composite structure was found to be $d_{33} = 11.2 \pm 0.3$ pm V^{-1} . This value is consistent with the piezoelectric coefficient of similar ZnO structures reported in previous studies^{26,27}.

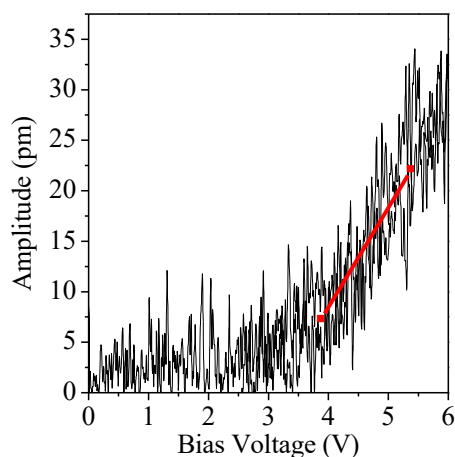


Figure 4.6: Electromechanical response of the ZnO nanosheets. The line indicates the linear part of the curve used to extract d_{33} .

4.2.5. Assessment of Mechanical Flexibility of Au/Ti/ZnO/FeGa/PDMS Film

The highly flexible character of the composite films was confirmed by measuring the angular displacement when applying magnetic fields in different directions by approaching permanent magnets near fixed cantilevers cut from the film (Figure 4.7).

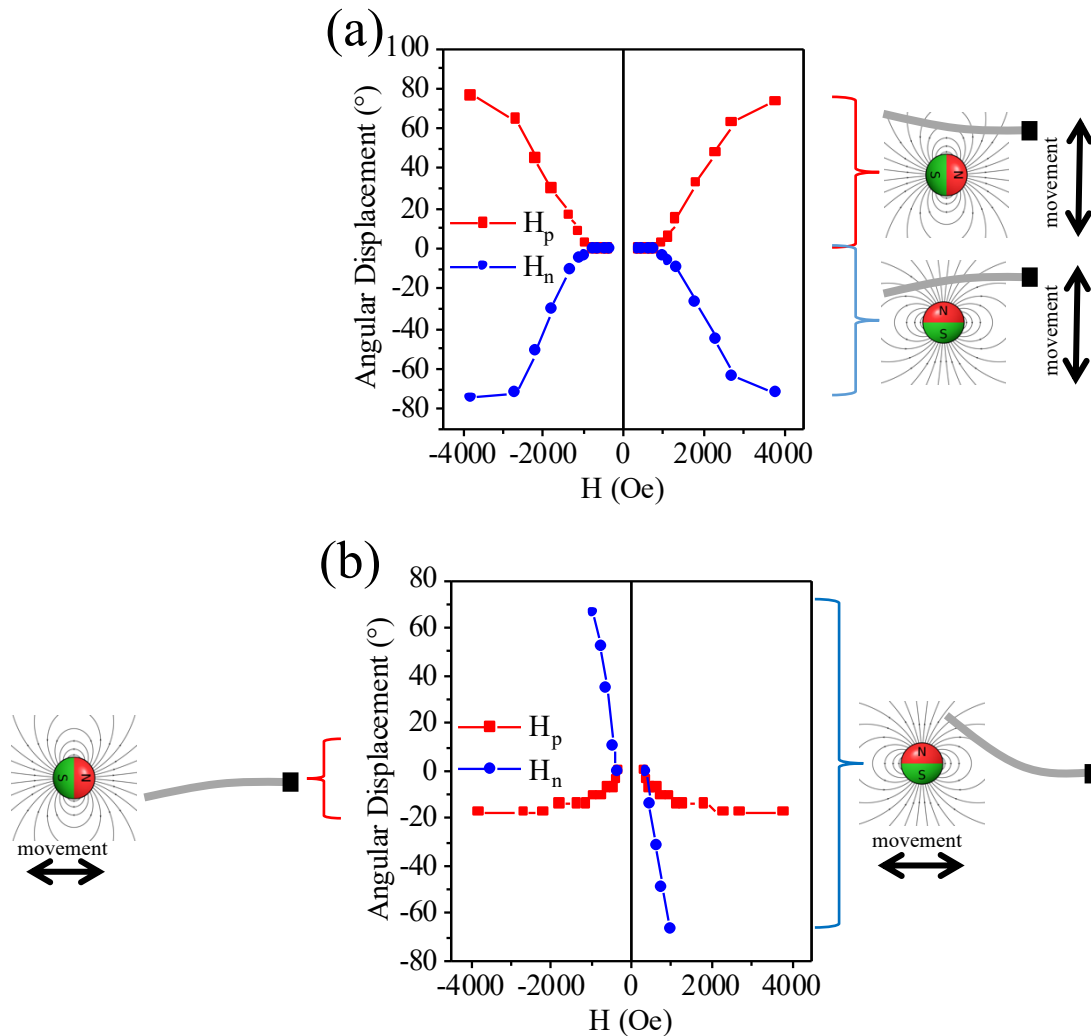


Figure 4.7: Magnetomechanical response of the FeGa/ZnO composite using a magnet moving (a) perpendicular and (b) parallel to the Au/Ti/ZnO/FeGa/PDMS cantilevers clamped on one side, with the direction of the magnetic field either along (H_n) or perpendicular (H_p) to the cantilever.

Remarkably, the flaky structure of the ZnO and the discontinuous nature of the FeGa layer allows the structure to maintain the high flexibility and conformability of the PDMS layer without jeopardising the piezoelectric properties of the ZnO.

4.2.6. Indirect Evaluation of the ME-induced Electric Fields by the Catalytic Degradation of Methylene Blue

The global ME response of the heterostructure was indirectly evaluated by observing the methylene blue (MB) degradation under magnetic field induced electric actuation. An indirect method was chosen firstly because of the very peculiar morphology of the ZnO nanosheets which complicates any measurements, and secondly to investigate the global response, which in contrast to the PFM local characterization, it does not measure at the nanoscale, but assesses the macroscopic response of the heterostructure.

The sample was immersed in a mixture of MB and peroxymonosulfate (PMS) which initiated the degradation process. This degradation process is known to be enhanced by the presence of electric fields²⁸. Thus, to generate the electric fields magnetic fields of different intensities and frequencies were applied. The evolution of the degradation is tracked by the change over time of the intensity of the light absorption peak of MB, which changes colour as it degrades (*Figure 4.8a*).

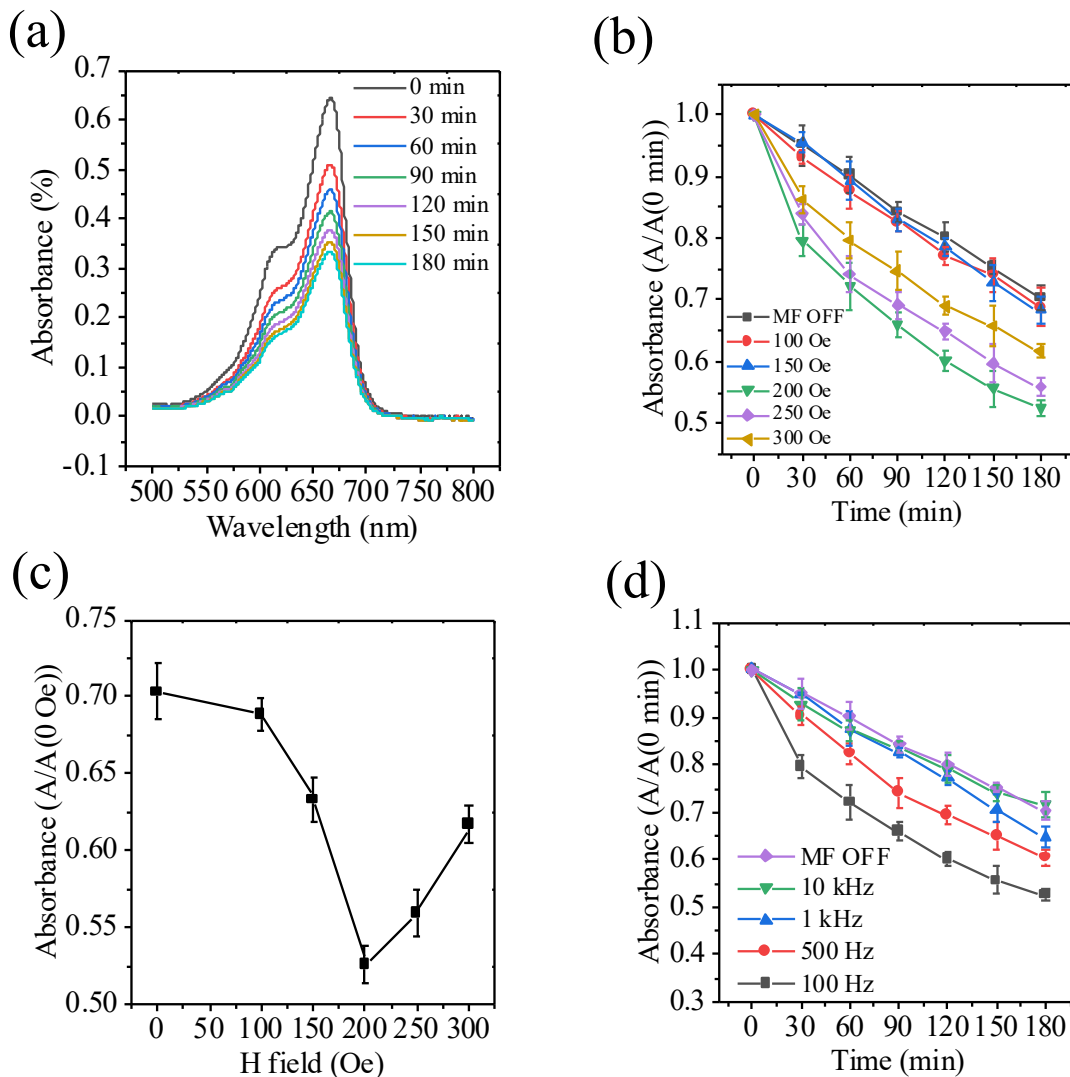


Figure 4.8: (a) Evolution of the absorption peak of MB at different times (200 Oe at 100 Hz); (b) Dependence of the normalized absorbance at 664 nm on the actuation time using different magnetic field values at a frequency of 100 Hz; (c) Dependence of the normalized absorbance at 664 nm after 3 h on the applied magnetic field; (d) Dependence of the normalized absorbance at 664 nm on the actuation time using different frequencies, using 200 Oe. Error bars indicate the standard deviation of the replicated experiments.

Interestingly, the level of MB degradation has a non-monotonic dependence on the applied field, where the largest degradation after 3 hours, representing the largest ME response, occurred when the structure was placed under 200 Oe at 100 Hz (0.526 ± 0.013 A/A(0 min)) (Figure 4.8 b, c). The dependence of the degradation on the applied field observed in the ME response of the material (Figure 4.8c) can be attributed to magnetostriction-induced strain of the FeGa layer. Magnetostriction often exhibits a maximum at intermediate fields²⁹, which implies that at this specific field the strain transfer to the piezoelectric material would be maximum. Consequently, the generated electric field would also peak at the same field.

On the other hand, the degradation becomes weaker as the frequency increases (*Figure 4.8 d*). This effect may be more related to chemical aspects of the degradation process (e.g., the limited mass transport towards the active surface at high frequencies), than to a ME effect. More studies are necessary to elucidate the role of frequency in the ME effects.

4.2.7. Biocompatibility and Proliferation Assays

To confirm the biocompatibility of the heterostructures, their cytotoxicity was assessed. The potential cytotoxic effect of the films and the electrical stimulation on human osteoblast cells (hOBs) were analysed by quantifying the number of live cells with esterase activity, and the number of dead cells. The percentage of live cells after 24 h was higher than 94% for both electrically stimulated (ES) and non-electrically stimulated (n-ES) films, indicating that the films are indeed biocompatible. In addition, no significant differences in viability were found when comparing the stimulated with non-stimulated films (*Figure 4.9*).

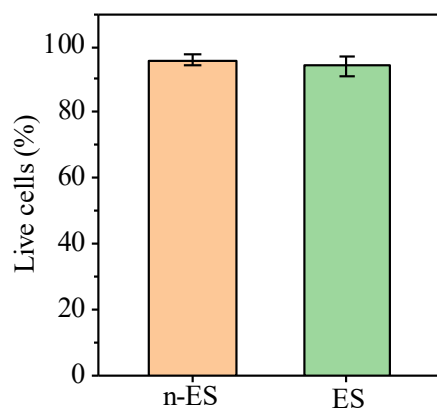


Figure 4.9: Cell viability of non-electrically stimulated (n-ES) and electrically stimulated (ES) hOBs on ZnO/FeGa/PMDS films; Error bars indicate the standard deviation of the replicated experiments.

Since the cells cultured on the films in both conditions showed exceptional viability and adhesion, their proliferation was assessed. To evaluate the effect of the magnetic field-induced electrostimulation on the proliferation of hOBs, the cells were either (i) cultured on the films and were magnetically stimulated (400 Oe at 100 Hz) for 1 hour per day, for 7 days or (ii) cultured without applied field. The cell surface area coverage was quantified on day 7 and the results showed that the proliferation of hOBs was significantly enhanced on the stimulated films compared to the non-stimulated films. Namely, the percentage of surface area covered by cells was 40% for electrically stimulated films compared to 26% for non-electrically stimulated ones.

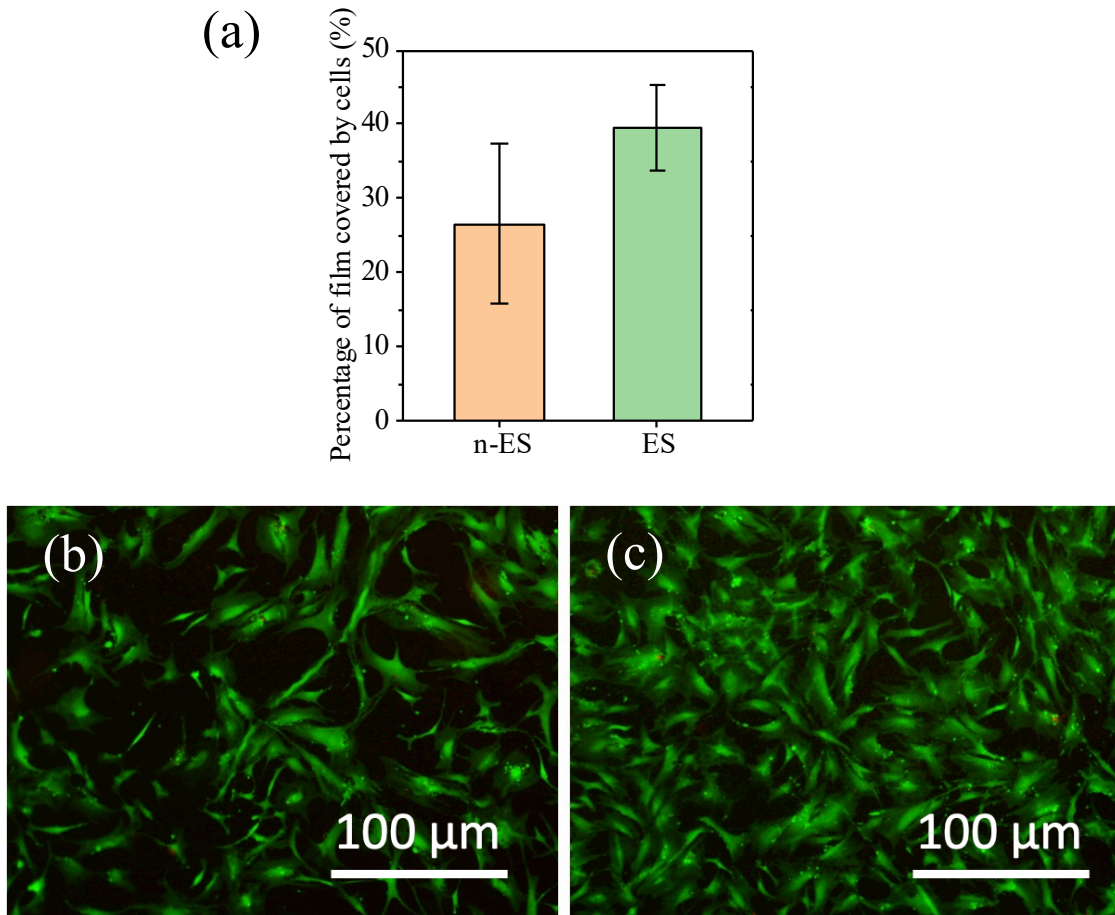


Figure 4.10: (a) Proliferation of human osteoblasts grown for 7 days in culture for both conditions (non-electrostimulated, n-ES, and magnetically-induced electrostimulated, ES); Error bars indicate the standard deviations of the replicated experiments. (b) Cell viability image of non-electrostimulated hOBs.; (c) Cell viability image of electrostimulated hOBs.

The enhanced proliferation observed, can be attributed to the ME-induced electric field produced by the films under magnetic field, which increases the intracellular calcium ion concentration, activating signalling pathways responsible for cell growth and proliferation (Chapter 2). The enhanced proliferation is probably related to the flexible character of the heterostructure which allows for an efficient transmission of the mechanical forces between the magnetostrictive and piezoelectric layers (i.e., reduced clamping effect).

4.3. CONCLUSIONS

We have developed a highly flexible magnetoelectric Au/Ti/FeGa/ZnO heterostructure embedded in a polydimethylsiloxane (PDMS) elastomer layer, capable of wirelessly producing electric fields when placed under an external magnetic field. While the combination of the piezoelectric ZnO and magnetostrictive FeGa layers allows for the production of electricity via magnetic field, the flexible elastomer gives the structure its conformable property. The hydrothermally-grown hexagonal (hcp) ZnO nanosheet layer grows textured along the c-axis, and its piezoelectric character was confirmed by piezo force microscopy (PFM), with an estimated piezoelectric coefficient of $d_{33} = 11.2 \pm 0.3 \text{ pm V}^{-1}$. Magnetization measurements of the composite film showed that it had an in-plane magnetization with a moderate coercivity of $H_c = 200 \text{ Oe}$. Moreover, we indirectly evaluated the ME response of the heterostructure by observing the electric field induced methylene blue (MB) degradation under magnetic field actuation. The results showed that the strongest degradation occurred in the presence of a 200 Oe magnetic field at a frequency of 100 Hz, indicating that these conditions generate the largest electric fields. Finally, the heterostructures were shown to be biocompatible. In addition, cell proliferation studies, comparing the stimulated and non-simulated cells, showed that after 7 days of 1 h daily ME stimulation, the stimulated cells exhibited a 42% enhancement in the proliferation. Overall, the highly flexible magnetoelectric composite film demonstrated in this study could be useful for various applications, including soft ME implants in biomedicine or for energy harvesting. The ease of integration into various types of devices requiring highly flexible and conformable structures makes this composite film particularly attractive. Future studies could explore further optimization of the composite film structure and investigate the performance of the film in different applications.

4.4. REFERENCES

1. Kopyl, S., Surmenev, R., Surmeneva, M., Fetisov, Y. & Kholkin, A. Magnetolectric effect: principles and applications in biology and medicine—a review. *Mater Today Bio* **12**, 100149 (2021).
2. Chen, X.-Z. *et al.* Hybrid Magnetolectric Nanowires for Nanorobotic Applications: Fabrication, Magnetolectric Coupling, and Magnetically Assisted In Vitro Targeted Drug Delivery. *Adv Mater* **29**, 1605458 (2017).
3. Wang, Y., Li, J. & Viehland, D. Magnetolectrics for magnetic sensor applications: status, challenges and perspectives. *Mater Today* **17**, 269–275 (2014).
4. Liang, X., Chen, H. & Sun, N. X. Magnetolectric materials and devices. *APL Mater* **9**, 041114 (2021).
5. Chen, J. C. *et al.* A wireless millimetric magnetolectric implant for the endovascular stimulation of peripheral nerves. *Nat Biomed Eng* **6**, 706–716 (2022).
6. Spaldin, N. A. & Ramesh, R. Advances in magnetolectric multiferroics. *Nat Mater* **18**, 203–212 (2019).
7. Singer, A. *et al.* Magnetolectric Materials for Miniature, Wireless Neural Stimulation at Therapeutic Frequencies. *Neuron* **107**, 631–643 (2020).
8. Hoque Apu, E. *et al.* Biomedical applications of multifunctional magnetolectric nanoparticles. *Mater Chem Front* **6**, 1368–1390 (2022).
9. Bichurin, M. *et al.* Magnetolectric Magnetic Field Sensors: A Review. *Sensors* **21**, 6232 (2021).
10. Ghosh, S. K. *et al.* Rollable Magnetolectric Energy Harvester as a Wireless IoT Sensor. *ACS Sustain Chem Eng* **8**, 864–873 (2020).
11. Zaeimbashi, M. *et al.* Ultra-compact dual-band smart NEMS magnetolectric antennas for simultaneous wireless energy harvesting and magnetic field sensing. *Nat Commun* **12**, 3141 (2021).
12. Wang, Y., Chen, J. & Lai, Y. Flexible magnetolectric complex oxide heterostructures on muscovite for proximity sensor. *npj Flexible Electronics* **7**, 10 (2023).
13. Lu, Z., Zhang, C., Kwon, S. H., Jiang, Z. & Dong, L. Flexible Hybrid Piezoelectric-Electrostatic Device for Energy Harvesting and Sensing Applications. *Adv Mater Interfaces* **10**, 2202173 (2023).
14. Liu, Z. *et al.* Flexible piezoelectric nanogenerator in wearable self-powered active sensor for respiration and healthcare monitoring. *Semicond Sci Technol* **32**, 064004 (2017).
15. Jana, B. *et al.* Recent Progress in Flexible Multiferroics. *Front Phys* **9**, 10 (2022).
16. Almusallam, A. *et al.* Clamping effect on the piezoelectric responses of screen-printed low temperature PZT/Polymer films on flexible substrates. *Smart Mater Struct* **24**, 115030 (2015).

17. Belouadah, R., Seveyrat, L., Guiffard, B. & Guyomar, D. Enhancement of the magnetolectric response of polyurethane polymer / piezoceramic bi-layer materials. *Sens Actuators A Phys* **299**, 111582 (2019).
18. Gao, W. *et al.* Flexible organic ferroelectric films with a large piezoelectric response. *NPG Asia Mater* **7**, e189 (2015).
19. Gupta, P. *et al.* Large Scale Exchange Coupled Metallic Multilayers by Roll-to-Roll (R2R) Process for Advanced Printed Magnetolectronics. *Adv Mater Technol* **7**, 2200190 (2022).
20. Wen, D. *et al.* Piezoelectric and Magnetolectric Effects of Flexible Magnetolectric Heterostructure PVDF-TrFE/FeCoSiB. *Int J Mol Sci* **23**, 15992 (2022).
21. Sharma, T., Aroom, K., Naik, S., Gill, B. & Zhang, J. X. J. Flexible Thin-Film PVDF-TrFE Based Pressure Sensor for Smart Catheter Applications. *Ann Biomed Eng* **41**, 744–751 (2013).
22. Murillo, G. *et al.* Electromechanical Nanogenerator-Cell Interaction Modulates Cell Activity. *Adv Mater* **29**, 1605048 (2017).
23. Iakoubovskii, K., Mitsuishi, K., Nakayama, Y. & Furuya, K. Thickness measurements with electron energy loss spectroscopy. *Microsc Res Tech* **71**, 626–631 (2008).
24. Murillo, G. *et al.* Role of aluminum and HMTA in the hydrothermal synthesis of two-dimensional n-doped ZnO nanosheets. *Nano Energy* **60**, 817–826 (2019).
25. Shrisha, B. V., Bhat, S., Kushavah, D. & Gopalakrishna Naik, K. Hydrothermal growth and characterization of Al-doped ZnO nanorods. *Mater Today Proc* **3**, 1693–1701 (2016).
26. Fu, J. Y., Liu, P. Y., Cheng, J., Bhalla, A. S. & Guo, R. Optical measurement of the converse piezoelectric d_{33} coefficients of bulk and microtubular zinc oxide crystals. *Appl Phys Lett* **90**, 21 (2007).
27. Abu Ali, T. *et al.* Piezoelectric Properties of Zinc Oxide Thin Films Grown by Plasma-Enhanced Atomic Layer Deposition. *Phys Status Solidi A* **217**, 21 (2020).
28. Nwanebu, E. O., Liu, X., Pajootan, E., Yargeau, V. & Omanovic, S. Electrochemical Degradation of Methylene Blue Using a Ni-Co-Oxide Anode. *Catalysts* **11**, 793 (2021).
29. Srisukhumbowornchai, N. & Guruswamy, S. Large magnetostriction in directionally solidified FeGa and FeGaAl alloys. *J Appl Phys* **90**, 5680–5688 (2001).

5. Suspended Au/FeGa/BaTiO₃ Magnetoelectric Microdiscs

5.1. INTRODUCTION

Magnetoelectric materials are systems in which the electric polarization can be controlled by the application of an external magnetic field, or, conversely, the magnetization can be tuned by the application of an electric field.¹ Due to their appealing properties, the interest in magnetoelectric materials has been steadily increasing during recent years. They are being investigated for a broad range of applications in widespread fields, ranging from sensors, transducers, energy harvesters or random-access memories, to biomedical uses.²⁻⁴

Due to the rarity of naturally occurring single-phase (intrinsic) magnetoelectric materials, during the last decades artificial magnetoelectric composites have been developed. These systems are usually composed of a ferroelectric and a magnetostrictive ferromagnetic phase, combining the properties of the two phases. However, the performance of many of these structures can be hindered by the so-called substrate clamping effect, particularly in thin films. Namely, due to the coupling between the films and the substrate, mechanical forces inducing the magnetoelectric effect cannot be efficiently transmitted between the ferromagnetic and ferroelectric counterparts, thus dramatically reducing the magnetoelectric effect. Although approaches to minimize clamping are being proposed,^{5,6,10,11} there are still issues to be solved for their application in devices.

In this work, we have fabricated magnetoelectric Au/FeGa/BaTiO₃ (ferromagnetic/ferroelectric) suspended microdisc heterostructures, where the magnetic field induced mechanical strain in the magnetostrictive FeGa layer can be effectively transferred to the BaTiO₃ ferroelectric phase, generating a strong electric polarization. The results evidence that due to their reduced clamping effects, the magnetoelectric performance of the suspended microdiscs is considerably better than the one in the non-suspended discs or films of the same composition.

5.2. RESULTS AND DISCUSSION

5.2.1. Design and Fabrication

The magnetolectric suspended microdisc heterostructures were fabricated by colloidal lithography and reactive ion etching from films composed of a bilayer of ferroelectric BaTiO₃ and magnetostrictive FeGa on a Si substrate, capped with a protective Au (5 nm) layer, which also serves as a top electrode. (**Figure 5.1**).

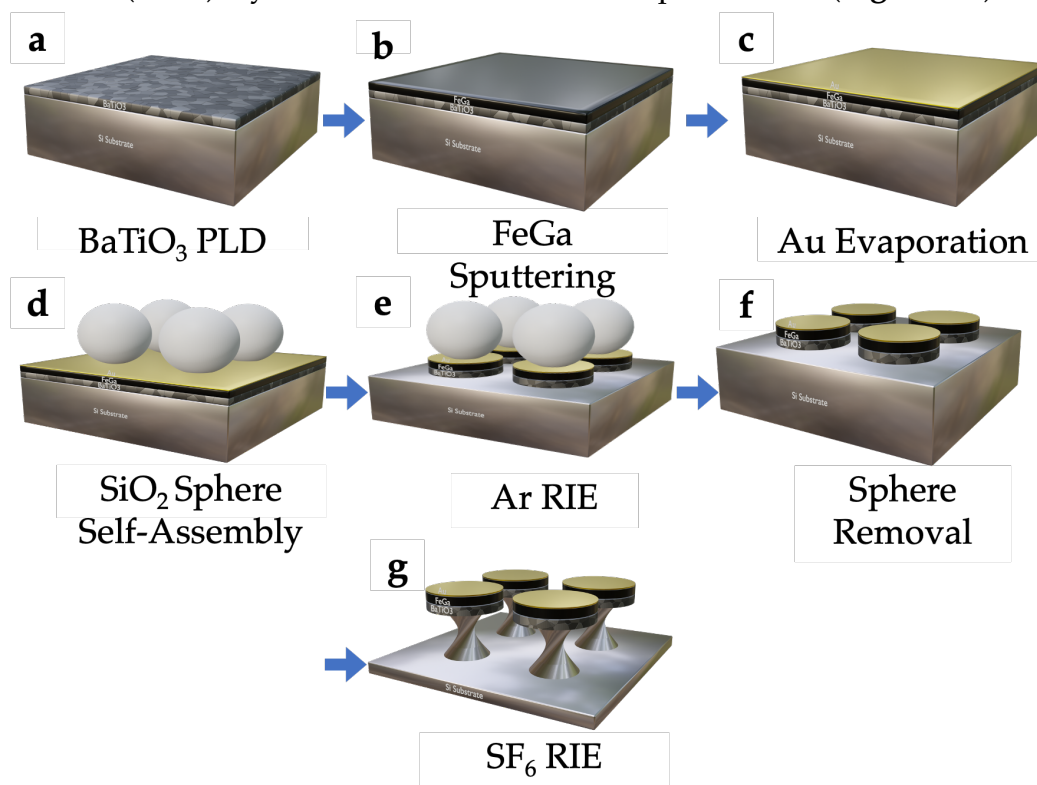


Figure 5.1: Schematic description of the fabrication process of Au/FeGa/BaTiO₃ suspended microdiscs. PLD-pulsed laser deposition; RIE-reactive ion etching.

For the fabrication of the suspended microdiscs, SiO₂ microspheres (2 μm) were assembled on the BaTiO₃/Fe₈₀Ga₂₀/Au films to serve as masks (**Figure 5.1d**). Subsequently, a first etching step was carried out (**Figure 5.1e**), followed the removal of the SiO₂ microspheres, which lead to the non-suspended microdiscs (**Figure 5.1f**). Finally, a second etching step was performed to partially remove the Si under the discs, resulting in the suspended microdiscs (**Figure 5.1g**).

5.2.2. Morphological and Structural Characterization

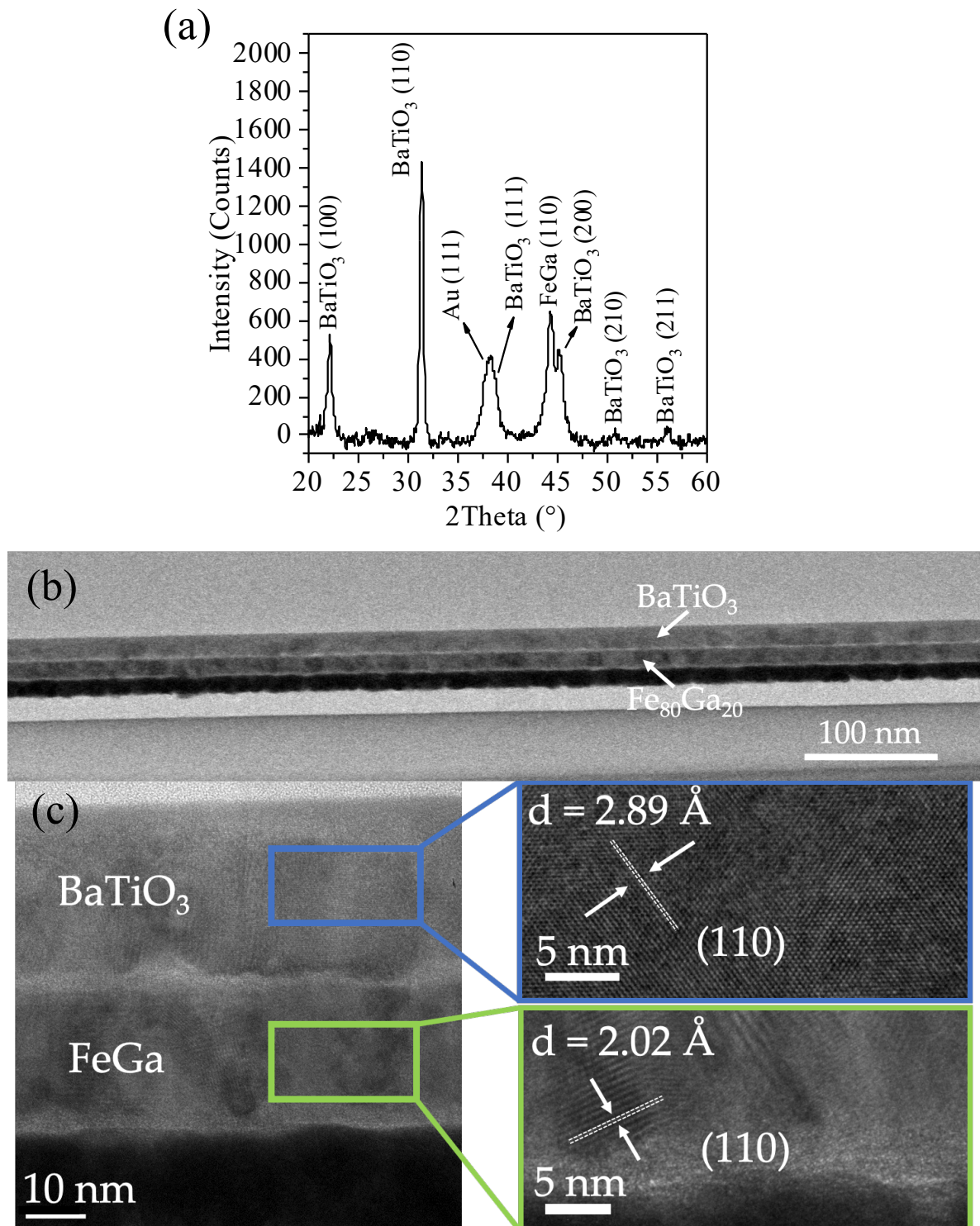


Figure 5.2: (a) X-ray diffraction pattern, (b) Low-resolution cross-section TEM Image and (c) High-resolution cross-section TEM image of the BaTiO₃/Fe₈₀Ga₂₀/Au continuous film. Shown in the right panel of (c) is an enlarged view of the areas highlighted by the rectangles in the left panel.

The x-ray diffraction pattern of the continuous film evidences that the BaTiO₃ and Fe₈₀Ga₂₀ layers are polycrystalline (**Figure 5.2a**). From the peak broadening, the crystallite sizes of the BaTiO₃ and Fe₈₀Ga₂₀ were estimated to be about 22 nm and 12 nm, respectively. From the low-resolution transmission electron microscopy (TEM) images, the thickness of the layers was determined to be 32 nm for the BaTiO₃ and 35 nm for the Fe₈₀Ga₂₀ layers, respectively. In addition, the in-plane crystallite size of the BaTiO₃ and the Fe₈₀Ga₂₀ layers were about 20 nm and 15 nm, respectively. The low-resolution and high-resolution TEM images confirm the polycrystalline character of the layers. (**Figure 5.2b, c**). Using energy-dispersive x-ray spectroscopy in the TEM, the composition of the FeGa layer was determined to be Fe₈₀Ga₂₀. From the enlarged images in **Figure 5.1c**, inter-planar distances of 2.89 Å and 2.02 Å were measured for BaTiO₃ and FeGa respectively, corresponding to the (110) planes of each material.

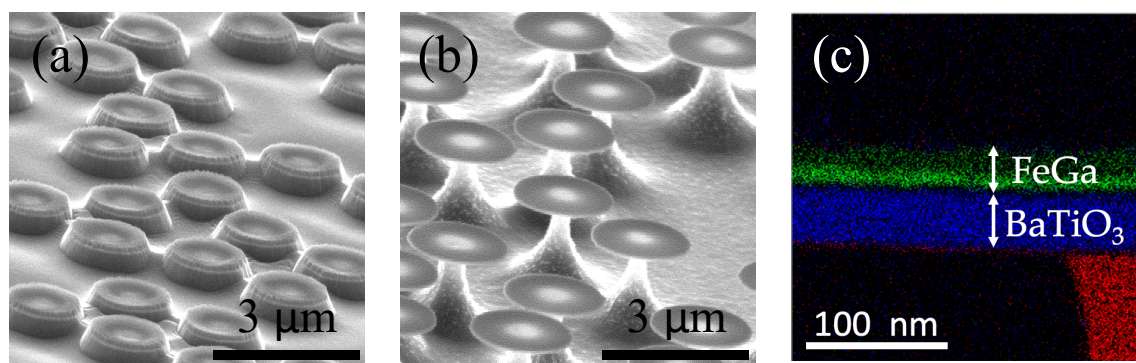


Figure 5.3: (a) 70°-Angled SEM Image of non-suspended microdiscs; (b) 70°-Angled SEM Image of suspended microdiscs; (c) EELS mapping of the cross-section TEM image of the suspended microdiscs, where green corresponds to the Fe signal, blue to Ba and red to Si, respectively.

The scanning electron microscopy (SEM) images clearly show the differences between the non-suspended and suspended discs (**Figure 5.3a, b**). Importantly, the suspended discs show that a large part of the disc is free standing, supported by a Si column. To confirm the structure, an electron energy loss spectroscopy (EELS) mapping of the TEM cross section of the suspended discs was carried out. As can be seen in **Figure 5.3c**, the BaTiO₃/Fe₈₀Ga₂₀ layers are mostly suspended and only the central part (about 500 nm) is supported by a Si column. Note that there is a hardly discernible Si signal under the suspended part of the microdiscs, which is estimated to be less than 4 nm thick.

5.2.3. Piezoelectric and Ferroelectric Characterization

Figure 5.4a shows the analysis of the electromechanical response of the different configurations, acquired using piezo force microscopy (PFM). Notably, while the continuous film and the centres of both microdisc structures exhibited similar mechanical responses, the edges of the non-suspended and suspended microdiscs showed a considerably stronger response. **Figure 5.4b** shows the piezoelectric coefficients obtained from Figure 5a. In the case of the continuous film, it was estimated to be $3.7 \pm 0.3 \text{ pm}\cdot\text{V}^{-1}$. The coefficient of the non-suspended microdiscs was estimated in the centre and on the edge of the disc to be $4.8 \pm 0.4 \text{ pm}\cdot\text{V}^{-1}$ and $7.7 \pm 0.4 \text{ pm}\cdot\text{V}^{-1}$, respectively. Finally, the suspended microdiscs exhibited an estimated coefficient of $4.6 \pm 0.4 \text{ pm}\cdot\text{V}^{-1}$ in the centre and $13.2 \pm 0.4 \text{ pm}\cdot\text{V}^{-1}$ on the edge. This enhanced piezoelectric coefficient can be attributed to the reduced clamping effect due to the geometry and the depletion of the Si substrate on the underside of the microdiscs, which allows for a larger freedom of movement for the nanostructured ferromagnetic/ferroelectric composites, especially at the edges of the nanostructure^{5-7,25}.

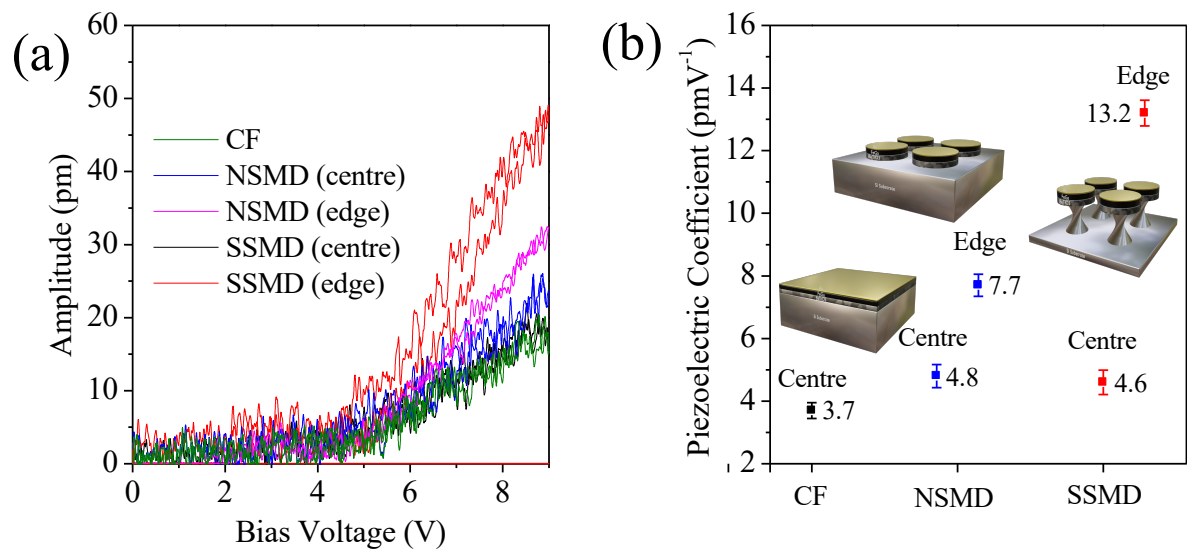


Figure 5.4: (a) Electromechanical response and (b) d_{33} piezoelectric coefficients for the three Au/FeGa/BaTiO₃ samples. Error bars indicate the standard deviations of the replicated experiments. CF = continuous film; NSMD = non-suspended microdiscs; and SSMD = suspended microdiscs. The insets show schematic drawings of the different structures.

The ferroelectric character of the composite was demonstrated by directly probing and poling the heterostructure using PFM in the continuous films. The dark and bright contrasts of the two concentric squares ($8 \mu\text{m} \times 8 \mu\text{m}$ and $3 \mu\text{m} \times 3 \mu\text{m}$) (**Figure 5.5**) indicate reversible polarization and remanence in both the amplitude and phase, and thus confirm the ferroelectric nature of the composite⁸. Additionally,

the 180° phase change between the different areas (**Figure 5.5b**) confirms that the response is almost purely electromechanical and not electrostatic^{8,9}.

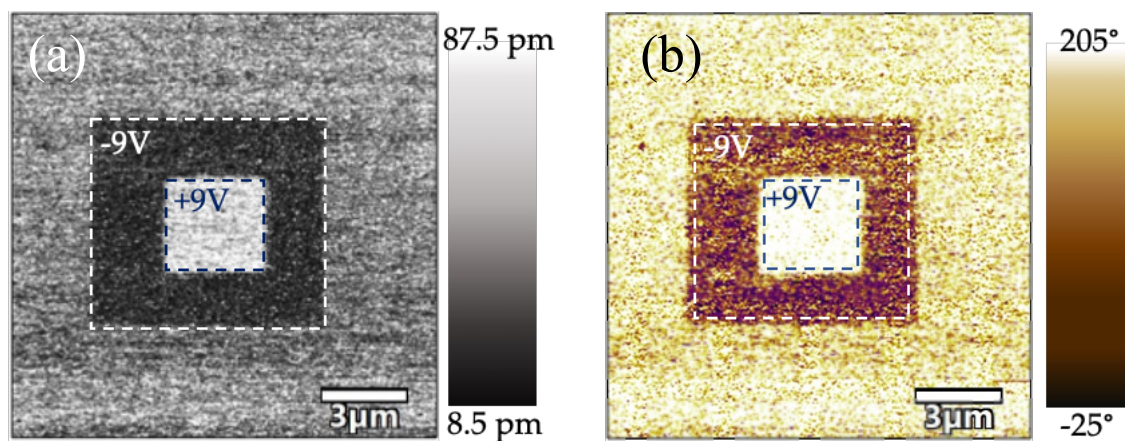


Figure 5.5: (a) PFM Amplitude and (b) Phase image obtained after two concentric squares recorded after applying a bias ± 9 VDC to the sample through the tip.

5.2.4. Magnetic and Magnetoelectric Characterization

The magnetic properties of the three structures show that the three samples have an in-plane magnetization with similar coercivity. However, the shape of the hysteresis loop changes for the three configurations, where the field required to saturate the sample increases from a few hundred Oe (100 Oe and 350 Oe, for the film and non-suspended microdiscs, respectively) to almost 2000 Oe for the suspended microdiscs, but with a similar coercivity in the in the three cases, around $H_c = 180$ Oe. These changes were linked on one hand to the patterning from a continuous film to a disc shape¹⁰ and on the other hand to the change of the strains acting on the ferromagnetic layer¹¹ once the Si layer was partially etched away.

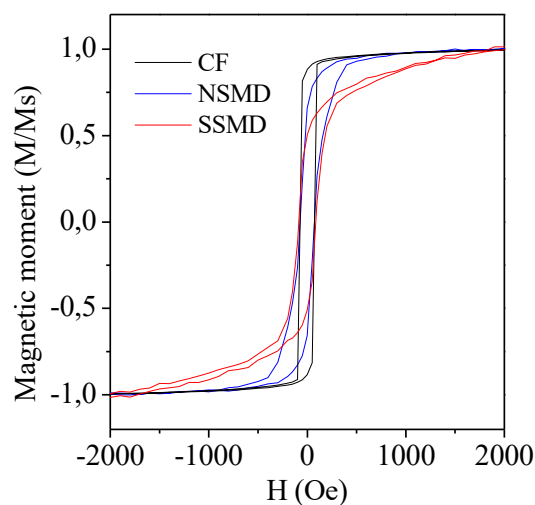


Figure 5.6: In-plane hysteresis loops for the three Au/FeGa/BaTiO₃ samples. CF = continuous film; NSMD = non-suspended microdiscs; and SSMD = suspended microdiscs.

The piezoresponse amplitude curves (**Figure 5.7a** and **c**) reveal the characteristic hysteretic “butterfly” shaped response, further validating the piezoelectric behaviour of the composite¹². Note that the asymmetry of the piezoresponse loops can originate from factors such as the internal electric fields of the materials or preferential polarization differences between the Pt-coated silicon probe and the Au electrode^{13–18}. Moreover, the fact that phase change with applied voltage is around 180° (**Figure 5.7b** and **d**) further corroborates that the response is electromechanical and not electrostatic^{9,19}.

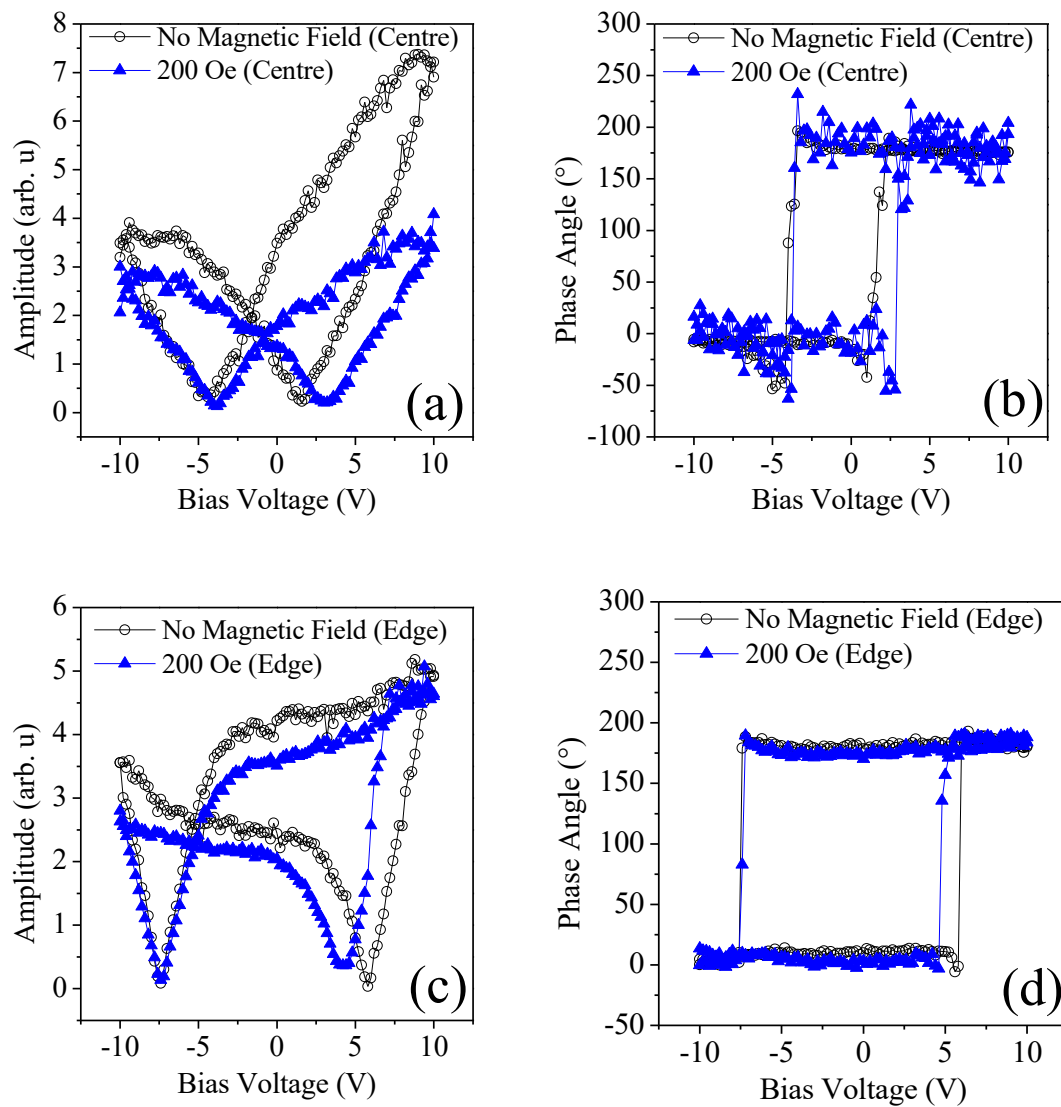


Figure 5.7: (a) Piezoresponse amplitude in the centre of the structure, with 200 Oe applied magnetic field and without magnetic field and (b) the corresponding piezoresponse phase loops; (c) piezoresponse amplitude on the edge of the structure, with 200 Oe applied magnetic field and without magnetic field and (d) the corresponding piezoresponse phase loops of the Au/FeGa/BaTiO₃ suspended microdiscs.

Remarkably, the piezoresponse depends both on the position and the applied field. Namely, different coercive voltages were observed in the local piezoresponse loops of **Figure 5.7** depending on the conditions. More specifically, in the case of the centre of the suspended microdiscs, without an applied magnetic field, the coercive voltages were 1.5 V and -5 V (**Figure 5.7a**), while on the edges they were 5.5 V and -7.5 V (**Figure 5.7c**), resulting to average coercive electric fields of 101 MV·m⁻¹ and 202 MV·m⁻¹, respectively. Note that for a given field there is a spread of ferroelectric coercive fields. This arises from the polycrystallinity character of the material, consisting of grains with different crystal orientations. Thus, the PFM tip locally

probes crystallites with different crystal orientation, which produces different ME responses.

As can be seen in **Figure 5.8**, the magnetoelectric coupling of all three samples decreases as the magnetic field is increased, which is related to the field dependence of magnetostriction²⁰. In addition, it is worth to emphasize that the magnetoelectric coupling coefficient of the continuous film was the lowest of the three morphologies.

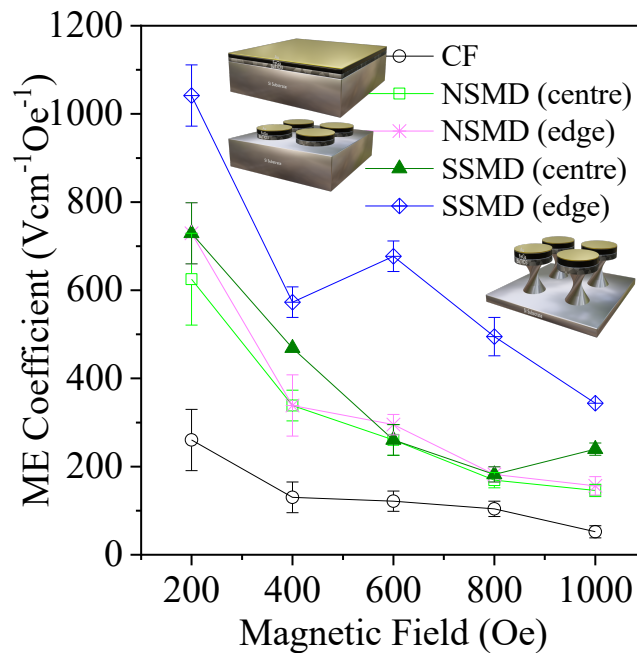


Figure 5.8: Magnetoelectric coupling coefficient value comparison of Au/FeGa/BaTiO₃ composite for the continuous film (CF), non-suspended microdiscs (NSMD) and suspended microdiscs (SSMD) in the centre and on the edge of the microdiscs, under different values of applied magnetic field. Error bars indicate the standard deviations of the replicated experiments.

The non-suspended discs have a larger coefficient than the films and the values are similar in the edge and the centre (**Figure 5.8**). On the other hand, the suspended structures, while the magnetoelectric coupling coefficient in the centre is comparable to the one of the non-suspended discs, on the edge they exhibit the largest coefficient. Remarkably, at 200 Oe, the edges of the suspended discs show an exceptional, more than 4-fold, increase with respect to the continuous films (from $260 \pm 70 \text{ V}\cdot\text{cm}^{-1}\cdot\text{Oe}^{-1}$ to $1040 \pm 70 \text{ V}\cdot\text{cm}^{-1}\cdot\text{Oe}^{-1}$). These values are, in fact, three orders of magnitude larger than macroscopic magnetoelectric coefficients of heterostructures of similar compositions²¹. However, local magnetoelectric coefficients obtained by PFM cannot be directly compared to macroscopic magnetoelectric coefficients, due to the varying coercive voltages originating from the inhomogeneous field created by the nano-scale contact between the tip of the

PFM and the polycrystalline layers of the heterostructure^{22–24}. Nevertheless, the values obtained for the suspended discs are very high compared to other systems measured by PFM using similar conditions^{8,14}. Independently of the absolute value of the magnetoelectric coefficient, the results clearly establish that partially removing the Si substrate in the suspended microdiscs reduces the substrate clamping effect and, as a consequence, it significantly increases the magnetoelectric effect^{7,25–27}.

5.2.5. Indirect Evaluation of the ME-induced Electric Fields by Catalytic Degradation of Methylene Blue

The overall ME-induced electric field was indirectly evaluated by studying its influence in catalytic degradation of methylene blue. A magnetic field of 200 Oe at 100 Hz was applied and the rates of degradation were compared between the continuous film, the non-suspended microdiscs, the suspended microdiscs and a control without any sample. As shown in **Figure 5.9a**, the continuous film showed the weakest response of the three structures, but slightly larger than the control. The non-suspended microdiscs exhibited a stronger response, while the suspended microdiscs showed the strongest response. Namely, the suspended microdiscs showed a response more than twice as much as the continuous film response [0.326 ± 0.021 A/A(0 min) and 0.703 ± 0.019 A/A(0 min), respectively]. It is also observed that despite the reduced ME surface area, the responses of the nanostructured configurations were still the largest, compared to the continuous film. These results are in accordance with the conclusions of the local PFM experiments in subsections 5.2.3 and 5.2.4, where the strongest responses were observed for the suspended microdiscs.

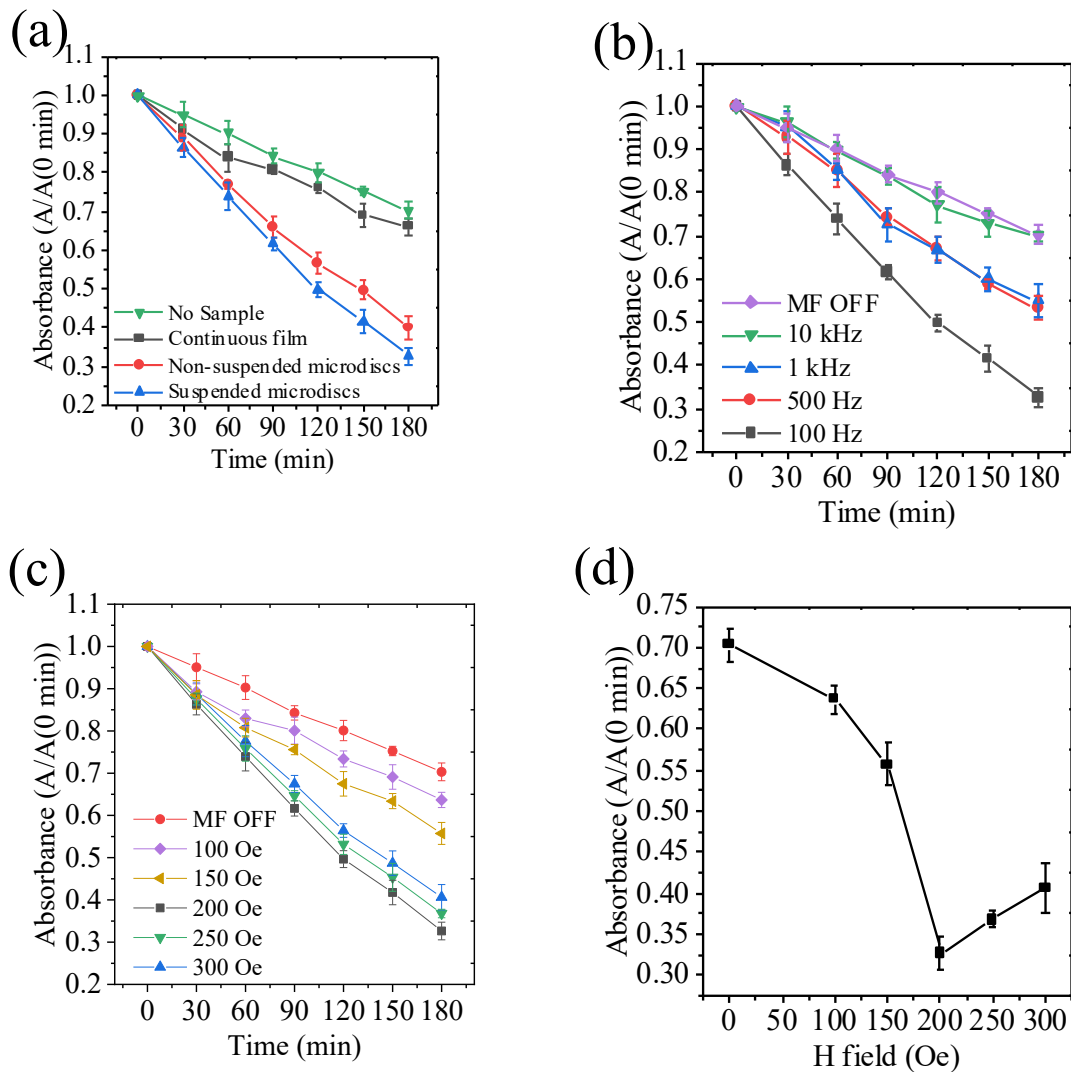


Figure 5.9: Evolution with time of the normalized absorbance at 664 nm in an applied magnetic field (200 Oe, 100 Hz) for (a) the control (no sample), continuous film, non-suspended microdiscs and suspended microdiscs, respectively; (b) for the suspended microdiscs by applying 200 Oe at different frequencies; and (c) for suspended microdiscs by applying different magnetic fields at 100 Hz. (d) Dependence of the normalized absorbance on the applied field. Error bars indicate the standard deviations of the replicated experiments.

Since the strongest response was exhibited by the suspended microdiscs, their response was also assessed under magnetic fields of different intensity and different frequencies. In the case of **Figure 5.9b**, the suspended microdiscs were placed in magnetic fields of 200 Oe, but using different frequencies. It was observed that the weakest response was recorded at 10 kHz, which was similar to the response of no magnetic field (MF OFF). The responses at 500 Hz and 1 kHz were similar and slightly stronger than at 10 kHz. The strongest response was recorded at 100 Hz, which was more than double of the response at 10 kHz [0.326 ± 0.021 A/A(0 min) and 0.699 ± 0.0121 A/A(0 min), respectively]. Although the frequency effects observed in this study may suggest that the ME coupling response of the

heterostructures is frequency-dependent, other effects related to the chemical aspects of the MB degradation may play an important role. Nevertheless, effects related to the mechanical resonance of the structures cannot be ruled out²⁹. Subsequently, when the frequency was fixed at 100 Hz and the magnetic field was varied between 100 Oe and 300 Oe (**Figure 5.9c**), the strongest response was observed at 200 Oe [0.326 ± 0.021 A/A(0 min)] which was 1.8 times larger than the response with 100 Oe [0.636 ± 0.018 A/A(0 min)] and 1.13 times larger than the response with 300 Oe [0.406 ± 0.03 A/A(0 min)]. Also in this case, the findings correspond with the results of the local PFM characterization (**Figure 5.8**), where the strongest response of the suspended microdiscs was observed when a magnetic field of 200 Oe was applied. Moreover, the non-monotonic dependence of the degradation on the applied field is probably related to the field dependence of the magnetostriction²⁸.

These results support previous findings that the substrate clamping effect inhibits the ME effect in the structures, consequently, removing the Si substrate from underneath the microdiscs improves the ME response.

5.2.6. Biocompatibility Assay and Calcium Peak Detection

The biocompatibility of the heterostructures was confirmed in all three configurations by assessing their cytotoxicity. The impact cytotoxicity on human osteoblast cells (hOBs) was evaluated by quantifying live cells with esterase activity and the number of dead cells. After analysing the three Au/FeGa/BaTiO₃ configurations after three days of cell culture, the percentage of live cells was found to be 98.1% for the continuous film (CF), 97.9% for the non-suspended microdiscs (NSMD) and 98.1% for the suspended microdiscs (SSMD), strongly corroborating the biocompatibility of the heterostructures (**Figure 5.10a**).

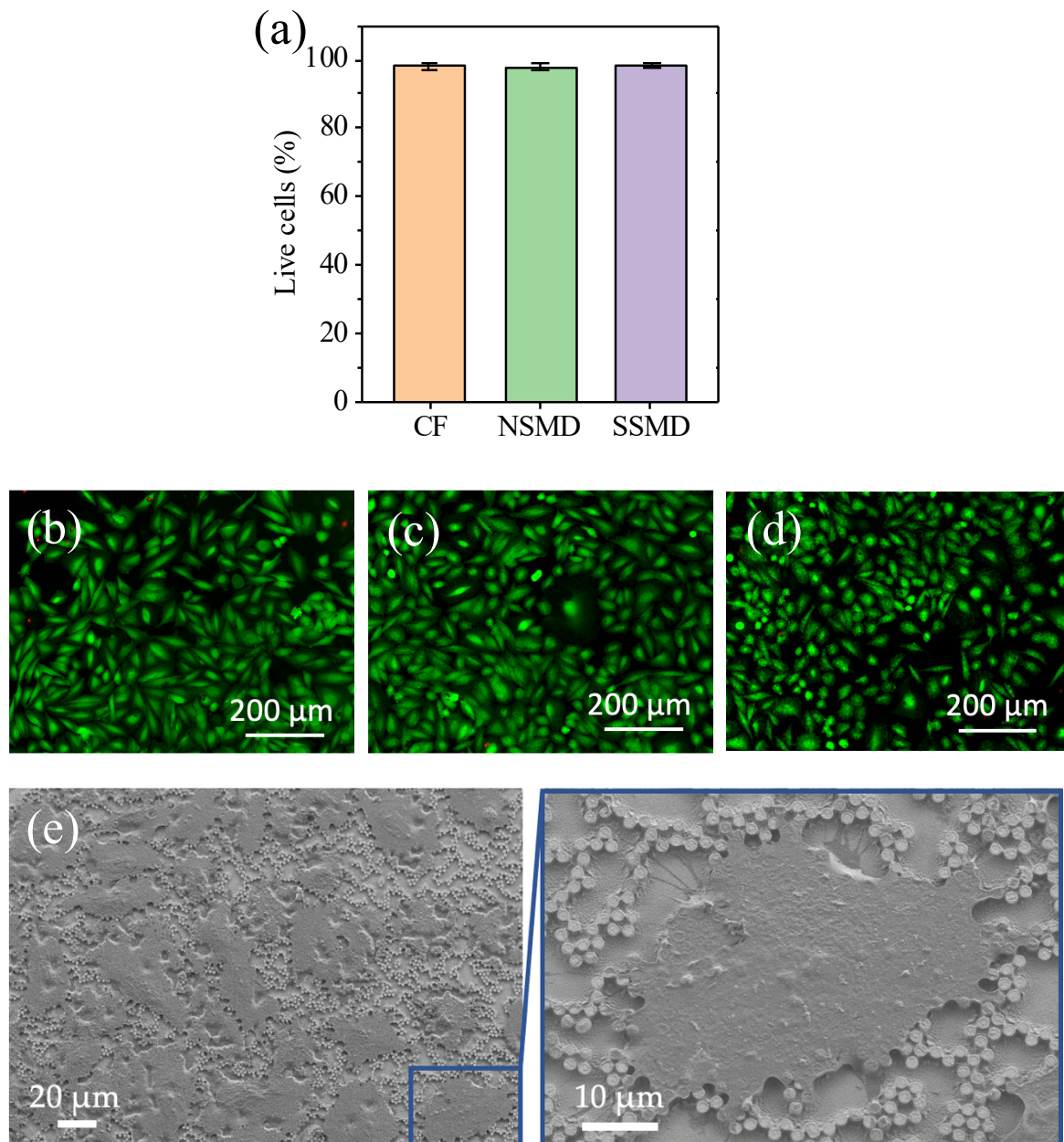


Figure 5.10: (a) Cell viability of hOBs on the Au/FeGa/BaTiO₃ configurations; CF = continuous film; NSMD = non-suspended microdiscs; and SSMD = suspended microdiscs; Error bars indicate the standard deviation of the replicated experiments (b) Cell viability image of hOBs on the continuous film (c) Cell viability image of hOBs on the non-suspended microdiscs (d) Cell viability image of hOBs on the suspended microdiscs (e) SEM Image of cell cultures on the Au/FeGa/BaTiO₃ Suspended microdiscs. Shown in the right panel of is an enlarged view of the area highlighted by the rectangle in the left panel.

The intracellular calcium peaks caused by the activation of voltage gated Ca channels were also detected in osteosarcoma Saos-2 cells. The calcium peaks were generated by wireless magnetoelectric stimulation of the cells cultured on the suspended microdiscs, and demonstrate the magnetic field-induced cell

stimulation. Particularly, the changes of the fluorescence intensity of the cells (**Figure 5.11a** and **b**) indirectly indicate changes in intracellular calcium levels, thereby confirming the wireless cell activation and signalling. More importantly, when the cells are cultured on a Si substrate (i.e., without the ME heterostructure), no changes in the fluorescence were detected when the magnetic field was applied, indicating that the cells were not activated (**Figure 5.11c** and **d**).

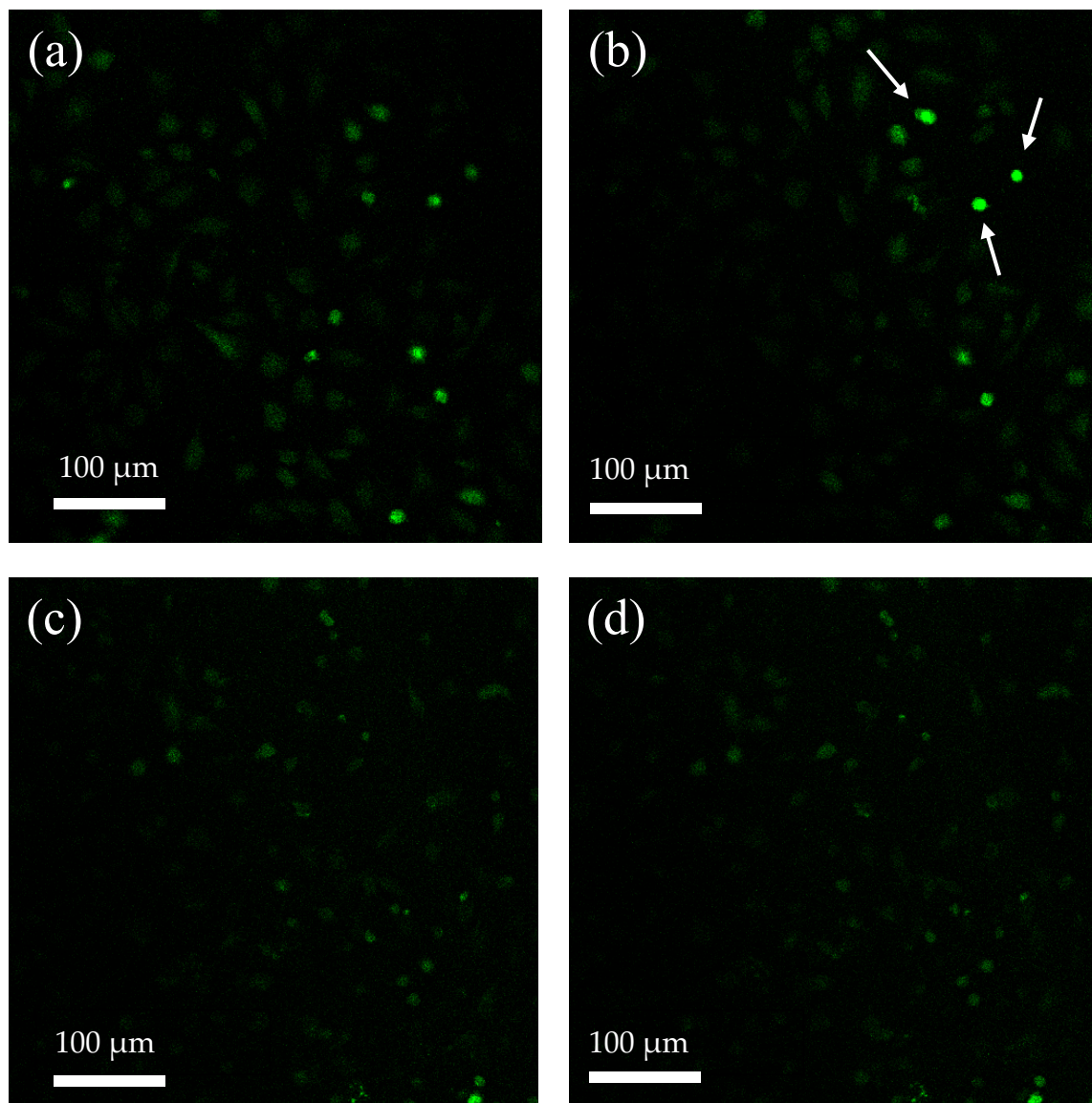


Figure 5.11: (a) Human osteosarcoma Saos-2 cells on Au/FeGa/BaTiO₃ suspended microdiscs with 0 Oe magnetic field applied, and (b) with 200 Oe magnetic field applied (the arrows indicate some of the activated cells); (c) Human osteosarcoma Saos-2 cells on a Si substrate with 0 Oe magnetic field applied, and (d) with 200 Oe magnetic field applied.

5.3. CONCLUSIONS

In conclusion, we have successfully fabricated magnetoelectric Au/FeGa/BaTiO₃ suspended microdisc heterostructures. The results demonstrate that the reduced substrate clamping in the suspended microdiscs leads to a significantly improved magnetoelectric performance compared to non-suspended microdiscs or continuous films of the same composition.

The properties of the Au/FeGa/BaTiO₃ composites were studied using piezo force microscopy (PFM) and found that the edges of non-suspended and suspended microdiscs showed stronger mechanical response than their centres and continuous film. The piezoelectric coefficients of continuous film, non-suspended microdiscs, and suspended microdiscs were evaluated to be $3.7 \pm 0.3 \text{ pm}\cdot\text{V}^{-1}$, $7.7 \pm 0.4 \text{ pm}\cdot\text{V}^{-1}$, and $13.2 \pm 0.4 \text{ pm}\cdot\text{V}^{-1}$, respectively. The heterostructure exhibited ferroelectric character and had in-plane magnetization with similar coercivity ($H_c = 180 \text{ Oe}$), but the field required to saturate the sample increased for the three configurations. The magnetoelectric coupling coefficient was the highest for suspended microdiscs at $730 \pm 70 \text{ V}\cdot\text{cm}^{-1}\cdot\text{Oe}^{-1}$ to $1040 \pm 70 \text{ V}\cdot\text{cm}^{-1}\cdot\text{Oe}^{-1}$ in the centre and edge of microdiscs, respectively, an improvement compared to the continuous film ($260 \pm 70 \text{ V}\cdot\text{cm}^{-1}\cdot\text{Oe}^{-1}$). The improved performance of the suspended microdiscs was also evident in the catalytic effect of the ME-induced electric field in pollutant degradation (methylene blue) under a magnetic field of 200 Oe at 100 Hz, which also proven to be the optimal magnetic field parameters, and in accordance with the magnetic coercivity of the heterostructure. Additionally, the heterostructures exhibited excellent biocompatibility, showing an average of 98% of living cells in the three configurations after 3 days of growing. Finally, intracellular calcium transients caused by ME-induced electrical fields were observed in Saos-2 cells, confirming wireless cell stimulation.

Overall, our work contributes to the development of improved magnetoelectric materials and offers insights into the importance of controlling the substrate clamping effect in these systems. As demonstrated by our results, suspended heterostructures provide a promising route towards enhancing the performance of magnetoelectric materials and expanding their potential applications in various fields.

5.4. REFERENCES

1. Eerenstein, W., Mathur, N. D. & Scott, J. F. Multiferroic and magnetoelectric materials. *Nature* **442**, 759–765 (2006).
2. Pradhan, D. K., Kumari, S. & Rack, P. D. Magnetoelectric Composites: Applications, Coupling Mechanisms, and Future Directions. *Nanomaterials* **10**, 2072 (2020).
3. Bichurin, M., Petrov, V., Priya, S. & Bhalla, A. Multiferroic Magnetoelectric Composites and Their Applications. *Adv Condens Matter Phys* **2012**, 129794 (2012).
4. Kopyl, S., Surmenev, R., Surmeneva, M., Fetisov, Y. & Kholkin, A. Magnetoelectric effect: principles and applications in biology and medicine—a review. *Mater Today Bio* **12**, 100149 (2021).
5. Kang, M.-G. *et al.* Enhanced piezoelectric properties of vertically aligned single-crystalline NKN nano-rod arrays. *Sci Rep* **5**, 10151 (2015).
6. Matavž, A., Bradeško, A., Rojac, T., Malič, B. & Bobnar, V. Self-assembled porous ferroelectric thin films with a greatly enhanced piezoelectric response. *Appl Mater Today* **16**, 83–89 (2019).
7. Kim, D. *et al.* Magnetoelectric coupling in micropatterned BaTiO₃/CoFe₂O₄ epitaxial thin film structures: Augmentation and site-dependency. *Appl Phys Lett* **119**, 012901 (2021).
8. Nicolenco, A. *et al.* Strain gradient mediated magnetoelectricity in Fe-Ga/P(VDF-TrFE) multiferroic bilayers integrated on silicon. *Appl Mater Today* **19**, 100579 (2020).
9. Kim, S., Seol, D., Lu, X., Alexe, M. & Kim, Y. Electrostatic-free piezoresponse force microscopy. *Sci Rep* **7**, 41657 (2017).
10. Martín, J. I., Nogués, J., Liu, K., Vicent, J. L. & Schuller, I. K. Ordered magnetic nanostructures: fabrication and properties. *J Magn Mater* **256**, 449–501 (2003).
11. Ahmad, H., Atulasimha, J. & Bandyopadhyay, S. Electric field control of magnetic states in isolated and dipole-coupled FeGa nanomagnets delineated on a PMN-PT substrate. *Nanotechnology* **26**, 401001 (2015).
12. Qiao, H., Kwon, O. & Kim, Y. Electrostatic effect on off-field ferroelectric hysteresis loop in piezoresponse force microscopy. *Appl Phys Lett* **116**, 172901 (2020).
13. Miao, H., Zhou, X., Dong, S., Luo, H. & Li, F. Magnetic-field-induced ferroelectric polarization reversal in magnetoelectric composites revealed by piezoresponse force microscopy. *Nanoscale* **6**, 8515 (2014).
14. Chen, X.-Z. *et al.* Hybrid Magnetoelectric Nanowires for Nanorobotic Applications: Fabrication, Magnetoelectric Coupling, and Magnetically Assisted In Vitro Targeted Drug Delivery. *Adv Mater* **29**, 1605458 (2017).
15. Chen, X.-Z. *et al.* Ordered arrays of a defect-modified ferroelectric polymer for non-volatile memory with minimized energy consumption. *Nanoscale* **6**, 13945–13951 (2014).

16. Caruntu, G., Yourdkhani, A., Vopsaroiu, M. & Srinivasan, G. Probing the local strain-mediated magnetoelectric coupling in multiferroic nanocomposites by magnetic field-assisted piezoresponse force microscopy. *Nanoscale* **4**, 3218–3227 (2012).
17. Trivedi, H. *et al.* Local manifestations of a static magnetoelectric effect in nanostructured BaTiO₃–BaFe₁₂O₉ composite multiferroics. *Nanoscale* **7**, 4489–4496 (2015).
18. Rodriguez, B. J. *et al.* Vortex Polarization States in Nanoscale Ferroelectric Arrays. *Nano Lett* **9**, 1127–1131 (2009).
19. Kalinin, S. v. & Bonnell, D. A. Imaging mechanism of piezoresponse force microscopy of ferroelectric surfaces. *Phys Rev B* **65**, 125408 (2002).
20. Ramana, E. V., Figueiras, F., Graça, M. P. F. & Valente, M. A. Observation of magnetoelectric coupling and local piezoresponse in modified (Na_{0.5}Bi_{0.5})TiO₃–BaTiO₃–CoFe₂O₄ lead-free composites. *Dalton Trans.* **43**, 9934–9943 (2014).
21. Plyushch, A. *et al.* Magnetoelectric coupling in nonsintered bulk BaTiO₃–xCoFe₂O₄ multiferroic composites. *J Alloys Compd* **917**, 165519 (2022).
22. Hou, Y., Lü, Z., Zhang, Y., Xu, G. & Xu, H. The improved imprint effect in poly(vinylidene fluoride-trifluoroethylene) copolymer ultrathin films. *Appl Phys Lett* **101**, 183504 (2012).
23. Hou, Y. *et al.* Fast switching protocol for ferroelectric random access memory based on poly(vinylidene fluoride-trifluoroethylene) copolymer ultrathin films. *Appl Phys Lett* **102**, 063507 (2013).
24. Naber, R. C. G., Blom, P. W. M., Marsman, A. W. & de Leeuw, D. M. Low voltage switching of a spin cast ferroelectric polymer. *Appl Phys Lett* **85**, 2032–2034 (2004).
25. Petrov, V. M., Bichurin, M. I., Laletin, V. M., Paddubnaya, N. N. & Srinivasan, G. Modeling of Magnetoelectric Effects in Ferromagnetic / Piezoelectric Bulk Composites. in *Magnetoelectric Interaction Phenomena in Crystals* (Springer Netherlands, 2004) p. 65–70.
26. Amrillah, T. *et al.* Flexible Multiferroic Bulk Heterojunction with Giant Magnetoelectric Coupling via van der Waals Epitaxy. *ACS Nano* **11**, 6122–6130 (2017).
27. Li, T., Wang, H., Ma, D., Li, K. & Hu, Z. Influence of clamping effect in BaTiO₃ film on the magnetoelectric behavior of layered multiferroic heterostructures. *Mater Res Bull* **115**, 116–120 (2019).
28. Laletin, V. M., Paddubnaya, N. N. & Filippov, D. A. Field dependence of magnetoelectric effect in the electromechanical resonance region on the Permendur -Quartz - Permendur structures. *IOP Conf Ser Mater Sci Eng* **939**, 012040 (2020).

6. Conclusions and Future Perspectives

6.1. CONCLUSIONS

In this thesis, two different approaches were implemented to address the issue of the substrate clamping effect in magnetolectric composite heterostructures for potential applications in biomedicine. More specifically, the use of a flexible elastomer substrate and nanopatterning have enabled us to obtain heterostructures with an enhanced magnetolectric response. The specific conclusions of the thesis are listed below:

1. The growth of a highly flexible magnetolectric composite film, composed of hydrothermally synthesized piezoelectric ZnO nanosheets covered with magnetostrictive FeGa layer and embedded in a polydimethylsiloxane (PDMS) elastomer layer, has been successfully carried out. This heterostructure exhibited excellent flexibility, conformability and good magnetolectric properties.
2. Indirect evaluation of the magnetolectric response of the film was performed by observing the electric field-induced methylene blue degradation under magnetic field actuation. It showed that the strongest degradation occurred in the presence of a 200 Oe magnetic field at a frequency of 100 Hz, indicating the generation of the largest electric fields. This finding provides important insights into the optimal conditions for inducing electric fields, which could be useful in developing applications for the composite film.
3. The highly flexible magnetolectric composite film was shown to be biocompatible. Moreover, cell proliferation studies demonstrated that after 7 days of 1 h daily magnetolectric stimulation, the stimulated cells exhibited a 42% enhancement in proliferation compared to non-stimulated cells. These findings suggest that the highly flexible magnetolectric composite film could have potential applications in biomedicine, specifically in promoting cell growth and tissue regeneration.
4. The fabrication of magnetolectric Au/FeGa/BaTiO₃ suspended microdiscs was achieved. The magnetolectric properties of the suspended microdiscs demonstrate that the magnetolectric performance of these suspended microdiscs is considerably better than that of non-suspended microdiscs or continuous films of the same composition, due to the removal of the Si substrate from underneath the microdiscs.
5. The piezoelectric coefficients measured for the different morphologies showed that the suspended microdiscs had the highest coefficient (3.5-fold increase over the continuous films).

6. The magnetoelectric response, evaluated by piezo force microscopy, showed that the suspended microdiscs exhibited a much stronger electromechanical response (4-fold) compared to the continuous film and non-suspended microdiscs. This was confirmed by the indirect evaluation of the catalytic effect of magnetoelectric-induced electric fields under magnetic actuation on the degradation of methylene blue. The local and global magnetoelectric response was found to be strongest for a magnetic field of 200 Oe at 100 Hz.
7. The cell biocompatibility experiments conducted on the Au/FeGa/BaTiO₃ heterostructures demonstrated exceptional results, with a 98% viability of cells observed after three days. Additionally, intracellular calcium transients caused by the magnetic-field-induced electric stimulation were detected by observing fluorescence intensity changes, confirming the wireless electrical stimulation via voltage-gated Ca channels. This highlights the potential of these heterostructures for biomedical applications, showcasing their compatibility and promising prospects in the field of biomedicine especially the suspended microdiscs which exhibited an enhanced magnetoelectric response.

6.2. FUTURE PERSPECTIVES

Even though both magnetoelectric composite heterostructures showed high efficiency and promising potential, there are still many obstacles that need to be addressed and dealt with in order for them to be able to be used into functional applications in biomedicine. Specific upcoming perspectives of the work of this thesis are detailed below:

1. The FeGa/ZnO thin film heterostructure has shown promising results for bone cell electrostimulation *in vitro*. Thus, further *in vitro* studies such as differentiation assays could provide further confirmation on the applicability of the film. Additionally, it would be interesting for the possibility to apply this approach to other electrostimulable cells such as skin cells or neurons.
2. Despite the good results *in vitro*, its potential for *in vivo* applications remains to be explored. Future research could investigate the biocompatibility and long-term stability of the heterostructure, and optimize its design and fabrication for *in vivo* applications.
3. In addition to cell electrostimulation, given their excellent flexible/conformable character, the FeGa/ZnO thin film heterostructure may have other potential applications in sensors, actuators, and energy harvesting. Future research could explore these areas and develop new devices based on the heterostructure, as well as investigate the scalability and manufacturability of the fabrication process.

4. The remarkable cell biocompatibility demonstrated by the Au/FeGa/BaTiO₃ heterostructures, with 98% cell viability and exhibited calcium signalling by the observation of intracellular calcium transients under magnetic field, sets a solid foundation for further investigations. Extended and repeated in vitro analyses will be carried out in order to better understand the gene and protein expression changes. Thus, understanding cellular behaviour under the proven enhanced magnetoelectric response of the micropatterned can push the potential of the structures in healthcare solutions.
5. The development of magnetoelectric Au/FeGa/BaTiO₃ suspended microdisc heterostructures offers a promising platform for biomedical applications. The enhanced magnetoelectric performance can be utilized for the design of novel wireless cell electrostimulation devices. Future research can focus on the optimization of the fabrication process, larger-scale production for practical applications for injected or implanted devices for remote electrostimulation in vivo.
6. Although, the results of this study demonstrate the great potential of the Au/FeGa/BaTiO₃ suspended microdiscs, future studies can focus on optimizing the design and fabrication of these structures to improve their magnetoelectric properties and expand their application range. For example, varying the size, shape or thickness and composition of the ferromagnetic and ferroelectric layers can potentially improve the magnetoelectric coupling coefficient and reduce the magnetic field required for inducing a strong electric polarization.

